PolyPublie
Polytechnique Montréal

POLYTECHNIQUE MONTRÉAL
UNIVERSITÉ D'INGÉNIERIE

Titre: Title:	Deformable MRI to Transrectal Ultrasound Registration for Prostate Interventions Using Deep Learning
Auteur: Author:	Shirin Shakeri
Date:	2020
Type:	Mémoire ou thèse / Dissertation or Thesis
Référence: Citation:	Shakeri, S. (2020). Deformable MRI to Transrectal Ultrasound Registration for Prostate Interventions Using Deep Learning [Mémoire de maîtrise, Polytechnique Montréal]. PolyPublie. https://publications.polymtl.ca/5369/

Document en libre accès dans PolyPublie
Open Access document in PolyPublie

URL de PolyPublie: PolyPublie URL:	https://publications.polymtl.ca/5369/
Directeurs de recherche: Advisors:	Samuel Kadoury, & Cynthia Ménard
Programme: Program:	Génie informatique

Ce fichier a été téléchargé à partir de PolyPublie, le dépôt institutionnel de Polytechnique Montréal
This file has been downloaded from PolyPublie, the institutional repository of Polytechnique Montréal

https://publications.polymtl.ca

POLYTECHNIQUE MONTRÉAL
affiliée à l'Université de Montréal

Deformable MRI to Transrectal Ultrasound Registration for Prostate Interventions Using Deep Learning

SHIRIN SHAKERI
Département de génie informatique et génie logiciel

Mémoire présenté en vue de l'obtention du diplôme de *Maîtrise ès sciences appliquées*
Génie informatique

Août 2020

© Shirin Shakeri, 2020.

POLYTECHNIQUE MONTRÉAL
affiliée à l'Université de Montréal

Ce mémoire intitulé :

Deformable MRI to Transrectal Ultrasound Registration for Prostate Interventions Using Deep Learning

présenté par **Shirin SHAKERI**
en vue de l'obtention du diplôme de *Maîtrise ès sciences appliquées*
a été dûment accepté par le jury d'examen constitué de :

Lama SEOUD, présidente
Samuel KADOURY, membre et directeur de recherche
Cynthia MENARD, membre et codirectrice de recherche
Frédéric LEBLOND, membre

DEDICATION

To my amazing sister Mahsa, brother in law Hani, and nephew Ayden.
For their love, encouragements, and supports....

ACKNOWLEDGEMENTS

I would like to express my deep and sincere gratitude to my research director, Prof. Samuel Kadoury, for his continuous support, his patience, and valuable advice. His encouragements and motivation has guided me through the way.
I would like to greatly thank my co-director, Dr. Cynthia Menard, who guided me throughout my Master's with her great supports. I would like to convey my gratitude to the committee for accepting to be my Master's jury member. I am dedicating this thesis to my beloved parents, my sisters Mojdeh and Mahsa, my dear brother-in-laws Hani Nemati and Ali Mirzadeh and my niece and nephew Diana and Ayden. For their non-stop support, endless love and encouragements. I would like to thank all my colleagues at the "MEDICAL-Lab", especially Rosalie Plantefève, Roozbeh Shams, William Trunge,and my friends who shared knowledge, wisdom, and joy with me.

RÉSUMÉ

Le cancer de la prostate est l'un des principaux problèmes de santé publique dans le monde. Un diagnostic précoce du cancer de la prostate pourrait jouer un rôle vital dans le traitement des patients. Les procédures de biopsie sont utilisées à des fins de diagnostic. À cet égard, l'échographie transrectale (TRUS) est considérée comme un standard pour l'imagerie de la prostate lors d'une biopsie ou d'une curiethérapie. Cette technique d'imagerie est relativement peu coûteuse, peut scanner l'organe en temps réel et est sans radiation. Ainsi, les scans TRUS sont utilisés pour guider les cliniciens sur l'emplacement d'une tumeur à l'intérieur de la prostate. Le défi majeur réside dans le fait que les images TRUS ont une faible résolution et qualité d'image. Il est difficile de distinguer l'emplacement exact de la tumeur et l'étendue de la maladie. De plus, l'organe de la prostate subit d'importantes variations de forme au cours d'une intervention de la prostate, ce qui rend l'identification de la tumeur encore plus difficile. Une solution consiste au recalage d'un scan préopératoire de haute qualité et à l'utiliser comme référence pour identifier les limites et les cibles de la prostate sur les images TRUS peropératoires. La tomodensitométrie (TDM) et l'IRM (imagerie par résonance magnétique) sont deux modalités courantes qui sont utilisées à des fins diagnostic. Ces modalités d'imagerie peuvent fournir des informations à haute résolution sur l'emplacement de la tumeur et la limite de l'organe de la prostate. Ici, une fusion précise est nécessaire pour le recalage d'images préopératoires haute résolution sur celles à basse résolution peropératoire. La fusion d'images est difficile car l'intensité entre les images pré et peropératoires est très différente. De plus, la prostate est un organe flexible qui subit beaucoup de déformations, à cause de la sonde transrectale ou de positions corporelles différentes. Divers approches de fusion multimodales ont été développé dans la littérature. Parmi eux, la fusion par surfaces permettent de déformer la surface de la prostate dans l'espace de l'image préopératoire à la surface de la prostate dans l'image TRUS. Cette technique évite le problème de trouver directement corrélations basées sur l'intensité entre les images pré et intra-opératoires. Il est possible de modéliser la variation de la surface de la prostate et de régulariser le processus de recalage. En règle générale, différentes techniques peuvent être appliquées pour modéliser la prostate variation, linéaire ou non linéaire. Dans ce travail, deux approches différentes le recalage IRM déformable en TRUS sont proposées pour les interventions de la prostate, utilisant une segmentation automatique de la prostate sur les images TRUS. La première méthode proposée est un recalage basé sur un modèle de déformation statistique (SDM), la seconde est une approche d'apprentissage profond, basée sur un modèle d'encodeur-décodeur (AEM) qui permet de modéliser les variations dans un espace latent.

Les approches proposées modélisent la variation de la prostate et utilisent le modèle entrainé afin d'effectuer un recalage non rigide par points d'encrage itératifs (NICP). L'approche SDM comprend deux phases : l'entrainement et la phase de recalage en ligne. Cette méthode nécessite un ensemble d'entrainement de paires IRM-TRUS, les examens IRM et TRUS pairés pour chaque patient. En phase d'apprentissage, la déformation de surface IRM-TRUS est calculée pour chaque paire IRM-TRUS dans l'ensemble d'entraînement. Cela produit un ensemble de données de la surface de la prostate IRM-TRUS déformations. Ces déformations sont modélisées statistiquement à l'aide d'une déformation statistique algorithme de modèle. Dans la phase le recalage, une nouvelle paire MRI-TRUS est donnée à l'algorithme et l'objectif est de déformer l'IRM à sa surface TRUS correspondante. La surface IRM est fusionnée à la surface TRUS à l'aide d'un algorithme de recalage non rigide itératif de points correspondants. Cependant, la déformation est contrainte de s'adapter au modèle SDM entrainé. Outre l'approche basée sur SDM, une méthode de fusion IRM-TRUS basée sur des auto-encodeurs profond est proposée pour modéliser les variations non-linéaiers de surfaces. Cette approche nécessite un ensemble de surfaces TRUS et IRM. Les maillages de surfaces TRUS sont envoyées en entrée à un encodeur automatique (AE). Le modèle encode les données d'entrée dans un espace latent de dimension inférieure et les reconstruits à l'aide du décodeur. L'AE est entrainé de manière à ce que la sortie soit aussi proche que possible de l'entrée. Avec le recalage, une IRM et son image TRUS correspondante est fournie, et l'objectif est de trouver la transformation IRM-TRUS. L'approche AEM proposée recale également la surface de l'IRM à la surface TRUS basée sur l'algorithme NICP. De plus, il contraint la surface TRUS pour s'adapter avec le modèle AE entrainé. Les approches proposées ont été évaluées et comparées sur un ensemble de plus de 45 paires d'images IRM-TRUS obtenues du departement de radio-oncologie au CHUM. Des expériences ont révélé que les approches de fusion IRM-TRUS proposées peuvent produire des résultats similaires à ceux obtenus manuellement par un radio-oncologue. En outre, une analyse plus approfondie a démontré que les approches proposées surclassent les algorithmes le recalage automatique traditionnels.

ABSTRACT

Prostate cancer is one of the major public health issues in the world. An accurate and early diagnosis of prostate cancer could play a vital role in the treatment of patients. Biopsy procedures are used for diagnosis purposes. In this regard, Transrectal Ultrasound (TRUS) is considered a standard for imaging the prostate during a biopsy or brachytherapy procedure. This imaging technique is comparatively low-cost, can scan the organ in real-time, and is radiation free. Thus, TRUS scans are used to guide the clinicians about the location of a tumor inside the prostate organ.

The major challenge lies in the fact that TRUS images have low resolution and quality. This makes it difficult to distinguish the exact tumor location and the extent of the disease. In addition, the prostate organ undergoes important shape variations during a prostate intervention procedure, which makes the tumor identification even harder.

One solution is to register a high-quality pre-operative scan and use it as a reference to identify the prostate boundaries and targets on intra-operative TRUS images. CT (Computed Tomography) and MRI (Magnetic Resonance Imaging) are two common modalities that are used for diagnosis purposes. These imaging modalities can provide high-resolution information on tumor location and the boundary of the prostate organ. Here, an accurate fusion approach is required to register the high-resolution pre-operative image to the low-resolution intra-operative scan.

Image fusion is challenging since the intensity between pre- and intraoperative images is very different. In addition, the prostate is a flexible organ that undergoes a lot of deformation, because of either the Transrectal Probe or different body positions. Various multimodal fusion approaches have been developed in the literature. Among them, surface-based fusion approaches can deform the prostate surface from the space of the pre-operative image to the prostate surface in the TRUS image. This technique avoids the issue of directly finding intensity-based correlations between pre- and intra-operative images. In surface-based fusion approaches, there is a possibility to model the prostate surface variation and regularize the registration process. Typically, different techniques can be applied to model the prostate variation, either linear or nonlinear.

In this work, two different deformable MRI to TRUS registration approaches are proposed for prostate interventions using an automatic prostate segmentation on TRUS images. The first proposed method is a Statistical Deformation Model (SDM) based registration, while the second one is a deep learning approach based on an AutoEncoder model (AEM). Both

proposed approaches model prostate variation and use the trained model as a regularizer in a non-rigid iterative closet points (NICP) registration.

The SDM approach includes two phases: training and registration phase. This method requires a training set of MRI-TRUS pairs, both MRI and TRUS scans gathered for each patient. In the training phase, the MRI-TRUS surface deformation is computed for each MRI-TRUS pair in the training set. This produces a dataset of MRI-TRUS prostate surface deformations. These deformations are statistically modeled using a statistical deformation model algorithm. In the registration phase, an unseen MRI-TRUS pair is given to the algorithm and the objective is to deform the unseen MRI to its corresponding TRUS surface. The MRI surface is fused to the TRUS surface using a non-rigid iterative closest point algorithm. However, the deformation is constrained to fit in the trained SDM model.

Apart from the SDM based approach, an Auto Encoder based MRI-TRUS fusion method is proposed that models the TRUS surface variations. This approach requires a training set of TRUS surfaces. The TRUS surface meshes are fed as input to an Auto Encoder (AE). The AE encodes the input data into a lower-dimensional space and reconstructs it as a decoder output. The AE is trained in a way that the output is as close as possible to the input. At registration time, an MRI and its corresponding TRUS image are provided, and the goal is to find the MRI-TRUS transformation. The proposed AEM approach also registers the MRI surface to the TRUS surface based on the NICP algorithm. In addition, it constrains the TRUS surface to fit in the trained AE model.

The proposed approaches have been evaluated and compared on a prostate dataset of 45 patients with MRI-TRUS images from the radio-oncology department at CHUM. Experiments revealed that the proposed MRI-TRUS fusion approaches can produce results similar to gold-standard manual registration. In addition, further analysis showed that the proposed approaches outperform the baseline automatic registration algorithms.

TABLES OF CONTENTS

LIST OF TABLES

LIST OF FIGURES

LIST OF SYMBOLS AND ABBREVIATIONS

2D	2-Dimensional
3D	3-Dimensional
MRI	Magnetic Resonance Image
TRUS	Transrectal Ultrasound
CT	Computed Tomography
PCA	Principal component analysis
SDM	Statistical deformation model
AE	Auto encoder
ICP	Iterative Closest Point
NICP	Non-Rigid Iterative Closest Point
FMM	Finite Element Model
PCa	Prostate Cancer
TR	Repetition time
TE	Echo time
RF	Radio Frequency
TZ	Transitional Zone
PZ	Peripheral Zone
LDR	Low Dose Rate
HDR	High Dose Rate
KNN	K-Nearest Neighbor
EBRT	External Beam Radiation Therapy
SSM	Statistical Shape Model
SDM	Statistical Deformation Model
RELU	Rectified Linear Unit
FDD	Free Form Deformation
CC	Correlation Coefficient
GAN	Generative adversarial network
TPS	Thin Plate Splines
RMSE	Root Mean Square Error
AEM	Auto Encoder Models
MSD	Mean Squared Distance
MSE	Mean Squared Error
TRE	Target Registration Error

RPM	Robust Point Matching
CNN	Convolutional Neural Network
DSC	Dice Score
S_{MRI}	MRI surface mesh
S_{TRUS}	TRUS surface mesh

CHAPITRE 1 INTRODUCTION

1.1 Motivation and clinical rationale

The prostate is a flexible organ beneath the bladder that is the size of a walnut. It is a part of the male reproductive system which secretes mucus and the prostatic fluid. Prostate cancer (PCa) is leading cancer among the Canadian male society with an estimation of 22,900 new cases in 2019. Generally, one in every five new cancer cases is PCa (20%). An accurate and early diagnosis of prostate cancer can play a vital role in treating the patient.

A biopsy procedure is part of the diagnosis approach. It gives the physician enough proof about the existence of a tumor inside the prostate. In many cases, the brachytherapy procedure is a treatment option, which is based on radiation therapy used to treat local cancers. It places radioactive sources inside the patient to kill cancerous cells and shrink tumors. There are two types of brachytherapy procedures : high dose and low dose. Either of them could be employed depending on the type of tumor. During the procedure, there is a crucial need for an imaging technology to guide the clinicians in localizing the needles with respect to the tumor.

Transrectal Ultrasound (TRUS) imaging is one of the most popular modalities for this procedure since it can scan the organ in real-time and has comparatively low-cost and is radiation free. In this technique, a probe is inserted inside the patient's rectum to take the image of the prostate organ through the rectum wall. The major challenge in urological interventions that use TRUS as image modality is the low resolution and quality of the images. It makes it difficult to assess the location and the extent of disease. The ambiguous boundary of the prostate leads to poor organ localization by the clinician.

One solution to this problem is to provide a high-quality pre-operative scan and use it as a reference to help to localize the organ on real-time TRUS (Figure 2.1). Usually, either a CT (Computed Tomography) or MRI (Magnetic Resonance Imaging) modality is chosen to provide high-resolution information about the patient's anatomy. However, the challenge is to match the pre-operative scan to the intra-operative image. Besides the fact voxel intensities differ between pre- and intra-operative scans, the prostate is a flexible organ that undergoes important elastic deformations. Both the transrectal probe (external pressure) and different body positions can cause motion on the prostate gland. Moreover, the exact shape of this gland slightly varies from one person to another, especially in the presence of a tumor. Hence, a robust non-rigid registration is required to describe the deformation of the organ.

Several multimodal registration approaches have been developed in the literature to perform this pre-operative/intra-operative fusion. Intensity-based multimodal registration methods maximize the intensity similarity between two images. However, comparing two separate modalities requires to extract a group of homologous anatomical features that appear in both images. The challenge is that since the imaging physics are substantially different between the two modalities, there may be parts of the anatomy that can be visible in one image but not in the other. For instance, in TRUS, the boundary of the prostate is not easily distinguished at its base, which makes it difficult to find where the prostate ends and the seminal vesicles begin.

On the other hand, surface-based fusion approaches can model the prostate variations in preoperative image and deform the prostate surface to the space of the TRUS image. Hence, if the segmentation of both pre-operative and intra-operative scans are available during the brachytherapy procedure, we can exploit a surface-based registration technique. This avoids the issue of finding intensity-based correlations between pre and intra-operative scans. Typically, different approaches can be used to model the prostate variation, either linear or nonlinear.

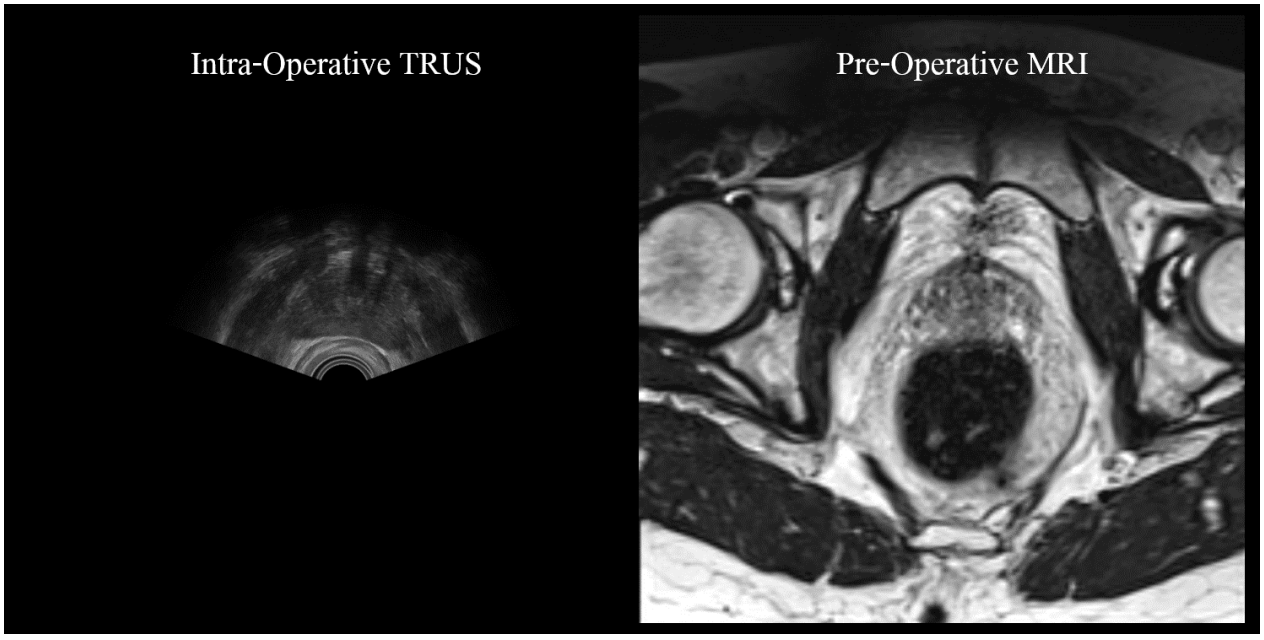

FIGURE 1.1 An intraoperative Transrectal Ultrasound (TRUS) image (Left) of the prostate and it's pre-operative MRI (Right) at the mid gland level. Unlike TRUS image the anatomical areas for example zonal anatomy can be well distinguished on MRI.

This work presents two different surface-based registration approaches to register a preoperative MRI to an intra-operative TRUS surface, each based on the automatic segmentation of the prostate on TRUS volumes. The first approach is the Statistical Deformation Model-based registration (SDM-registration), while the second proposed method is an Auto-Encoder Model-based registration (AEM-registration). The idea of both of these proposed registration approaches is to constrain the MRI/TRUS surface fusion to the plausible deformations.

The SDM-registration approach includes two phases : training phase and registration phase. This method requires a training set of MRI/TRUS pairs as pre-operative/intra-operative scans. In the training phase, first, the prostate surface meshes are extracted from the MRI and TRUS images. Then, point to point correspondence is established between all surfaces. Next, the MRI to TRUS surface deformation is computed for each MRI/TRUS pair in the training set. The result will be a list of MRI/TRUS prostate surface deformations. In the next step, a statistical deformation model (SDM) is trained to model the variation in the prostate deformation from MRI to TRUS.

In the registration phase, an unseen MRI/TRUS pair is given and the goal is to find the MRI to TRUS surface fusion. Here, first, the prostate surfaces are extracted from both MRI and TRUS images. Then, the trained SDM is incorporated into a Non-rigid registration algorithm to perform the MRI-TRUS surface fusion on the unseen patient data.

The AEM-registration approach includes two steps : a training step and a registration step. This approach requires a train set of TRUS images. In the training step, first prostate surface meshes are extracted from TRUS images in our training set. Then, an Auto Encoder (AE) is trained on TRUS surfaces to encode TRUS meshes into a lower-dimensional space. In fact, the AE can encode an input TRUS surface into a latent representation then reconstruct the data in a way that is as similar as the input. This characteristic of AE can be used to constrain the shape of an unseen TRUS surface.

In the registration phase, an unseen MRI/TRUS image pair is given and the objective is to find the surface-based fusion between MRI to TRUS. First, MRI and TRUS surface meshes are extracted for the unseen patient data. Then, non-rigid registration between the test MRI and the TRUS meshes is regularized using the trained AE. The registration is regularized in a way that the deformed TRUS surface fits into the latent representation of the AE.

1.2 Contribution

In this work, a new TRUS prostate segmentation, as well as two separate surface registration approaches are proposed to reduce the manual work required by radio-oncologists and simplify

the brachytherapy workflow : (1) a Statistical Deformation Model-based registration (SDM-registration) and (2) an Auto-Encoder Model-based registration (AEM-registration). Both methods constrain the fusion to an acceptable deformations.

1.2.1 Fully convolutional Residual Network for TRUS segmentation

A dual neural network, consisting of a fully convolutional network (FCN) followed by a ResNet, is developed to automatically segment the prostate in the TRUS images from the base to the apex. The FCN serves as a normalizing pre-processor of images across the dataset. These normalized images are then iteratively refined by means of a FC-ResNet in order to generate a segmentation prediction (9). This segmentation allows creating a mesh surface of the gland used as the target for the registration approaches, described below.

1.2.2 Statistical deformation based registration model

The SDM-registration first models the prostate deformations by training a statistical deformation model on a train set. Then the trained SDM is used to regularize the non-rigid optimal Iterative Closest Point (NICP) registration approach. This proposed approach has been published in SPIE Medical Imaging Conference (8).

SDM algorithm assumes that deformations are distributed in a Gaussian manner. It linearly combines the variance of the shape population of a given anatomical entry. As a result, using SDM algorithm, the unseen motions can be estimated by the linear combination of the training set.

The method is validated on a dataset of 45 brachytherapy patients. Using a leave one out cross-validation framework.

1.2.3 Auto-Encoder based registration model

While a linear assumption may not always cover all the possible scenarios for the data, in the second proposed method a nonlinear approach based on a neural network is designed. Here, an Auto-Encoder (AE) is trained to compress and encode data in a lower-dimensional space based on deep features. The AE learns how to reconstruct the data back from the reduced encoded representation to a representation that is as close to the original input as possible. This characteristic of AE can be used to generate a wider range of prostate variations. In this proposed approach, the registration is constrained with AEM based model.
This approach is also compared to standard manual approaches to register both MRI and TRUS.

1.3 Thesis Structure

This thesis includes seven chapters. Following this introduction, Chapter 2 provides detailed background information that is necessary for reading this thesis along with a critical review of the literature. Chapter 3 includes the problem statement, hypothesis, research objectives, and general methodology. Chapter 4 presents the proposed TRUS segmentation, SDM-based, and AEM based registration methodologies. The experimental results of the segmentation and proposed registration approaches are reported in Chapter 5. In Chapter 6, the general discussion of the thesis is presented. Finally, Chapter 7 summarizes the findings, limitations, and main recommendations for future work.

CHAPITRE 2 BACKGROUND and CRITICAL LITERATURE REVIEW

2.1 Human Prostate

The prostate is a part of a male's reproductive system that entirely surrounds the urethra. This walnut-sized gland is located beneath the bladder and on the anterior side of the rectum. The urethra runs through the center of the prostate, from the bladder to the penis, letting urine flow out of the body. The prostate and the seminal vesicles produce a fluid. This seminal fluid lubricates the urinary tract system, combines with the sperm that comes from the testicle, and nourishes the sperm. (10) , (11), (12). The alkaline quality of the seminal fluid assists neutralizing the potential hydrogen (PH) of the vaginal duct which extends the lifespan of the sperm. (13).

2.1.1 Prostate structure and function

John McNeal histologically categorizes the tissue of the prostate into four major sections : one non-glandular tissue and three glandular regions (Figure 2.1). The fibromuscular stroma is the non-glandular area that surrounds the gland. Transitional, peripheral, and central zones are the terms of the glandular regions "which contain a complex, yet histologically distinct ductal system".(12). Throughout ejaculation this organ contracts for secretion. Figure 2.1-A.

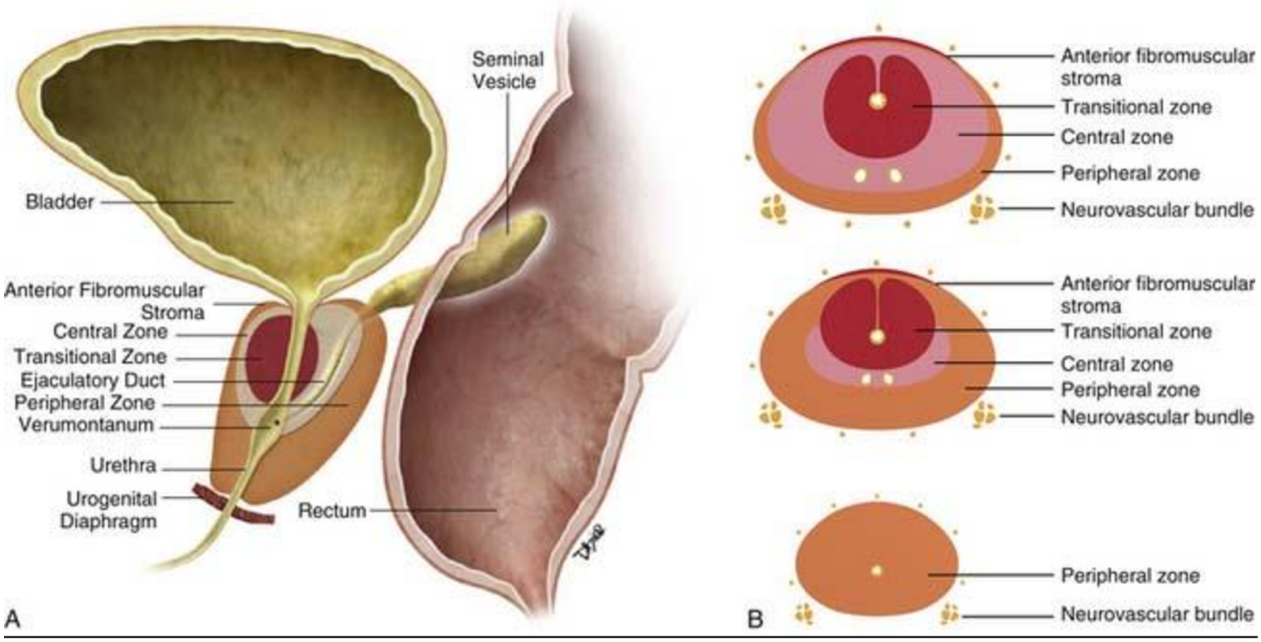

FIGURE 2.1 A. The anatomy of the prostate gland. B. Transverse view of the gland. Source :[https ://clinicalgate.com/].

The prostate is oriented along the prostatic urethra and is divided into three location-wise regions along the urinary tube. The base is the superior sector that is adjacent to the bladder. The apex is the inferior area near the urogenital membrane which mainly encompasses the peripheral zone. The mid-gland section is the area middling these two.Figure 2.1-B.

2.1.2 Epidemiology of prostate cancer

Prostate cancer (PCa) is an abnormal growth of cells inside the organ. A malignant prostate tumor can spread to adjacent tissues and other parts of the body such as the bones. The growth of these cells is often slow and it can either be removed or controlled when a diagnosis is made.

PCa is the fourth most commonly diagnosed non-dermal cancer in Canada. The latest report published by "Canadian Cancer Society Statistics" suggests that one in nine men is expected to be diagnosed with PCa in their lifetime. In men, one in every 5 new cancer cases is PCa (20%). It is leading cancer for the Canadian male population with an estimation of 22,900 new cases in 2019. PCa is the main cause of 9.5% of the cancer deaths in the same year (4,300 patients). Men appear to be at increased risk of developing PCa as they age. The likelihood of a PCa diagnosis on a man starts at eight percent at the age of 20 and reaches 80% by the time he is in his 70s. Early-stage diagnoses and treatment of the PCa declines the patient's

mortality rate. From 1993 to 2016 the death rate of the PCa dropped by 51% (14).

2.1.3 Screening for PCa

Screening is the process of searching for the cancerous-tumor prior to any symptoms. The digital rectal exam (DRE) and examining the Prostate-specific antigen (PSA) level are two of the most common screening tests to identify and treat men with clinically significant prostate cancer. Any reported abnormality on the results of these tests leads to further actions like a biopsy or active surveillance.

Prostate specific antigen test

Prostate-specific antigen (PSA) is a protein produced by the prostate cells. Normally, a certain amount of this antigen exists in the plasma of a man with a healthy prostate. PSA screening tests are one of the common and necessary methods for the early detection of PCa. Elevated levels of PSA in the plasma can be one of the symptoms of a tumor in the prostate. Even though screening with the PSA plays a sensitive role in PCa detection, it lacks specificity. The high level of PSA may also accrue in men with non-cancerous conditions. For instance, some healthy prostates biologically overproduce PSA, some tumors are clinically insignificant and some are benign prostatic hyperplasia1 (BPH).

Urologists should use this factor cautiously in determining whether a person has PCa.

Digital Rectal Examination

Digital Rectal Examination (DRE) is the process of examining the prostate's condition for any abnormality through the rectal wall. Any suspicious bump, hard area, and enlargement could be considered as a symptom. The peripheral zone (PZ) is the largest area of the prostatic tissue. During DRE the dorsal area of the PZ is accessible within the rectum. Since around 70-80% of the PCa tumors are placed in the PZ area, the DRE is capable of diagnosing about 18% of the PCa patients. Due to the fact that this examination lacks the sensitivity parameter and is subject to human error, it should be used in conjunction with further diagnostic tools.

2.2 Imaging modalities to analyze the prostate

2.2.1 Magnetic Resonance Imaging (MRI)

Magnetic Resonance Imaging (MRI) is an imaging modality that utilizes a powerful magnetic field to influence the intracellular environment of the organs, like water and molecules. In exposure to a strong magnetic field, the coherent spinning of the hydrogen protons is affected with particular radio frequency (RF) pulses. It induces the molecules to face a new direction. When the magnetic field is switched off, the protons spin down, realign and return to their equilibrium state. Equivalently, the frequency changes. This phenomenon leads to the emission of the radio waves that are detected as MR signals. Multiple MR signals of various amplitudes are spatially mapped to form the MR image. (15)

Repetition time (TR) is the interval between the corresponding successive points on a recursive pulse to echoes. Echo time (TE) represents the time difference from the center of the RF-pulse to when the MR signal is detected (middle of the echo). As the period of consecutive RF pulsed TR and TE differ, two types of MRI are formed. T1-weighted images are taken when the TR and TE times are short (Figure 2.2-A), while in T2-weighted images, the TR and TE times are long (Figure 2.2-B). Figure 2.2 indicates the recognizable internal anatomy of the prostate gland in either T1-w and T2-w MRIs. In general, MRI is an expensive imaging technique and if captured in real-time it produces low-quality intra-operative images (due to time constraints). Therefore, MR imaging is usually used as a pre-operative imaging modality for planning prostate cancer treatments.

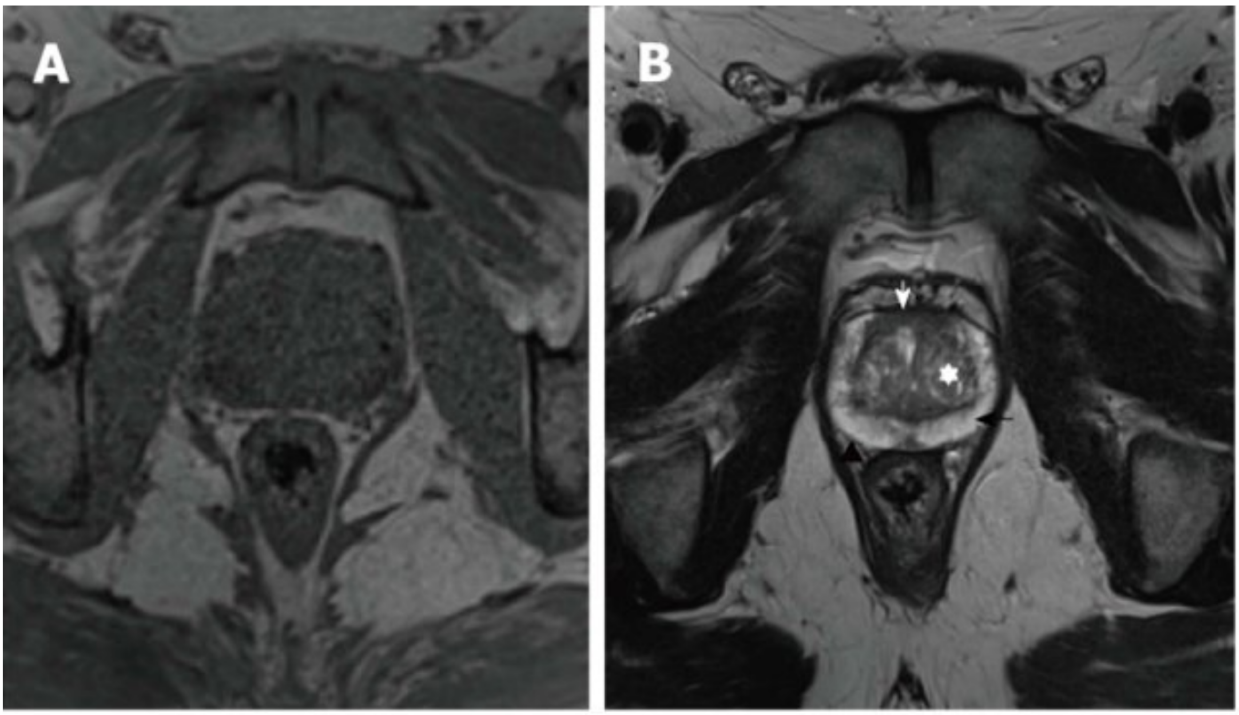

FIGURE 2.2 Prostate anatomy on T1- and T2-weighted Magnetic resonance images. A : Axial T1-weighted MRI of the human prostate. The organ appears as an isointense homogeneous gland. Differentiating the anatomical details in the prostate is challenging. B : T2-weighted axial MRI prostate anatomy. White arrows indicate the anterior fibromuscular stroma. Black arrows point to the peripheral zone (PZ) recognizable as a hyperintense U-shaped tissue. The white asterisk is the transitional zone (TZ) which appears hyperintense and has a multinodular pattern. (1)

2.2.2 Computerized Tomography (CT)

A Computerized Tomography (CT) scan is a diagnostic procedure in which a specialized X-ray provides a cross-sectional image of the body. While a conventional X-ray utilizes a fixed tube that radiates in only one direction, a CT scanner employs a motorized X-ray source that shoots narrow beams of X-rays as it rotates the body in an axial direction. Thus, a CT image reveals more details regarding the bones and soft tissue that a conventional X-ray system does. The scanner consists of an emitter and a receiver that is located opposed to each other.

As the X-rays pass through the patient's body, a detector receives the beam and transmits it to a computer for further analysis and produces 2D or 3D images. Due to the poor contrast, the interior anatomy of the prostate is the separation from the surrounding muscle.

X-ray and computed tomography (CT) images are not used for newly diagnosed prostate cancer if the cancer is likely to be confined to the prostate based on other findings have no diagnostic value in PCa, as separation from surrounding muscle is poor and the anatomy interior to the prostate is not well defined. The primary role of CT is in the detection of metastases and to plan radiation-based therapies in patients with confirmed PCa.

2.2.3 Transrectal ultrasound (TRUS)

Ultrasound is one of the standard imaging techniques during a biopsy or brachytherapy procedure to diagnose or treat prostate cancer. A transrectal ultrasound (TRUS) system for transperineal procedures has three important parts : a TRUS probe, a stepper, and a grid template (16).

The TRUS probe dispatches high-energy sound waves. The sound waves reflect on the internal organs or tissues and form echoes. The combination of the echoes of tissue makes a sonogram picture. TRUS is used to find abnormalities in the rectum and its adjacent areas. Since the prostate is located anterior to the rectum, the probe can scan it if inserted inside the rectum and through the rectum wall. It can maneuver in and out of the rectum and enable during brachytherapy to observe the target in a live image.

Side-firing, end-firing, and 3D probes are three common types of TRUS probes. They vary based on the orientation of the tip of the probe (the needle). In the side-firing probes, the needle is oriented longitudinally. The direction of the biopsy in this probe is around the craniocaudal axis. Therefore, sampling the gland in the transverse axis will face some challenges. Also in the side-firing probe, the lateral peripheral zone and the apex are sampled using some significant torques.

In end-firing probes, the needle is located at the tip of the probe without angle. The curved tip of this probe makes the visualization of the prostate on the transverse plane easy. It has also shown to be more sufficient and improve cancer direction rates since it facilitates the reach to the ventral and apical aspects of the prostate.(17)

The 3D probe has the advantage of using a combination of both axial and sagittal planes. As a result, it is possible to generate a full 3D volume with a motorized angular sweep. However, the timing of the image acquisition in 3D-TRUS is more than its 2D counterparts. It leads to lower frame rates.

The grid template of the TRUS is located on the TRUS stepper. It guides the physician during the needle insertion process. The stepper makes sure that the TRUS probe is always moving perpendicular to the grid template. It captures TRUS images parallel to the grid

(16). (15)
Detecting a malignant hyper or hypo-echoic lesions using just TRUS images is a challenging task. For instance, it is estimated that a hypo-echoic region identified on a TRUS has a seven to 57 percent chance of being malignant which results in false-positive PCa diagnoses. Overall, TRUS-based screening suffers low sensitivity and specificity with the respective percentages of 35-91% and 24-81%. These estimations increase the requirement of repeating the biopsy until cancer is detected. (18) and (19)

2.3 PCa diagnosis and treatment

2.3.1 Biopsy

A prostate biopsy is an out-patient procedure to harvest and analyze the suspicious tissue samples. This is one of the vital procedures for diagnosing prostate cancer. It is usually recommended in cases of reporting abnormality on the results of the DRE and PSA tests. During the procedure, a biopsy needle is guided by an end-firing TRUS probe through the rectal wall to collect a number of tissue samples from the prostate gland. The current sextant protocol limits the standardized biopsy samples from eight to twelve cores depending on the extent of the gland. On areas with hyperechoic lesions that are located beyond the predetermined area for the standardized biopsies, more cores are considered. (20) (21)

Unfortunately, the chance of missing a cancer case by 12-core sextant biopsy procedures is estimated as more than 30% (i.e., false-negative rate) (22). Even though collecting more samples could improve this rate, it is not always possible. This is because the number of cores is correlated with multiple factors such as pain, risk of infection, duration, and cost of the procedure. In general, TRUS images fail to visualize 40-70% of the PCa tumors which leads to the low sensitivity of the biopsy (23). In addition, the accurate needle placement requires a certain level of expertise in interpreting TRUS images due to the poor spatial information provided by these images.

2.3.2 Brachytherapy

Brachytherapy is a type of radiation therapy that is considered as one of the treatment procedures for prostate cancer. During the procedure, a radioactive source is placed directly inside or next to the organ or tissue disposed with cancer. Brachytherapy can be based on low-dose-rate (LDR) or high dose rate (HDR) techniques.

In LDR brachytherapy, small radioactive seeds are implanted as a source of radiation, directly

into the prostate gland for several days or even permanently. LDR brachytherapy is some times applied along with external beam radiation therapy (EBRT) as a boost.

In HDR brachytherapy, several implant catheters and radioactive materials are inserted inside the prostate temporarily for a few minutes and then removed. In HDR, the source position can be precisely adjusted and customized doses can be distributed specifically to each patient's need. Therefore, the tumors can be treated with high doses of localized radiation while the chances of emission on healthy tissues are reduced.

One of the critical facts during the operation is that the catheter should be precisely inside the prostate and it should not cross the urethra. Thus, the radio-oncologist needs to know exactly where the tumor is while inserting the needles. Transrectal Ultrasound (TRUS) imaging of the prostate is the routine clinical approach for guiding surgical interventions.

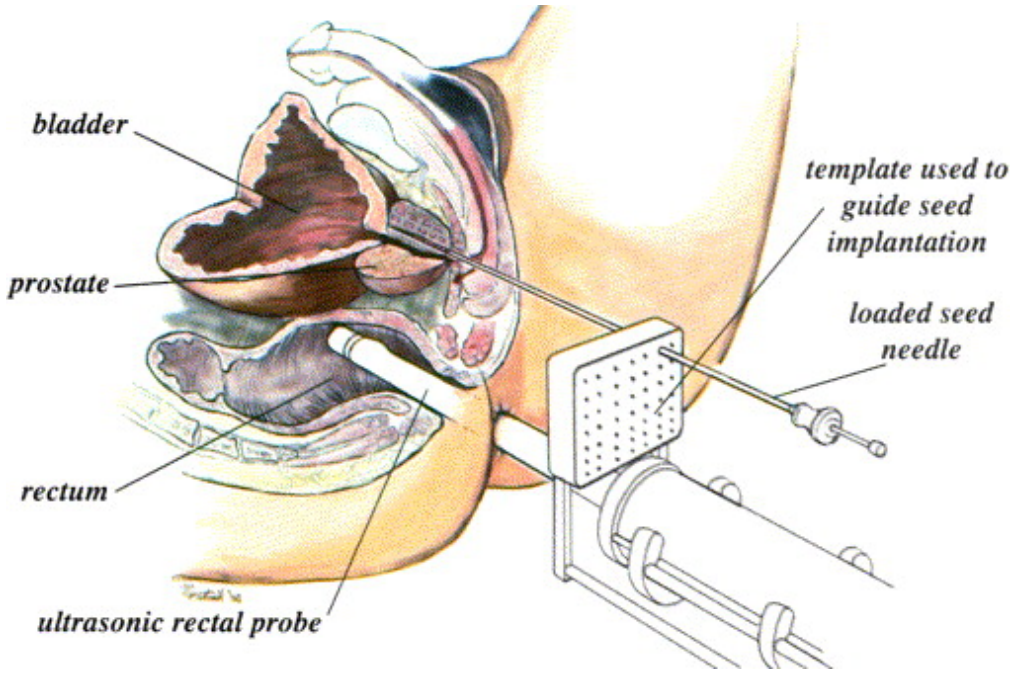

FIGURE 2.3 Prostate cancer treatment with radioactive seed implantation (2).

2.4 Image-guided diagnosis and treatment techniques

As mentioned in the previous section, there is a crucial need for an imaging technique in guiding the clinicians to localize the brachytherapy/biopsy needle. This is done by providing a high-quality pre-operative scan and using it as a reference to localize the organ in real-time

TRUS images. Usually, a high-quality modality like MRI is chosen to provide high-resolution information about the prostate organ. Then, an image registration technique is applied to match the pre-operative scan to the intra-operative TRUS image.

Image registration is an image processing technique where two or more images taken from the same scene are fused to each other. It is one of the most used approaches when it comes to analyzing and integrating information from various timings, sources, and situations. The various intensity and geometrical based registration approaches have been introduced in order to non-rigidly register a pre-operative MR image (Source) to its intra-operative TRUS image (Target), which can be combined with an optical or electromagnetic tracking system to navigate devices. Section 2.4.1 presents this intensity and geometrical based fusion approaches. In addition, Section 2.4.2 describes the automatic segmentation approaches that have been proposed in the literature to segment the TRUS images. These automatic segmentation approaches have been used in geometric-based registration techniques.

2.4.1 MRI-TRUS fusion approaches

Intensity-based registration methods adopt correlation metrics to compare and analyze the intensity patterns between the two modalities. In these approaches, the whole image or sub-images are registered.

The poor signal to noise ratio of the TRUS image and the complex intensity correlation among TRUS images and MRI make the task of intensity-based registration a challenge. Furthermore, one of the crucial requirements of the intensity-based approaches is that the corresponding anatomical features being visible in both imaging modalities. However, due to the variations of imaging physics, there may be parts of the anatomy that can be visible in one image but not in the other. For example, the boundary of the prostate is not clearly distinguishable at the base in TRUS modality, while this is not the case in MRI (24).

A geometric feature-based registration method or a surface-based registration method seeks the optimal correspondence between surface features such as points and lines. It determines a geometrical transformation to map the source image to the target image. The optimal fusion from MRI to TRUS images is computed by detecting the whole organ on both imaging modalities and then registering the structures. Thus this method is ideal for the cases where both pre-operative and intra-operative images are segmented during the clinical process. One advantage over the intensity-based approaches is that it eliminates the search for the intensity-based correlation. The initial surface-based registration methods genuinely depend on manual landmark selection. However, the process of manually selecting the landmarks or boundaries is time-consuming, monotonous, and subject to human error.

A real-time method that does not require any fiducial markers was designed by (25) for a guided prostate biopsy process. Here, they had two pre-operative modalities : a pre-operative 3D endorectal coil MRI and a 3D TRUS image (it was acquired by sweeping the 2D probe across the organ). A manual rigid body transformation registered these two images to superimpose the MRI image onto the TRUS image. Then, the intra-operative 2D US was registered to the reference US volume. The final fusion was computed based on the minimum of a sum of squared distances between the new ultrasound (3D) and the reference ultrasound (set of 2D frames). The corresponding 2D images were then registered using the image gradient and correlation coefficient (CC) based registration method. A data set of 20 patient data was used for this approach. The average computation time for their study was computed as 101 ± 68 s. The average overlap improved from 70 ± 18 to 90 ± 7 after fusion (19 ± 11). In another study, (26) manipulated distributed and grid computing approaches to perform an image-based registration. They computed the tissue deformation between intra-operative 3D TRUS and pre-operative MRI volume.

(3) aligned the pre-biopsy 3D MRI with intra-biopsy TRUS volume using elastic matching. The method required fixed manual anatomical landmarks on the apex and base of the prostate to rigidly register the two volumes. Then the surfaces were fused using a block matching approach and defining moving image deformation using a regular, 3D grid of B-spline control points ((27) and (28)). The elastic interpolation followed the dynamic contrast enhancement and diffusion-weighted imaging. This approach was evaluated on 47 patients which led to a mean target registration error (TRE) of 2.09 ± 0.77. Figure 2.4 shows a diagram of this fusion framework.

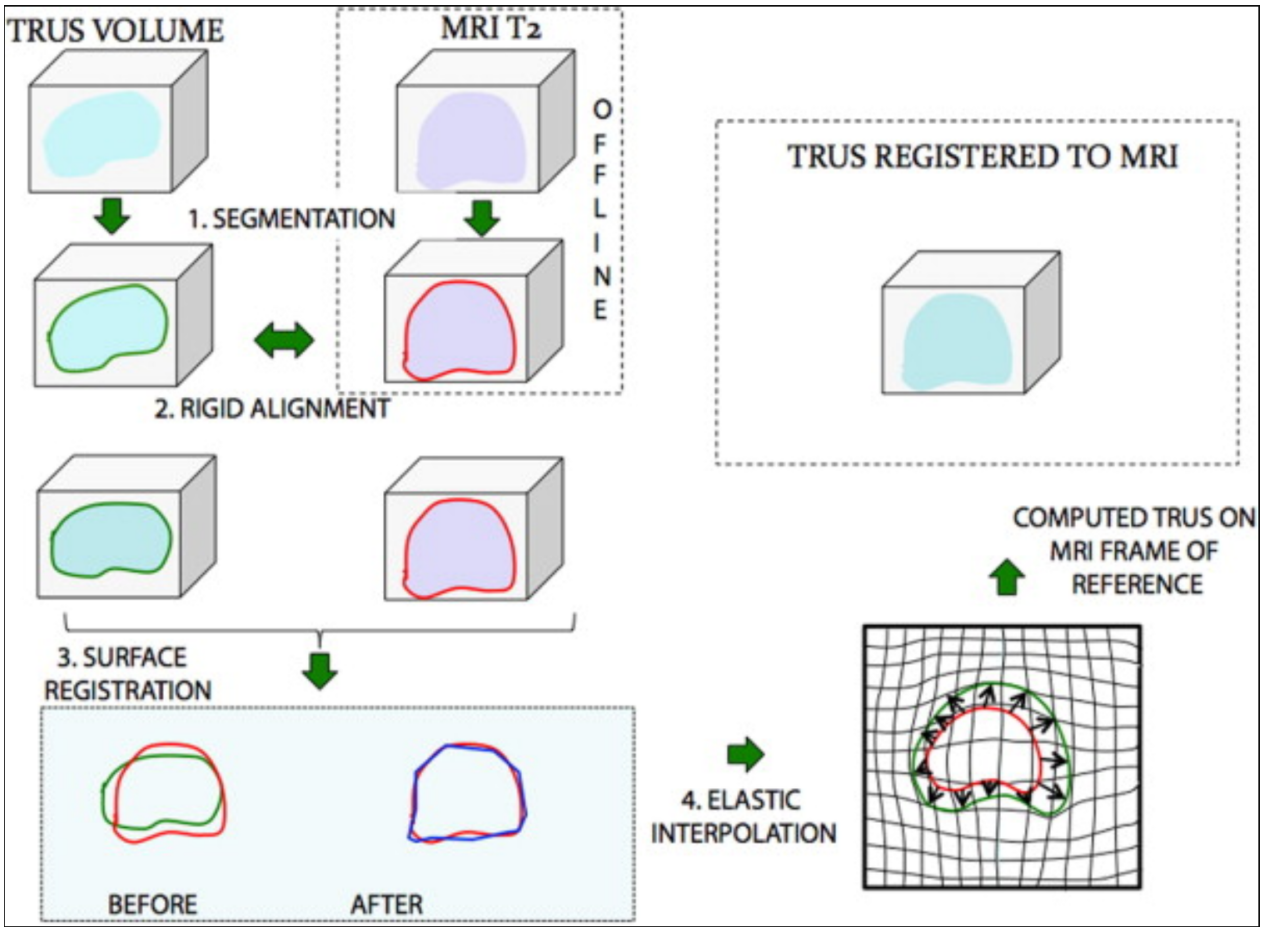

FIGURE 2.4 Process of MR-TRUS fusion. MR and TRUS images were segmented (1) and then rigidly aligned (2). Fusion then proceeded, involving a surface registration (3), and elastic (non-rigid) interpolation (4). Based on reference (3)

(29) registered the 3D endorectal coil MRI volume (with deformed prostate) with undeformed MRI volume. This approach used manual correspondences to apply intensity-based Thin-Plate Splines (TPS) (30), (31) to perform the fusion. However, the study only presented the qualitative results in terms of the checkerboard overlap. (32) used an octree spline elastic method to register TRUS and MRI volumes for brachytherapy planning. A total of four patients in a dataset was used and the average TRE of 2.07 ± 1.57 mm was obtained. A similar approach by (33) used both rigid and non-rigid registration for the alignment of MRI with TRUS, yielding an average residual distance for the surface points of 1.11 ± 0.54 mm on 11 patients. In (34), a B-spline approach was proposed to register the histology prostate slices to MRI slices to detect prostate cancer. Given the fact that the main focus of the paper was on cancer detection, no quantitative results were reported. (35) proposed a method that forms a spatial atlas of the prostate with B-splines and TPS algorithms (30). Oguro and his

team employed B-spline based deformations to non-rigidly register the pre-operative MRI to intra-operative TRUS during brachytherapy (36). This method was tested on 16 patient cases, achieving a Dice score of 0.91 and marker matching error of 2.3 ± 1.8 mm on the whole prostate gland. Amongst the approaches that have found automatically the corresponding fiducial pairs, the iterative closest points (ICP) method and its different variations are the most popular in the field. However, these methods suffer from a number of flaws such as being sensitive to initialization, outliers, and noise.

To address these limitations a variety of approaches have been adopted. In the work of (37), a stack of multi-slice 2D histological images is registered to 3D volumetric prostates using a particle filtering approach, computing probabilistic correspondences using a Gaussian mixture. (27) proposed two separate MRI-TRUS fusion approaches, one surface-based, and one intensity-based. The surface-based registration technique consisted of a rigid registration using ICP (38) and a non-rigid registration based on TPS algorithm (30). They also performed an image-based fusion using the block-matching technique introduced by (39) for rigid registration and 3D Bspline uniform grids for non-rigid registration. A dataset of 16 patients was used to evaluate the accuracy of the method. The reported average TRE was 2.09 ± 0.77 mm for the surface-based registration and 1.50 ± 0.83 mm for the image-based registration. A 3D TRUS volume to 3D MRI was accomplished with two approaches in (31). Both methods perform 2D intensity-based registration based on image textures. In the first approach, a TPS algorithm was employed to register MRI to TRUS. This method was tested on a dataset of four patients and achieved the Dice score of 0.97 ± 0.01mm. Then, a B-spline based registration was developed that maximized mutual information of quadrature local energy of the modalities. The method was tested on a dataset of 18 patients with a Dice score of 0.94 ± 0.39 and TRE of 2.64 ± 1.37 mm (40) and (41). (42) proposed a non-rigid MRI to TRUS registration. In this method, a TPS algorithm followed a rigid point matching on the manually placed corresponding landmarks. The average TRE of 2.24 ± 0.71 mm was reported after the evaluation of the method on 17 patient data. Kaplan et al. rigidly registered a set of axial pre-operative endorectal MRI slices with the axial intraoperative TRUS images. The method was introduced to assist the needle insertion in a biopsy procedure. During the process, some fiducials were chosen manually on both MRI and TRUS images and the registration method tended to minimize the distance of the corresponding markers. The method was validated on a dataset of two patients with only qualitative registration outputs. (4)

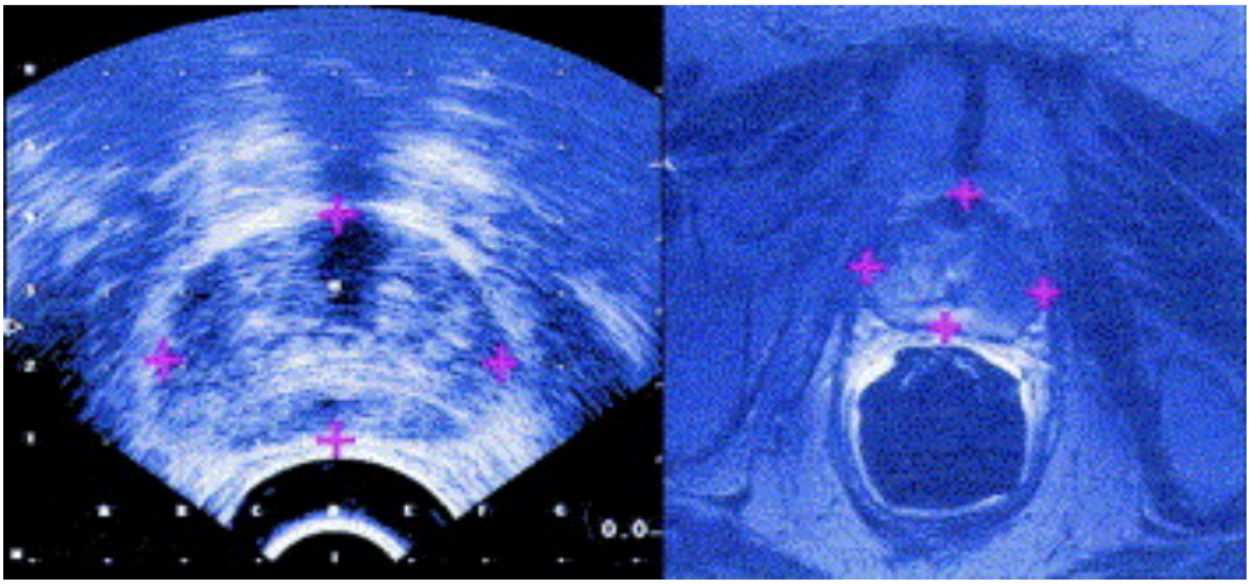

FIGURE 2.5 A sample of fiducial points on the a MRI and an ultrasound image for performing the fusion. Based on (4).

(43) presented a deformable landmark-based registration method that employed thin-plate splines in order to overlay the suspicious MRI lesions on the 3D TRUS image in real-time. The combined rigid registration along with the TPS deformation was used to fuse the 3D TRUS with 3D MRI. Their approach was evaluated on 25 patients who underwent mechanically-assisted prostate biopsy. It resulted in a TRE of 4.3 ± 1.2 and showed significant improvement compared to the ICP based approach .

(44) employed a model-to-image approach to match the MRI volume with the TRUS volume. Before the biopsy procedure, a biomechanical finite element based statistical motion model (FMM) was trained on the pre-operative MRI volume. It contained the possible random deformations of the prostate gland that was induced by the TRUS probe. This FMM was then used as a prior in the deformation of the registration to constrain the matching process. The registration algorithm was based on maximizing the likelihood of the FMM model that was obtained from the MRI. The method was evaluated on a data of eight patients and the median final Root Mean Square Error (RMSE) was reported as 2.40 mm. (24) and (45) used a Patient-Specific Statistical Deformation Model (PSSDM) instead of a biomechanical model. The method used a simulated finite element deformation model that was trained on the manually segmented prostate anatomy. They have adapted the robust point matching (RPM) (46) (47) framework to perform SDM registration. The Dice overlap was estimated at 0.85 ± 0.18 and a median target registration error of 2.98 mm. In the approach proposed by (48) both MRI and TRUS surfaces were mapped into a mutual space which was a topologically

equivalent space. The accuracy of their proposed approach was highly sensitive to regions with missing data. For instance, the areas that were mostly adjacent to the apex of the prostate were due to poor contour visibility.

A non-rigid deformation consists of a vast domain of possible solutions. Thus, many algorithms require a regularisation factor to assist the deformation field to converge. Khallaghi and his team proposed a method based on the finite element model (FEM) for non-rigid registration between MRI and TRUS. They achieved the target registration error (TRE) of 2.98 mm and a Dice score of 89.4. Yan and his colleagues have introduced an adaptive shape model-based method (ADSM) (49). In this method, they have updated the shape model adaptively during the segmentation of the patient's image. The Dice score of their method was 85.7 %. (50) proposed a registration technique based on a lesion-specific, anisotropic preconditioned similarity metric using SDM with 50 auto segmented patient data. Their final landmark registration error was reported to be 1.41mm. (5) trained a similarity metric of the MRI-TRUS fusion using a deep convolutional neural network (CNN). Their implicit optimization benefits the solution space in order to obtain the best initialization. It then smooths the metric for optimization using a multi-pass technique. This method reached the mean TRE of 3.86 mm. In a recent work (6), authors fused MRI to TRUS with a weakly supervised algorithm. This method was originally inspired by a viscous fluid physical model. They have first combined the CNN and LSTM neural networks and predicted the dense deformation fields. This method was validated on 66 patient data with the mean TRE of $2.85 \pm 1.72mm$.

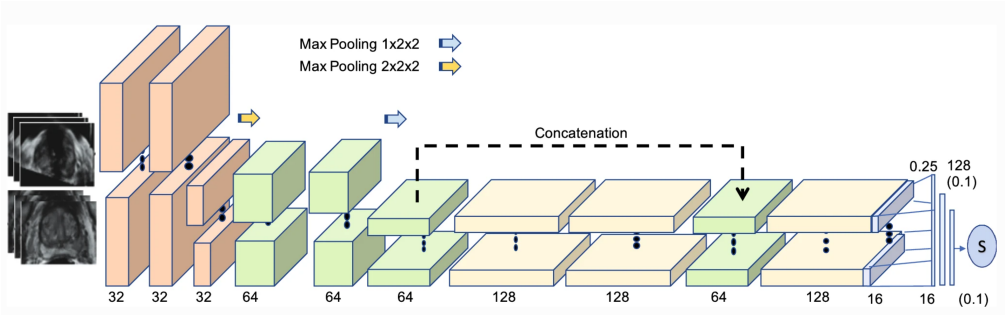

FIGURE 2.6 The CNN architecture designed by (5) that learns the similarity metric of the image.

2.4.2 Auto segmentation on TRUS

As mentioned in the previous section, the surface-based registration approaches typically rely on identifying the target gland. This segmentation process can be performed manually,

semi-automatically, or automatically.

The majority of current registration approaches lean on manual segmentation. However, manual segmentation of the TRUS images is a tedious and time-consuming process, which is subjected to variation and error.

Previous studies have proposed a number of solutions for the automatic segmentation problem. Recently, deep learning algorithms have become a popular methodology of choice for analyzing medical images. Convolutional Neural Networks (CNNs) have recently led to significant advances in the automatic segmentation of medical images. A wide variety of network architectures are now available to the research community.

However, in the case of prostate image segmentation, especially TRUS segmentation, it is still challenging. One reason is that the prostate is a flexible organ, so the TRUS probe's pressure could easily change the shape of the prostate (Figure 2.7). Apart from that, the exact shape of this gland varies from one person to another, especially in the presence of a tumor. This leads to difficulties in developing an accurate automatic segmentation approach.

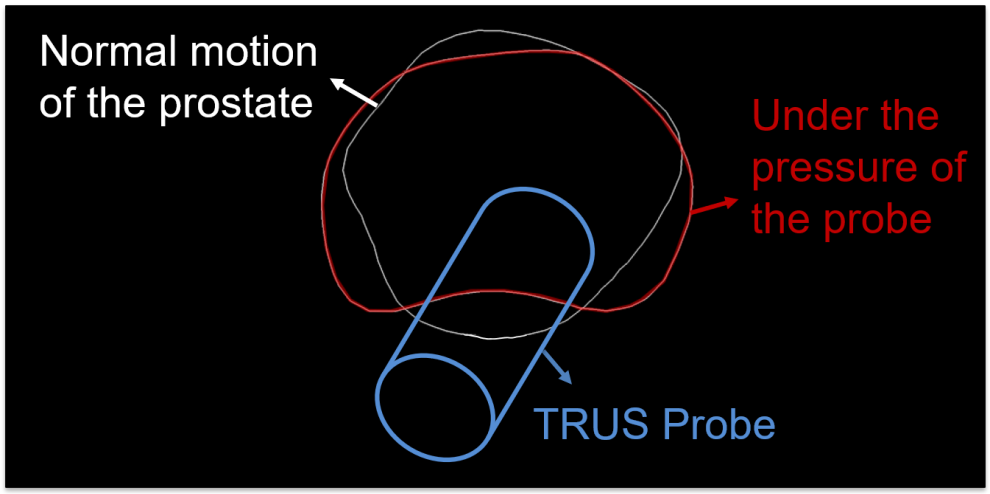

FIGURE 2.7 Some variability of the prostate segmentation is caused by the pressure from the prostate probe.

In (9), authors designed a segmentation method that benefits the advantages of both Convolutional Neural Networks(CNN) and ResNets called FC-Resnet. The data pre-processing was performed by a low-capacity FCN model that normalized the input medical image that iteratively was refined by means of a FC-ResNet while training to predict a segmentation.

In another work, Wang et al. (51) proposed a Deep Attentional Feature (DAF) approach. They relied on DA features to better integrate multi-scale features so that more relevant

information is amplified while suppressing noisy and irrelevant features. They have reached the total dice score of 90.6% for the whole gland.

(52) compared the TRUS-based prostate segmentation used in the treatment of 598 patients with a high-quality MRI prostate atlas and observed inconsistencies at the apex and base. Motivated by this finding, they proposed an alternative TRUS segmentation technique that was fully automatic and used MRI as priors. The method used a convolutional neural network to segment the prostate in TRUS images at mid-gland, where the gland boundary could be clearly seen. It then reconstructed the gland boundary at the apex and base with the aid of a statistical shape model built from an MRI atlas of 78 patients. Figure 2.8 illustrates the diagram or their approach.

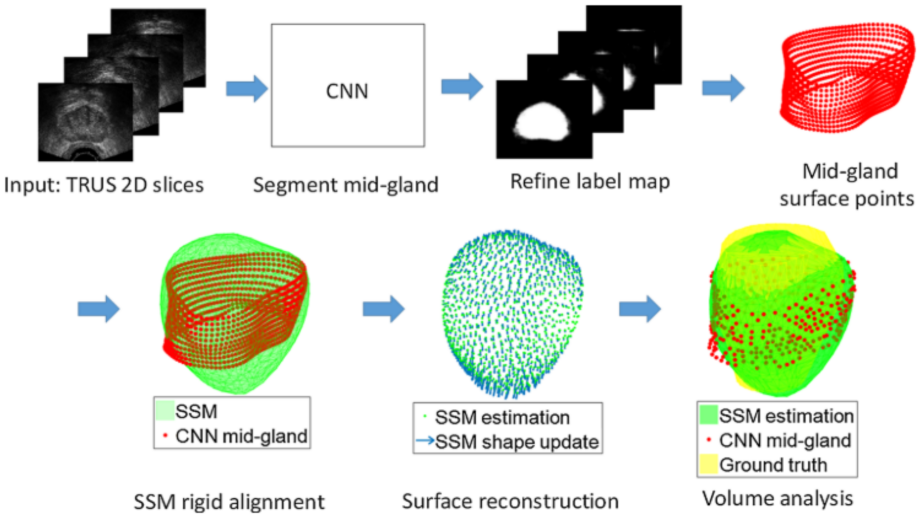

FIGURE 2.8 A step by step illustration of the automatic segmentation method proposed by Zeng and his team (6).

Karimi et al. (7) proposed a CNN based approach for automatic segmentation of the prostate in transrectal ultrasound (TRUS) images for brachytherapy. This method was based on a U-Net architecture (53) with adaptive sampling. They have also defined the uncertain areas with SSM. On the dataset of 675 TRUS images of the prostate with five-fold cross-validation, the Dice score of $93.9 \pm 3.5\%$ is obtained.

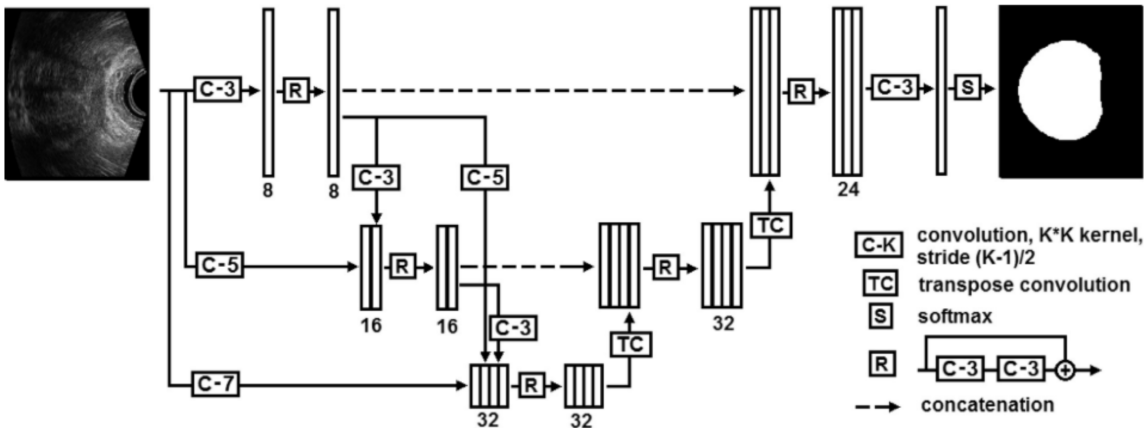

FIGURE 2.9 The CNN architecture proposed by (7). This network is of depth5 LeakyRelu was used for the activation function.

2.4.3 Summary

We can conclude that among different MRI-TRUS fusion approaches in the literature, surface-based approaches have enabled the most reliable fusions compared to the intensity-based methods. However, going through the fusion accuracy measures reported in previous studies, we realize that there is still a need for improving MRI-TRUS fusion approaches, particularly with regards to the workflow.

As mentioned in this section the accuracy of the surface-based fusion approaches can be improved by modeling the variation of the prostate shape. In addition, the performance of a surface-based approach can be improved by employing a precise segmentation on both MR and TRUS images. Although the segmentation on MRI can be done manually in offline mode. At least, the TRUS segmentation requires an accurate automatic approach.

2.5 An overview of registration and deep learning algorithms

In this section, some of the common algorithms named in the literature and the proposed methods are introduced.

2.5.1 Affine transformation

Affine transformation is one of the simplest transformation models. The translation, the rotation, and the scale of the image are the nine parameters involved in this linear transformation model. Equation (2.1) demonstrates the mathematical expressions of this method :

$$T_{affine} = \begin{bmatrix} \delta_{11} & \delta_{12} & \delta_{13} \\ \delta_{21} & \delta_{22} & \delta_{23} \\ \delta_{31} & \delta_{32} & \delta_{33} \end{bmatrix} + \begin{bmatrix} x \\ y \\ z \end{bmatrix} + \begin{bmatrix} \delta_{14} \\ \delta_{24} \\ \delta_{34} \end{bmatrix} \tag{2.1}$$

2.5.2 Iterative Closest Point (ICP)

Iterative closest point (ICP) (38) (54) is a point cloud registration method that starts from an initial location and minimizes the spatial transformation between two point clouds in order to align them. It generally assumes that points with minimal distance between each other correspond to each other.

The main idea of this method is to find the center of mass using the points with existing corresponding points, shift the points up against each other, and then compute the optimal rotation using a SVD approach so that the points are properly aligned until it converges with the optimal rotation and translation. Here, data estimation has a crucial role. Errors in data association prevent the alignment to reach an accurate and perfect state. An ICP method is generally sensitive to noise, initialization, and outliers.

Non-rigid ICPs are a modified version of the rigid ICP framework. In the method proposed by (55), the source template is gradually deformed towards the target by using a series of decreasing stiffness weights where the nearest point search estimates the initial correspondence. Then, the optimum rotation and translations of the source to target are computed. A locally affine transformation regularises the deformation of each vertex and keeps the transformation differences between neighbors to a minimum.

The method considers three factors to form a cost function. A distance term, a stiffness term, and a landmark cost.
The distance cost function from the deformed template and the target is defined as in equation (2.2) where it potentially needs to be small :

$$E_d(X) := \sum_{v_i \sim v} w_i dist^2(T, X_i v_i) \tag{2.2}$$

Considering $X = \{x_1, x_2, x_3, ...x_n\}$ as the affine (rotation and translation) transformation matrices of size 3 by 4 for each vertices. The template vertices are defined as $v_i = [x, y, z, 1]^T$. Here, $dist(T, v)$ denotes the surface. If a corresponding point for a vertex is unknown, the w_i is set to 0.

A stiffness contributor regularizes the distance function. Here, the differences of the transfor-

mation is weighted by $G = diag(1, 1, 1, \gamma)$ and is penalized under the Frobenius norm 4.11. The term γ weights the rotational and diagonal differences against partial deformations. It relies on the units of the data and on the type of deformation :

$$E_s(X) := \sum_{i,j \sim \varepsilon} \|(X_i - X_j)G\|_2^F \tag{2.3}$$

The landmark term initializes the registration. It basically maps the template vertices into the target surface using a set of landmarks : $L = \{(v_{i_1}, l_1), ..., (v_{i_l}, l_l)\}$, such that :

$$E_l(X) := \sum_{(v_i,l) \sim L} \|X_i v_i - l\|^2 \tag{2.4}$$

A weighted sum of these three functions form the cost function used in the non-rigid ICP (equation 2.5) :

$$E(X) = E_d(X) + \alpha E_s(X) + \beta E_l(X), \tag{2.5}$$

where the α coefficient affects the flexibility of the template and β effects the elimination of the noisy landmarks where needed. The process of minimizing the function is performed in the following steps using a non-rigid optimal ICP (55) , (56) :

1. An initial point correspondence is provided (X_0)
2. For each stiffness α of $\{\alpha_1, ..., \alpha_2\}$ in increasing manner, perform the following steps :
3. Until the distance between x and its corresponding pair is minimum (less than ε) : (Here, the deformation of the template is defined to set the template in the nearest possible distance to the target)
   (a) Find the preparatory corresponding points of $V(X^{j-1})$
   (b) Set the current optimal deformation for the initial correspondence as α_i
   (c) Repeat (a)-(b)

2.5.3 Spline-based registration

In most medical image processing tasks, the local features are significant. These features are subjected to differ between patients and are sensitive to the physical characteristics of the prostate. Simulating these deformations is challenging. An affine transformation ignores these qualities since it is focused on global deformation. Free Form Deformation (FFD) models plain deformations of the objects. The method consists of enclosing the object within geometric shape(s) such as a cube, cylinder (57), (58). As the cube transforms, the object deforms along

a set of control points on the surface of the object. The process of transforming the cube is based on the hyper patch concepts like B-Spline and Bezier curves (59). As a robust tool in 3D deformable modeling, the FFD model based on a B-spline hyper patch is a useful local deformation model(60),(61). Given the amplitude of the image volume as equation (2.6), a B-spline based FFD is described as Eq. (2.7) :

$$\theta = \{(x, y, z)|0 \leq x \leq X, 0 \leq y \leq Y, 0 \leq z \leq Z\} \tag{2.6}$$

$$T_{nongrid}(x, y, z) = \sum_{i=0}^{3} \sum_{m=0}^{3} \sum_{n=0}^{3} B_l(u) B_m(v) B_n(w) \Phi_{i+l,j+m,k+n} \tag{2.7}$$

where,

$$i = \lfloor x/n_x \rfloor - 1, j = \lfloor y/n_y \rfloor - 1, u = x/n_x - \lfloor x/n_x \rfloor, v = y/n_y - \lfloor y/n_y \rfloor, w = z/n_z - \lfloor z/n_z \rfloor \tag{2.8}$$

and,

$$B_0(u) = (1-u)^3/6, B_1(u) = (3u^3 - 6u^2 + 4)/6, B_2(u) = (-3u^3 + 3u^2 + 3u + 1)/6, B_3(u) = u^3/6 \tag{2.9}$$

Here, $\phi_{i,j,k}$ denotes the control points with uniform spacing of a mesh ϕ when ϕ is of size n_i, n_j, n_k. Unlike bazien based approaches, a local alteration in the control point will solely affect the region around the local neighborhood of that control point. The control points are considered the parameters of this model. Since B-spline is locally controlled larger number of parameters increases the computational efficiency of this approach (62), (63).

2.5.4 Machine learning methods

Statistical Shape Model (SSM)

Statistical Shape Models (SSMs) are based on Principle Component Analysis (PCA) that describes the linear connection of the data using their anatomical variation features. It is one of the common approaches to quantitatively analyze a deformable shape. The main assumption of this approach is that each object in the data is a variation of the reference shape and is represented in form of a point cloud or a set of landmarks, as descrtibed in (64), (65).

SSMs are primarily based on the parameters of PCA. Once the variation sets are computed,

the SSM is defined as below :

$$S = \bar{m} + \lambda b \tag{2.10}$$

where $\bar{m}$ represents the mean shape (Eq. 2.11), n is the number of data and λ is the matrix of orthogonal eigen-vectors (Eq. 2.12) and b is a vector of model coefficients :

$$\overline{m} = \frac{\sum_{i=1}^{n} s_i}{n} \tag{2.11}$$

$$\lambda = \frac{\sum_{i=1}^{n} (s_i - \bar{m})}{n-1} \tag{2.12}$$

Auto-Encoder (AE)

The Auto-Encoder (AE) is an unsupervised feed-forward generative neural network that is trained to learn efficient data coding. The main purpose of this model is to reduce the dimension of the data and reconstruct the original data subsequently. It basically consists of two stages : an encoder and a decoder (i.e. Figure 2.10). An encoder maps the input x into a low-dimensional latent state space (hidden layer) h (Eq. (2.16)). The decoder produces $x^{'}$ using h, with minimum difference from x (Eq. (2.14)), resulting in $x = x^{'}$. The network tends to minimize the 2.17 loss function to reach the optimum value of W :

$$E : Input \rightarrow h \tag{2.13}$$

$$h = \sigma(W.x + b_x) \tag{2.14}$$

$$D : h \rightarrow Output \simeq Input \tag{2.15}$$

$$x^{'} = \sigma^{'}(W^{'}.h + b_h^{'}) \tag{2.16}$$

$$Ł(x, x^{'}) = \left\| x - x^{'} \right\|^2 = \left\| x - \sigma^{'}(W^{'}(\sigma(W.x + b_x)) + b_h^{'}) \right\|^2 \tag{2.17}$$

where h is latent representation, σ is an element-wise activation function, W is a weight matrix and b is a bias vector. Rectified Linear Unit (ReLU) and sigmoid are the typical activation functions used in a simple autoencoder. It is proven that AE and PCA are closely

related. With a linear activation function within each layer of the AE, the latent variable at the bottleneck (h) could correspond to the principal components from PCA. (66) shows how a linear autoencoder is both capable of computing the subspace measured by PCA vectors and computing the PCs. The latent space is normally of a lower size than the input or the AE learns the identity function.

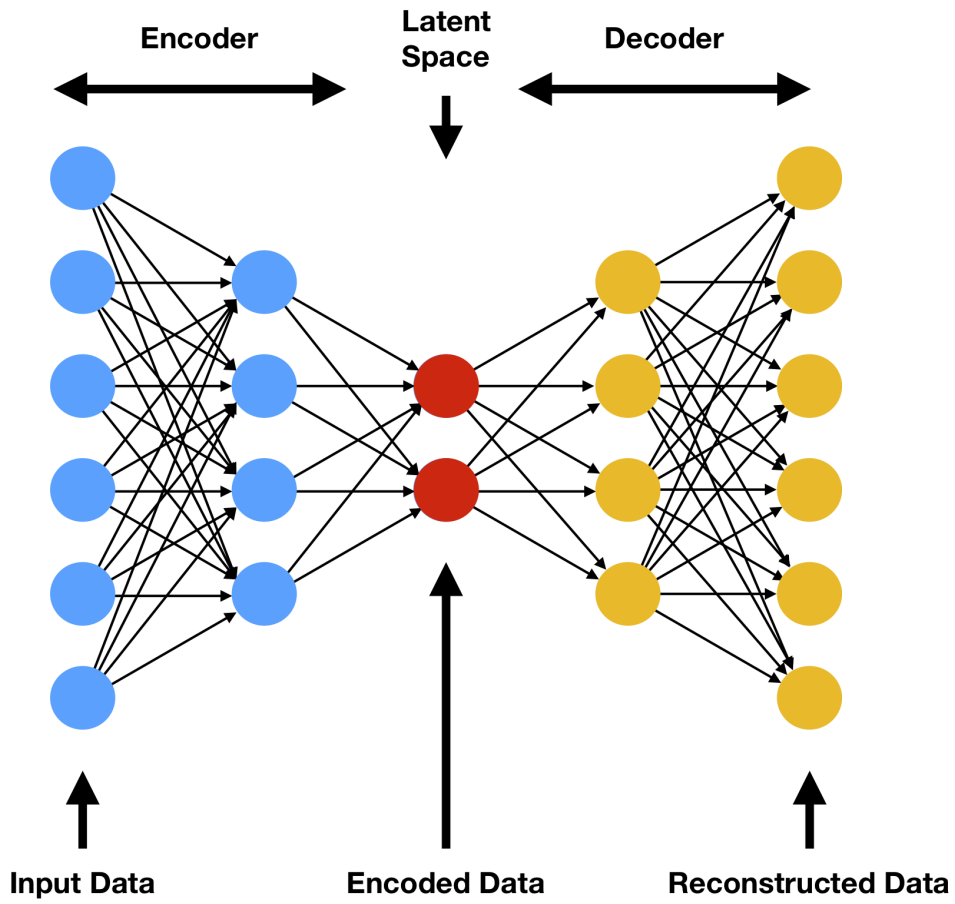

FIGURE 2.10 A prototype structure of a simple AE with 2 layers on each encoder and decoder block, input size of 1x6 and the hidden layer of size 1x2. https ://www.compthree.com/blog/autoencoder/

Convolutional Neural Networks (CNN)

U-Net

A U-Net (53) is basically a U-shaped semantic segmentation network that has the ability to compensate for missing image details using up-sampling and skip connections. The skip connections basically combine the high-resolution features from the sub-sampling (convolu-

tion) path with its corresponding features on the up-sampling path (deconvolution). Typically, because of these skip connections, it can reach more accurate segmentation results with fewer images (compared to convolutional networks). Figure 2.11, illustrates a simple U-Net architecture and the way its long skip connections work.

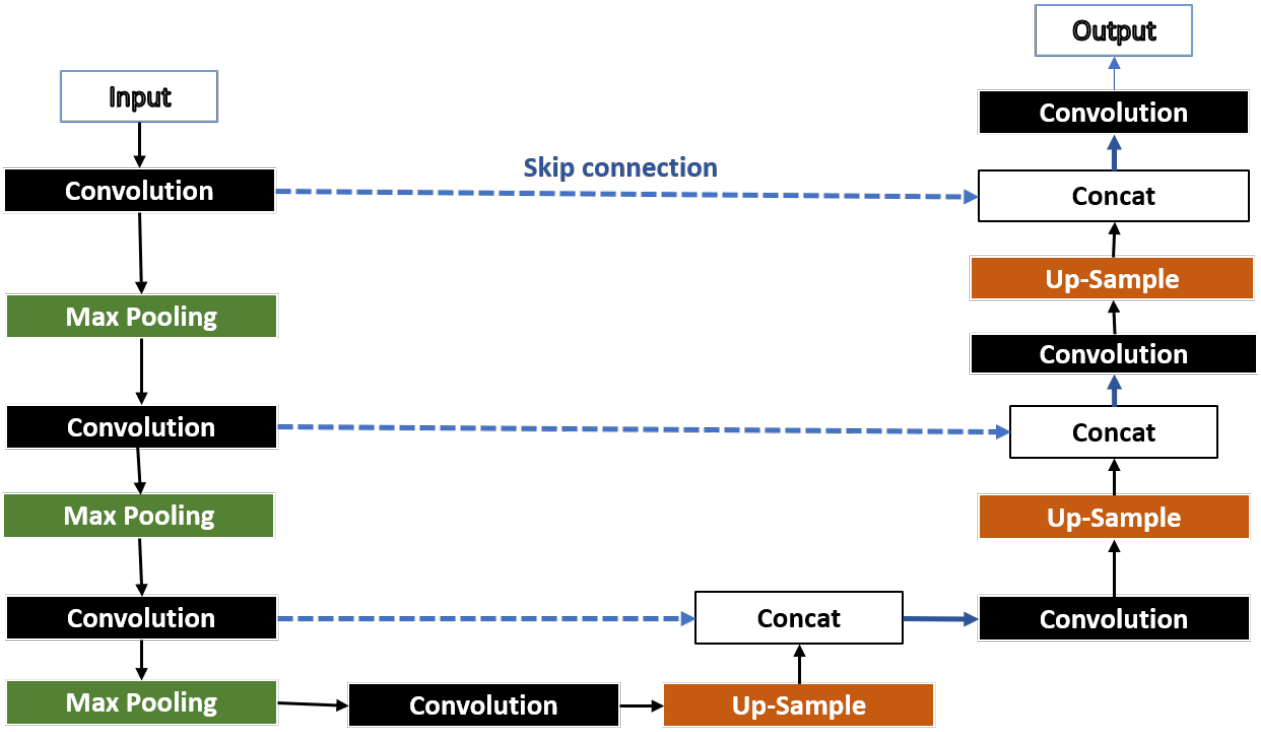

FIGURE 2.11 Schematic representation of the U-net structure.

In convolutional networks, a max-pooling layer is used in the down-sampling process. Its objective is to down-sample an input representation (image, hidden-layer output matrix, etc.), reducing its dimensionality and allowing for assumptions to be made about features contained in the sub-regions binned. One of the advantages of this layer is reducing the chance of over-fitting by providing an abstracted form of the representation. Max pooling is done by applying a max filter to (usually) non-overlapping subregions of the initial representation.

Res-Net

A deep residual learning framework (67) is the composition of residual blocks in a network model. Generally, the residual blocks in the ResNet architecture solve the degradation problem caused by the depth of the network. These residual connections can elevate the forward

and backward parameter conduction, reduce the computational complexity and improves efficiency. Given x_i as input, a typical block of a network is a stack of layers that directly fit a desired underlying mapping as $F(x_i)$ (See Figure 2.12). A residual block lets these layers to fit a residual mapping (Figure 2.12) where :

$$F(X_{i+1}) = F(X_i) + X_i \tag{2.18}$$

In a ResU-Net, the identity mappings are applied by shortcut connections that directly add up to the output of the stacked layers (Eq. (4.1)).

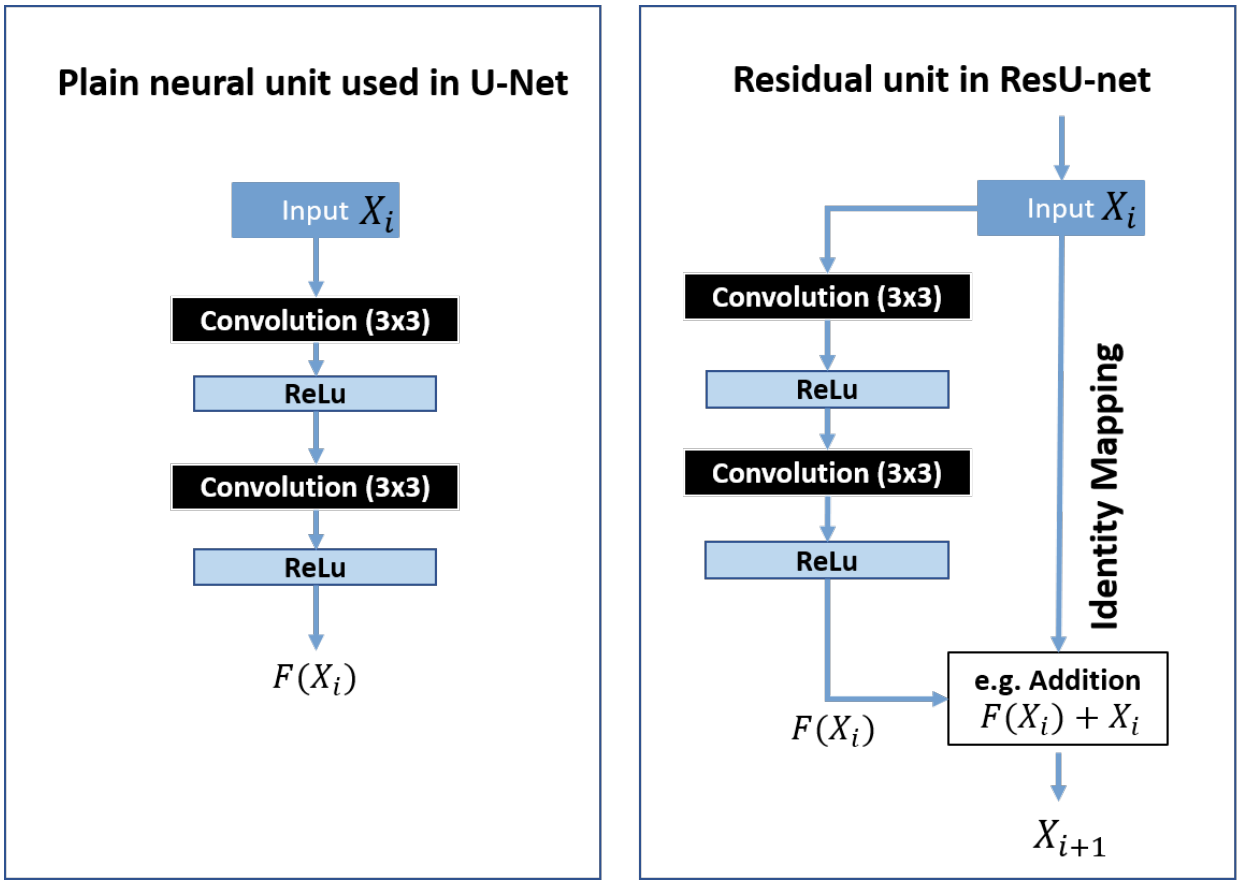

FIGURE 2.12 The difference between a regular convolutional structure (left) and a residual block (right).

CHAPITRE 3 RESEARCH OBJECTIVES and GENERAL METHODOLOGY

3.1 Problem statement

Prostate interventions require advanced imaging technologies to guide clinicians in localizing the tumor target accurately. Transrectal Ultrasound (TRUS) is one of the most common modalities for these procedures. However, it provides low-quality images. It leads to some challenges on recognizing the boundaries of the organ and the placement of the tumor and tissues. A pre-operative high-resolution image (e.g., MRI) can be used as the reference image. It provided more detailed information about the tissue of the organ and can help improve the proficiency of the performance. Here, the target organ (prostate) is a flexible gland. Factors such as the insertion of the Transrectal probe inside the rectum and the specific position of the patient while acquiring the TRUS image affect the general shape of the prostate by pressing the organ. This is while in MR images, that are taken without the Endorectal coil, the patient lies back and the prostate is in a more neutral position and shape. As a result, the organ appears differently in both images. It is ideal for the organ and the tissues in the reference image (pre-operative MRI) to be most similar to the current image (intra-operative TRUS). In fact, even one TRUS image with the same quality as the MRI can help improve localizing the biopsy or Brachytherapy needles.

A solution to this problem is to register the pre-operative MRI to the intra-operative TRUS. This fusion is also needed to map tumor location from the MRI onto the TRUS image, which is important to place brachytherapy needle to the correct location. Thus, if the registration operation has high accuracy, the registered MRI can perfectly replace the original MRI as a reference. This is because in the registered MRI the organ and the tissues are in the most similar state to the current TRUS image. The intensity-based approaches require the visible corresponding anatomical features in both imaging modalities while a geometric feature-based registration method seeks the optimal correspondence between surface features such as points and lines. As mentioned in the literature, The poor signal to noise ratio of the TRUS image and the complex intensity correlation among TRUS images and MRI make the task of intensity-based registration challenging. It does not imply that the intensity based approaches are impossible or dead-end for this task. However, in the cases where the prostate annotations for both modality is present, the geometric based approaches could be considered as less challenging approaches that could be effective as well((68)). Also, manually segmenting the TRUS image is both a time consuming process and is subjected to variation

due to human error. An accurate automatic segmentation of prostate organ on TRUS image could both help automating the process and accelerate it.

Accordingly, it is required to develop an accurate pre-operative/intra-operative registration approach. The important point is that this fusion method should consider the deformations of the various shapes that a prostate organ goes through during an intervention. Here, the question is that : *is it possible to design a pre-operative/intra-operative fusion framework based on deep learning, which models the prostate shape variations and is able to accurately delineate the boundary of the prostate organ on intra-operative images ?*

3.2 Hypothesis

Considering the given problem presented in the previous section, the following hypothesis can be formulated : *a pre-operative/intra-operative registration framework based on deep learning, modeling the prostate variation in an observational cohort, can yield similar accuracy levels to manual registration.*

3.3 Research objectives

The general goal of this thesis is to design a MRI to TRUS surface registration framework for prostate interventions based on deep neural networks and automatic segmentation of TRUS images.

Objective 1 : Perform the prostate segmentation on TRUS images using a fully convolutional ResNet model.

First, we aim to develop a dual neural network, consisting of a fully convolutional neural network (FCN), serving as a normalizing pre-processor of TRUS images across the training dataset. These pre-processed images are then segmented with a FC-ResNet, to automatically segment the prostate boundaries in the volume. This segmentation mask is then processed to generate a surface mesh model of the gland (including base and apex).

Objective 2 : Develop a MRI-TRUS surface registration approach using a statistical deformation model.

On one hand, MRI as a pre-operative scan provides high-quality information while TRUS produces low-resolution image. On the other hand, the prostate organ undergoes different amounts of variations. Thus, using a dataset of paired MRI-TRUS images, the deformation from MRI surface to TRUS surface can be modeled with a linear PCA model. Then, this deformation model can be used as prior information to regularize the MRI-TRUS surface registration for an unseen image pair.

The second objective is to model the deformation between the surfaces of the MRI and TRUS images using a statistical deformation model (SDM). The SDM approach assumes that the unseen deformation can be estimated by the linear combination of the deformations in the training set, and used as a regularizer during testing.

Objective 3 : Improve the MRI-TRUS surface registration framework using deep neural networks to model prostate shape variations.

Another way to model the prostate shape variations is to model the shape of the prostate on TRUS images using deep learning. The third objective will, therefore, train a deep autoencoder on a training set of surfaces originating from TRUS images. Auto-encoders (AE) learn to embed their input to a lower-dimensional representation and maps the reduced dimension to its reconstructed version. Unlike SDM, AE's with non-linear activation functions can model the non-linear combination of prostate variations. The trained AE is used to regularize the alignment between unseen surfaces of MRI-TRUS pairs.

3.4 General methodology

The SDM-registration approach consists of two phases : a training phase and a registration phase. The training phase is applied on a training set of paired MRI/TRUS images. First, surface meshes are extracted from the automatically segmented TRUS and MR images. Then, the extracted surfaces are aligned together using a Non-rigid surface registration. A vertex correspondence is established among all of the aligned meshes and a list of MRI/TRUS non-rigid surface deformation fields are extracted.

Once all MRI/TRUS surface displacement fields are extracted from the training set, a statistical deformation model (SDM) is trained. The trained SDM captures prostate shape deformations between MRI and TRUS surface meshes observed in the training dataset. Finally, the registration phase incorporates this trained SDM into the regularization process to perform the MRI-TRUS surface fusion on unseen patient data.

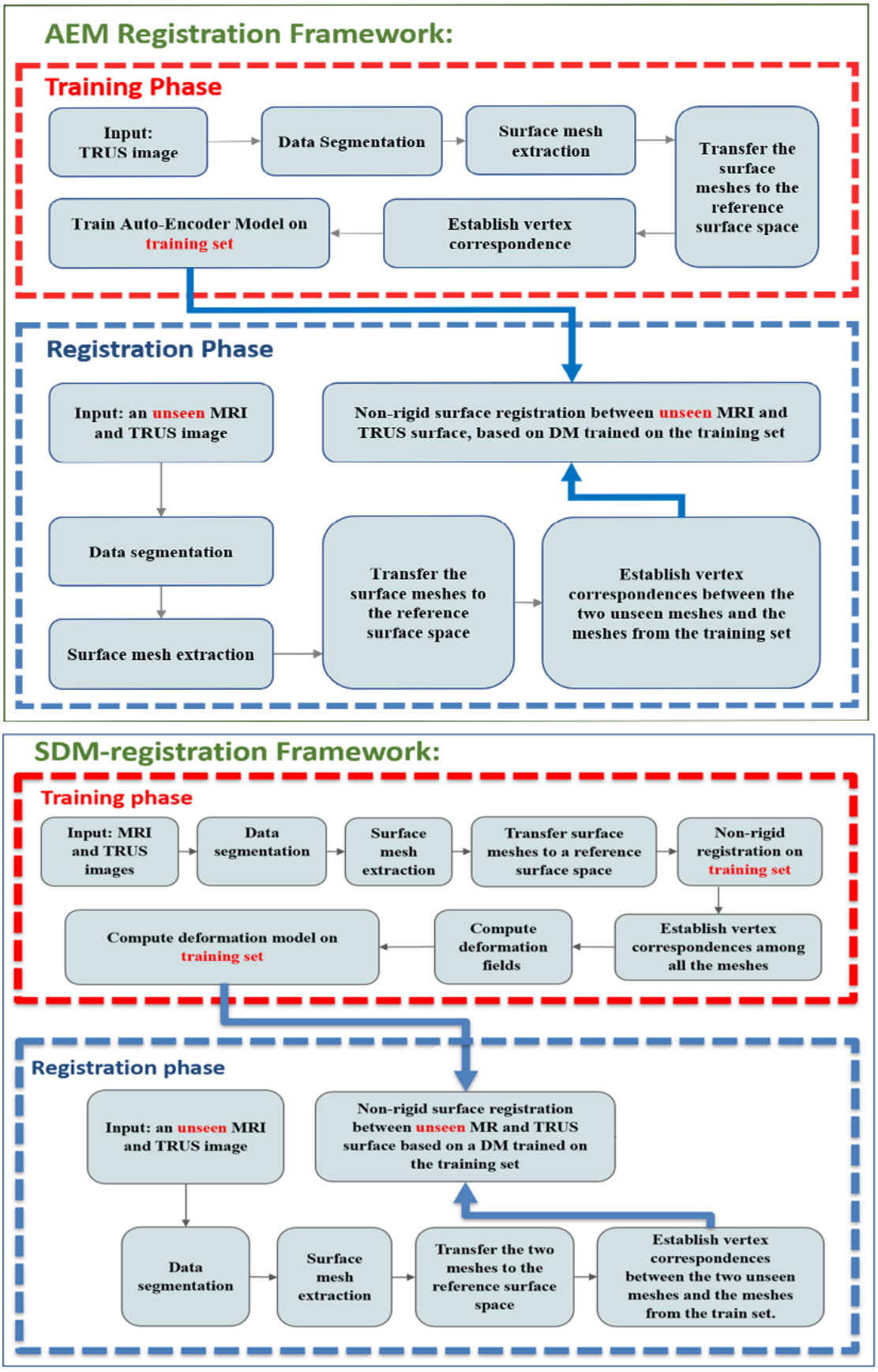

FIGURE 3.1 Schematic illustration of the proposed registration framework.

The AEM-registration method also includes two steps : a training phase and an online registration step. The training step first extracts surface meshes from automatically segmented TRUS images in our training set then trains a deep autoencoder to learn the prostate shape variation on TRUS. The autoencoder compresses and encodes data in a lower-dimensional latent space. In addition, it learns how to reconstruct the data back from the embedded representation to a representation that is as close to the original input as possible.

In the registration phase, MRI and TRUS manual surface meshes are extracted for the unseen patient data.The non-rigid registration between the test MRI and the TRUS meshes are regularized using the trained AE. A ResNet based automatic segmentation is applied in order to segment the prostate gland region on the target test TRUS Image. This method employs two types of residual blocks.

A ResNet based automatic segmentation is applied in order to segment the prostate gland region on the target test TRUS Image. This method employs two types of residual blocks.

3.4.1 Data Collection

The clinical dataset used in this work consists of 45 patients treated for prostate cancer with high dose rate (HDR) brachytherapy at the *Centre Hospitalier de l'Universite de Montreal* (CHUM). Data for each subject contains a diagnostic MRI volume and one intra-operative TRUS volume acquired before catheter placement.

For MRI scans, T2-weighted 3D variable-flip-angle TSE images with 1mm isotropic voxels were acquired on a 1.5T Siemens Magnetom, without an endorectal coil.

The 3D TRUS images have 0.5 mm slice thickness and obtained with the Oncentra Prostate (OcP) system using BK Flex Focus 400. Each volume consisted of 94 2D slices, which compounded the volume.

Prior to and during the clinical process, the boundaries of the prostate on all the MRI and TRUS volumes (respectively) are manually segmented by the radiation oncologist. In addition, a gold standard MRI-TRUS registration is available. An expert clinician manually selected the initial fiducial points in order to perform the B-Spline registration.

With regards to the automatic segmentation, the following pre-processing steps are applied to TRUS images : the TRUS images were resampled to have the same voxel spacing. Then, the images were normalized using standard deviation and min-max approach to bring them

into the same intensity range.

3.4.2 Evaluation metrics

Evaluation metrics for TRUS automatic segmentation

For validation of automatic segmentations, we consider the manual segmentation available on each sample data (performed by the radio-oncologist) as ground truth and estimate how close the automatic segmentation result is to the ground truth annotations. Dice coefficient (Dice, 1945) indicates the amount of volume overlap between the automatically segmented structures and the corresponding manually annotated ones. It is defined as :

$$Dice(A, B) = 2\left|\frac{A \bigcap B}{|A| + |B|}\right| \tag{3.1}$$

with A and N as the generated and ground-truth masks.

Evaluation metrics for MRI/TRUS surface based registration

To evaluate the accuracy of the proposed MRI/TRUS surface registration approaches, two metrics are used.

Mean squared distances (MSD) which represents the average squared difference between the deformed prostate surface from the MRI (i.e., the estimated value) and the target TRUS surface (i.e., the actual value). MSD is defined as follows :

$$MSD = \frac{1}{n}\sum_{i=1}^{n} x_i^2 \tag{3.2}$$

Where x_i^2 is the point-to-point error between deformed MRI and the target TRUS vertices.

Target registration errors (TRE) is another metric which computes the distance after registration between corresponding anatomical landmarks that have been chosen manually and is computed as :

$$TRE = \|S_{TRUS} - T(S_{MRI})\| \tag{3.3}$$

Where $T(.)$ is the final transformation computed by the proposed registration approach.

CHAPITRE 4 METHODOLOGY

In this chapter, the different methods used in the surface based MRI-TRUS registration approaches are presented. In both proposed registration approaches, an automatic segmentation based on Residual networks is used to segment TRUS images for unseen cases. In the proposed registration methods, prostate shape variation models are trained from clinical cases. Then, at test time, this variation model is incorporated in a non-rigid registration process to find the MRI-TRUS surface fusion for an unseen subject. These approaches could be used in improving biopsy planning and guided prostate cancer diagnoses.

In the following sections, first the automatic segmentation approach based on FC-ResNet is explained. Then, Section 4.2 presents the statistical deformable model based registration approach. Finally, Section 4.3 describes the proposed AE-based approach.

4.1 Automatic TRUS image segmentation

In this section, a 2D auto-segmentation algorithm (9) segments each 2D TRUS slice individually. An overview of the automatic segmentation approach is shown in Figure 4.1.

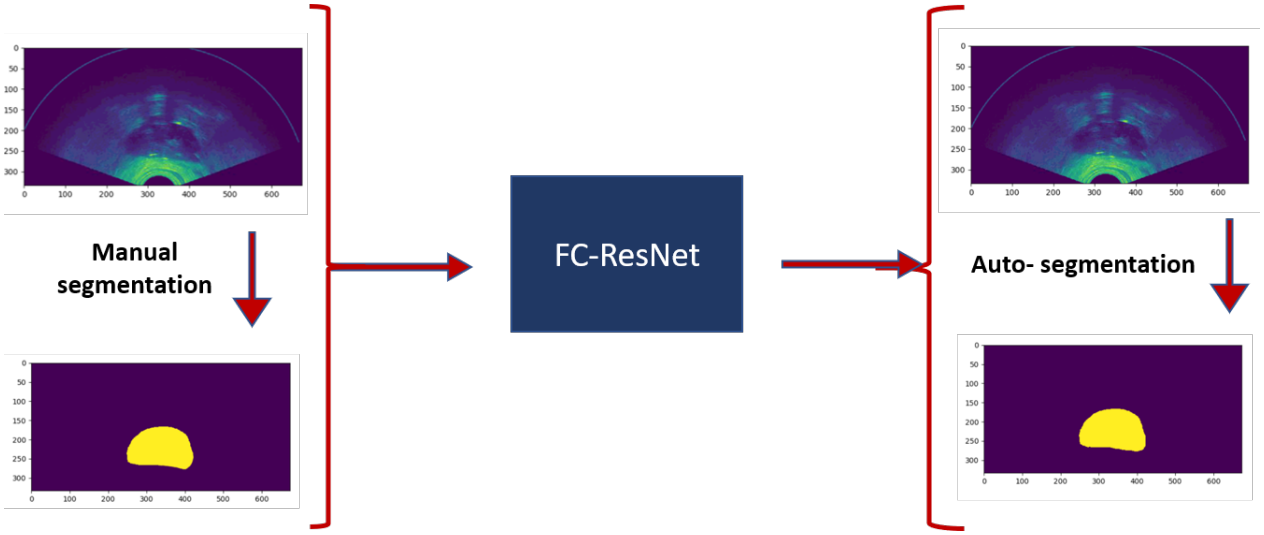

FIGURE 4.1 An overview of the FC-ResNet based segmentation approach.

4.1.1 Data pre-processing

The TRUS images have been re-sampled to have the same voxel spacing. Then, the images have been normalized using standard deviation and a min-max approach to map them in to the same intensity range. Furthermore, the images were cropped based on the minimal width and minimal height of the images. Finally, the dataset was augmented with some random horizontal and vertical flipping, sheering (max. 0.41), rotation (max. 10deg) and warping (GRYDS tool). These values were chosen empirically based on the observed prostate deformations and according to the experimental analysis.

4.1.2 FC-ResNet

A FC-ResNet model is a combination of U-Net (53) and ResNet (67), which is a convolutional de-convolution (up sample-down sample) depth network model with residual connections.

As mentioned before, given x_i as input, a typical block of a network is a stack of layers that directly fits a desired underlying mapping as $F(x_i)$ (See Figure 2.12 - left). A residual block lets these layers to fit a residual mapping (Figure 2.12 - right) where

$$F(X_{i+1}) = F(X_i) + X_i. \tag{4.1}$$

Here, the identity mappings are applied by shortcut connections that directly adds up to the output of the stacked layers (Eq. 4.1).

This work employs the ResNet network introduced in (9) in order to segment the TRUS images. Two stacks of residual blocks were considered where each residual block is a composition of two sections : a series of nonlinear transformations and an identity mapping section. The non-linearity section has a combination of one or two convolutional layers, ReLu activation function (Eq. (4.15), Figure 4.15) and Batch Normalization (BN).

At the end of the residual blocks, these sections are summed together. Figure 4.2 illustrates the architecture of the mentioned two residual blocks introduced by (9).

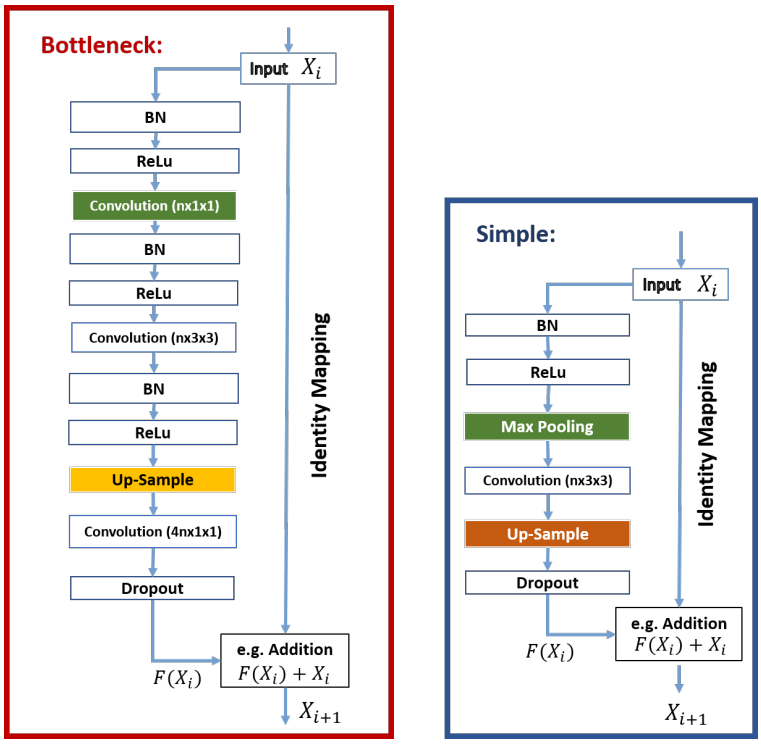

FIGURE 4.2 Two types of residual blocks. Left : Bottleneck Block. Right : Simple Block.

These blocks represent both up-sampling and down-sampling processes where the up and down sampling parts of each block is an optional feature that will be adjusted based on the position of the block in the ResU-Net's architecture.

The long skip connections shown in the Figure 4.3 represent two skip connections from the two convolutions in a simple block to it's corresponding simple block and one skip connection in the basic blocks.

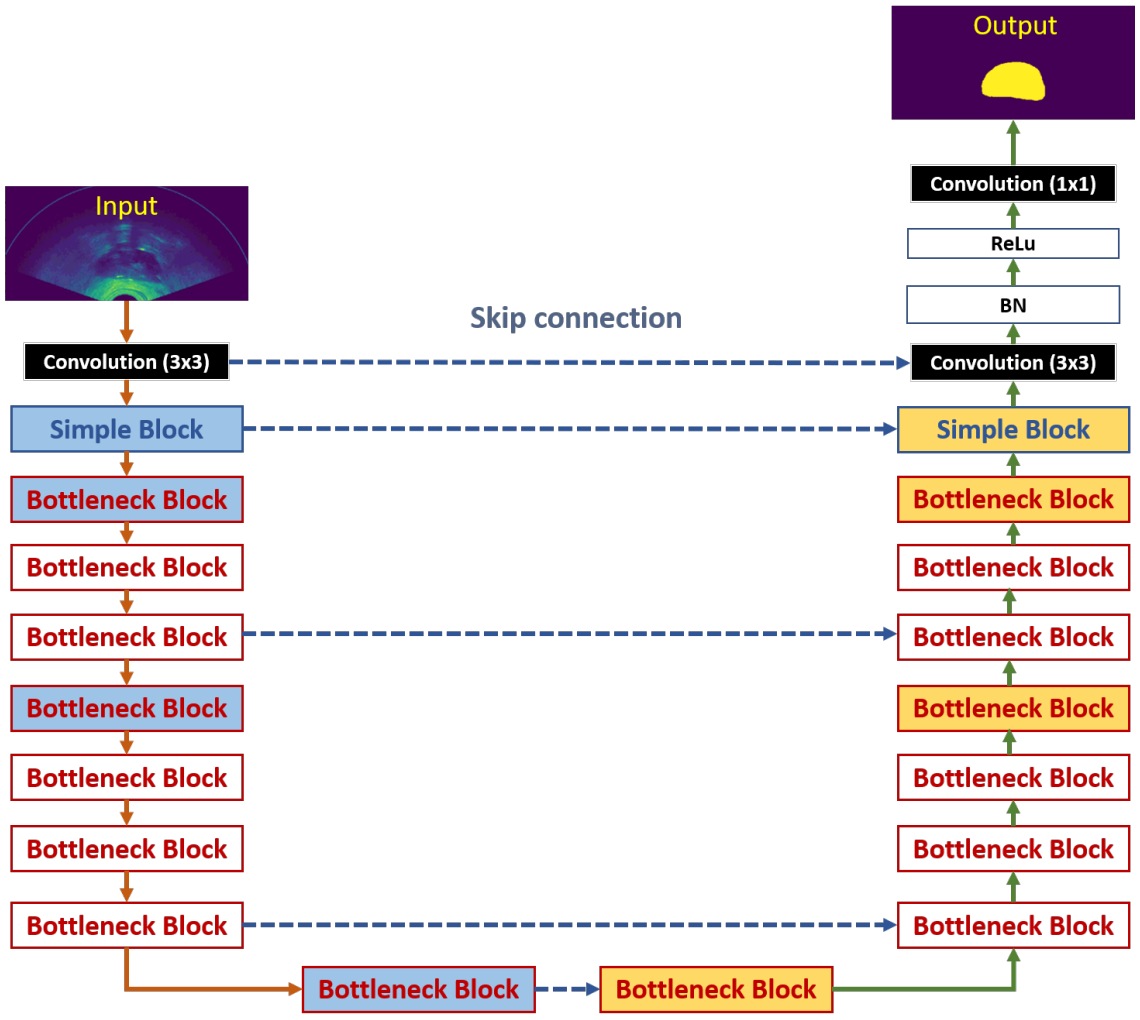

FIGURE 4.3 FC-ResNet structure. The orange boxes indicate the presence of down-sampling layers in the block and the blue boxes represent the up-sampling layers.

The Dice similarity (69) coefficient is used to measure the overlap between the automatically annotated surface and the manually segmented one used to optimize the network weights, Eq. (4.2) :

$$Dice(A, B) = 2 \left| \frac{A \bigcap B}{|A| + |B|} \right| \tag{4.2}$$

It is also sensitive to uncertainties in the segmentation labels.

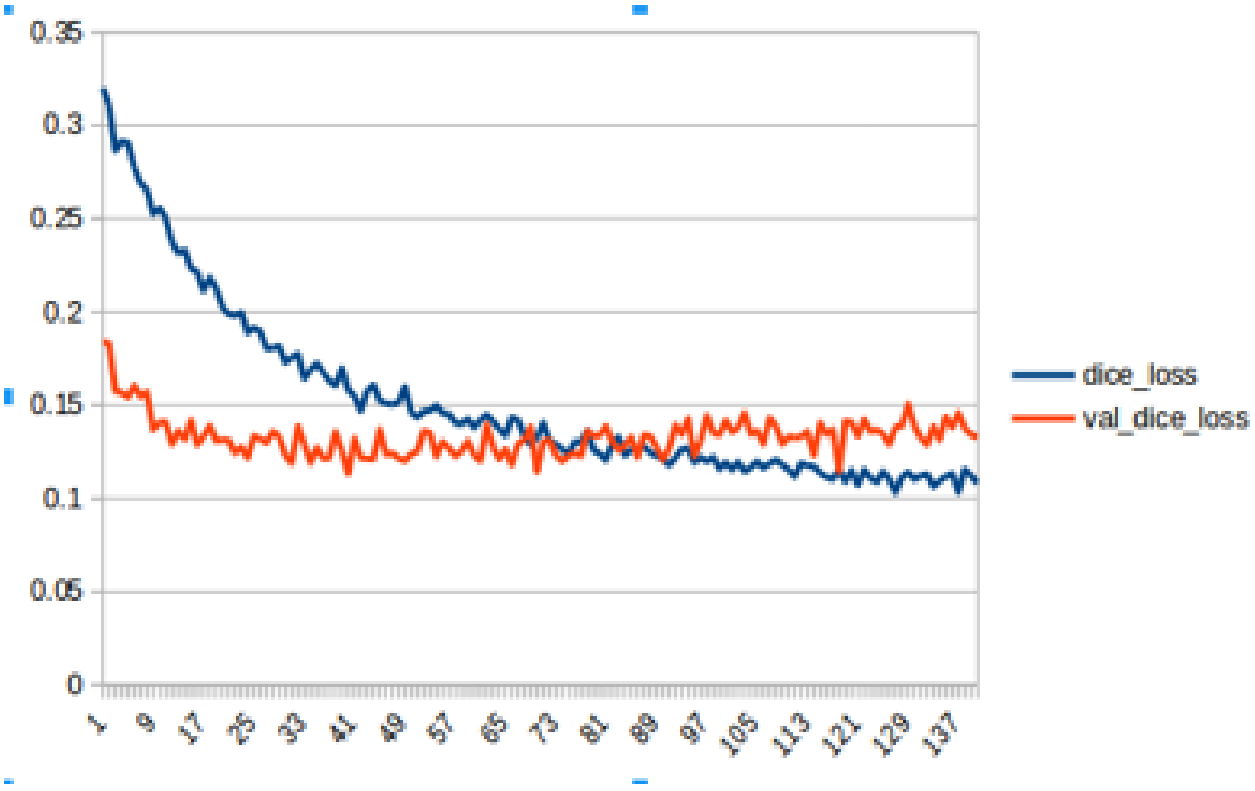

FIGURE 4.4 Evolution of Dice score loss function (for training and validation) with respect to of epochs.

4.1.3 Post-processing on the FC-ResNet output

As mentioned before, the FC-ResNet method is used to segment the intraoperative TRUS image. Then, in the next step, the triangular surface meshes were extracted from the segmented TRUS image.

Here, the main challenge for the TRUS images is that the segmentation method fails to segment some slices, creating void spaces in the prostate gland.

Figure 4.5-a shows a sample raw 3D mesh coming from the auto-segmentation. One could observe that the resulting mesh has some empty slices. The algorithm has failed to annotate the prostate gland in these areas.

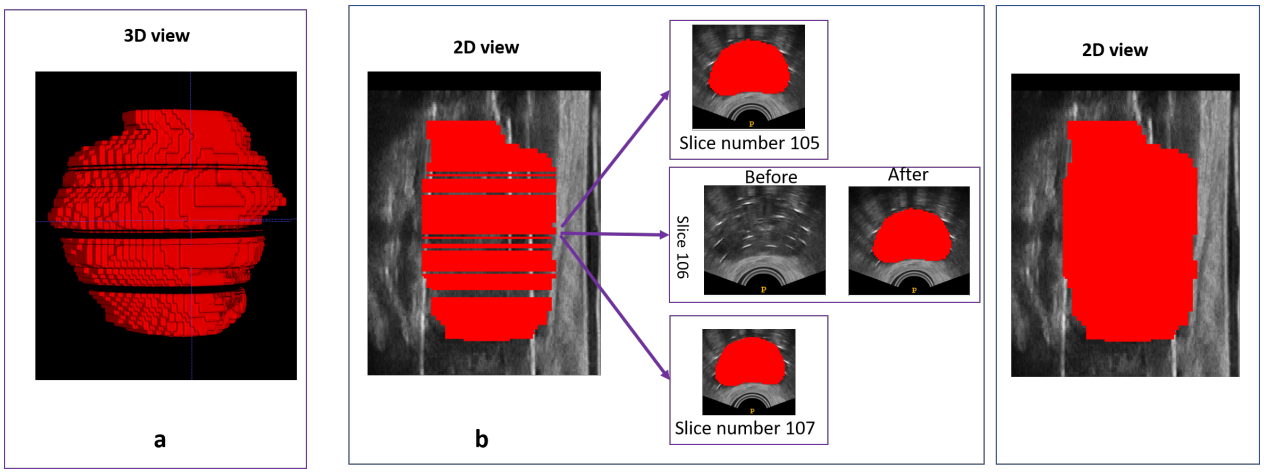

FIGURE 4.5 (a) The 3D reconstruction of a sample auto-segmented TRUS mesh. (b) The FC-ResNet algorithm failed to segment some layers (left block). To assess the registration method the unsegmented slices were filled using the mean masks of the neighbor slices (right).

In order to generate a monolith surface mesh, for each empty slice, the mean area of the adjacent layers is computed. Then the gap is filled with this mean surface. In other words, these mean surfaces are used as seed points to fill the gap and generate an integrated surface as shown in Figure 4.5.

4.2 Deformable MRI-TRUS surface registration using statistical deformation models

In this section, the non-rigid surface based MRI-TRUS registration method is described, which employs the surface motion models to increase the registration performance.

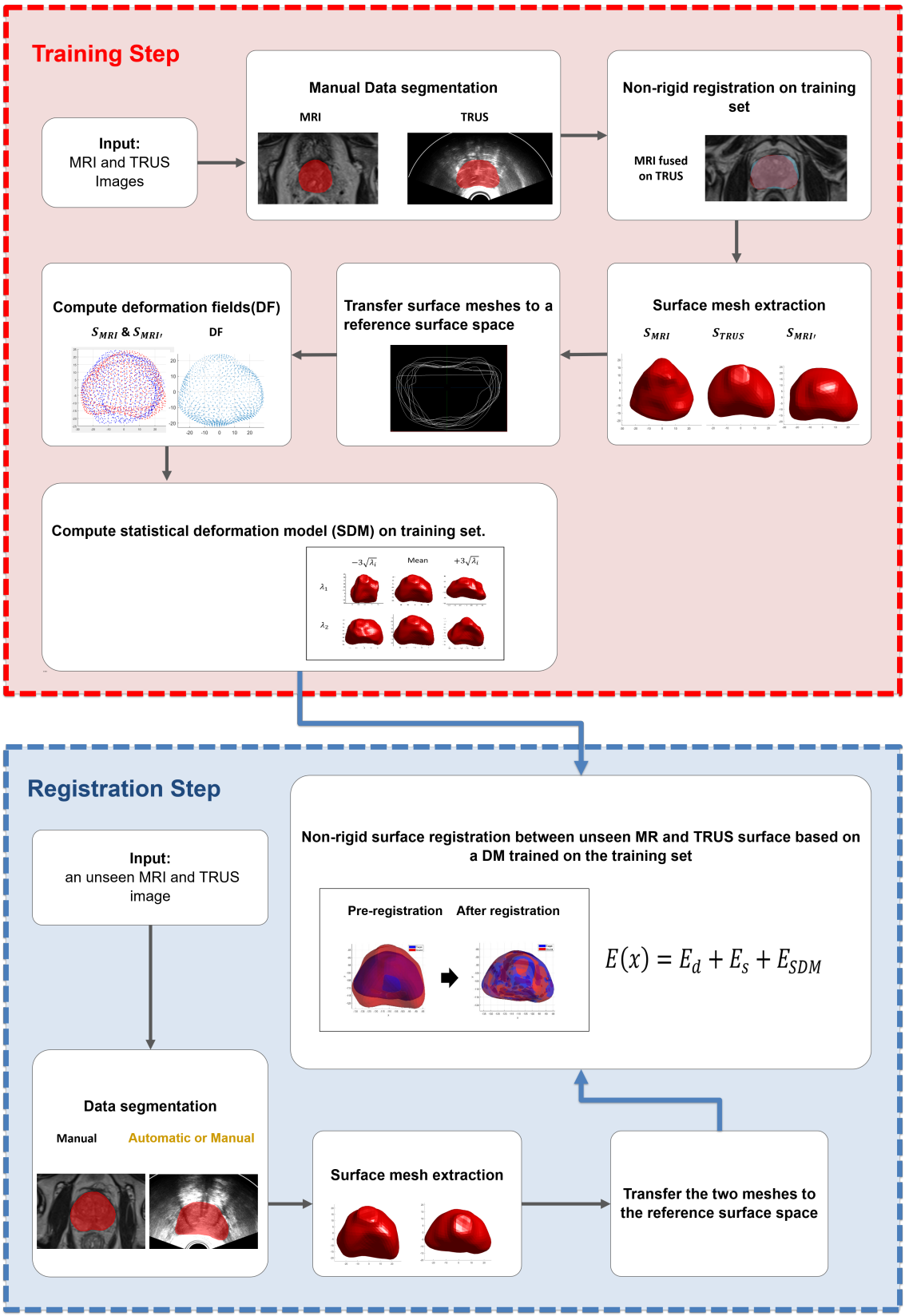

FIGURE 4.6 Diagram of the proposed MR-TRUS SDM registration method.

In general, the proposed method is performed in two main stages that each contain multiple steps. First an approach that generates a statistical deformation model (SDM) is performed. Here, using the training set, the deformation among MRI surface and its corresponding TRUS surface is captured. A registration phase follows this step. It fuses the MRI surface mesh to the TRUS surface mesh using the trained SDM prostate models as prior. The diagram on Figure 4.6 demonstrates the step by step procedure of the method.

4.2.1 Data pre-processing

The data used in this work consists of one pre-operative MRI and one intra-operative TRUS image from a set of n patients ($i = 1, 2, ..., n$) treated with brachytherapy. During the clinical workflow, the boundaries of the prostate on all the MRI and TRUS volumes are manually segmented by an expert. (Figure 4.7)

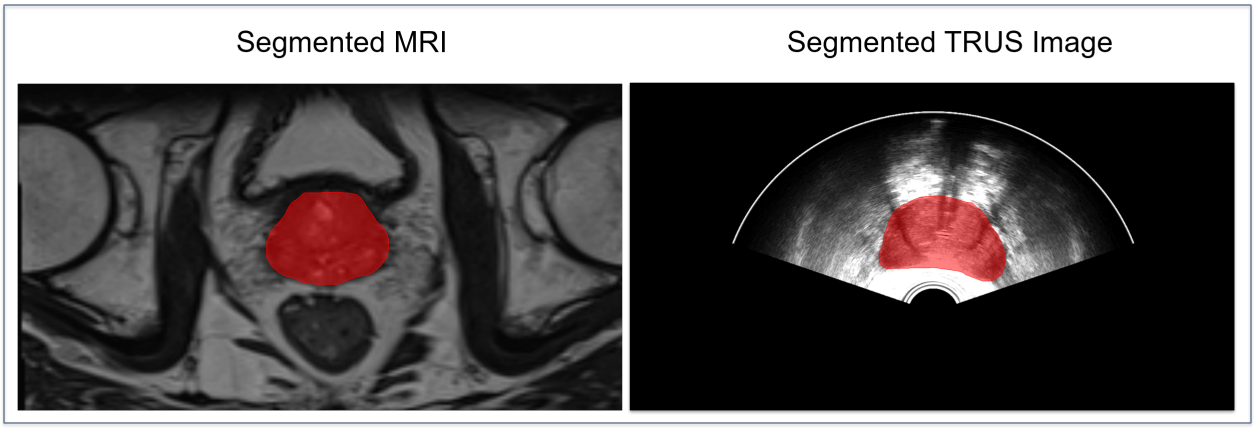

FIGURE 4.7 The prostate gland on a MRI (left) and a TRUS image (right) is specified by a radiation oncologist. It demonstrates the change in shape of the patient's prostate while it's under the pressure of the TRUS probe.

In order to train a SDM, the deformation fields from each MRI surface (S_{MRI}) to its corresponding TRUS surface mesh(S_{TRUS}) is required.

Thus, for each patient, the MRI surface ($i = 1, 2, ..., n$) is non-rigidly registered on its equivalent TRUS surface using 3D B-spline uniform grids (70) (71) :

$$(MRI_i' \cup Sg_{MRI'}) = (MRI_i \cup Sg_{MRI}) \bigotimes T((MRI_i \cup Sg_{MRI}) \rightarrow (TRUS_i \cup Sg_{TRUS})) \quad (4.3)$$

where, T is the FFD transformation model with B-spline parameterization. MRI_i , $TRUS_i$ and MRI_i' represent the original, target and deformed volumes. Also, Sg_{MRI}, Sg_{TRUS} and $Sg_{MRI'}$ are the segmented prostates on the corresponding image. Finally, $\bigotimes$ is the concatenation process that takes the volume and its surface to their target state.

At this point, each patient data contains three segmented images : one segmented preoperative MRI, one segmented TRUS image and a deformed MRI($MRI_{'}$). Then, a marching cube algorithm (72) extracts the triangular surface meshes of the segmented MRI (S_{MRI}), segmented TRUS (S_{TRUS}) and segmented deformed MRI ($S_{MRI'}$) by calculating triangle vertices employing linear interpolation. Practically, the deformed MRI surface mesh ($S_{MRI'}$) is defined as Eq. (4.4) :

$$S_{MRI'} = S_{MRI} \bigotimes T(S_{MRI} \rightarrow S_{TRUS}). \tag{4.4}$$

A linear transformation rigidly aligns all the surface meshes on a common reference space, as shown in Figure 4.8.

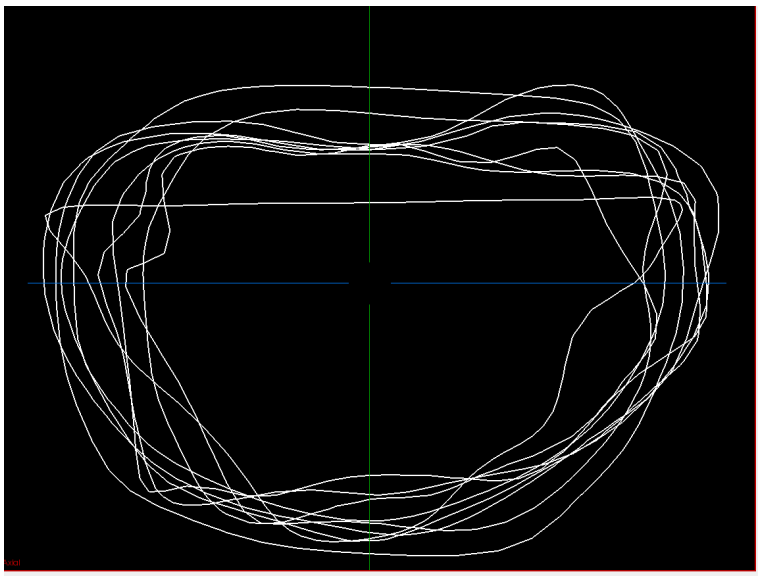

FIGURE 4.8 Surface meshes aligned in a reference space.

In order to uniformize the number of vertices constructing a surface mesh and establishing point-to-point correspondence across all the surface meshes, a spherical harmonics approach (SPHARM-PDM) is used (73). Here, each mesh is represented by spherical parameterization that maps the surface on a sphere. It establishes a monotonous subdivision across the surfaces

in order to equalize the number of points on all surfaces. Thus, all the surface meshes are composed of 1002 vertices. In this process a random surface from the training set is considered as an atlas (reference mesh). A rigid Procrustes analysis leads to one to one mapping among the vertices of the surface meshes. Figure 4.9 demonstrates the resulting point cloud for a sample patient mesh. For each patient $i = 1, 2, ..., , n$, three surface meshes are available : one MRI surface mesh ($S_{MRI,i}$), a TRUS surface mesh ($S_{TRUS,i}$) and deformed MRI surface ($S_{MRI',i}$). Equation 4.4 represents the computation of $S_{MRI',i}$ Where $S_{TRUS,i} \approx S_{MRI',i}$

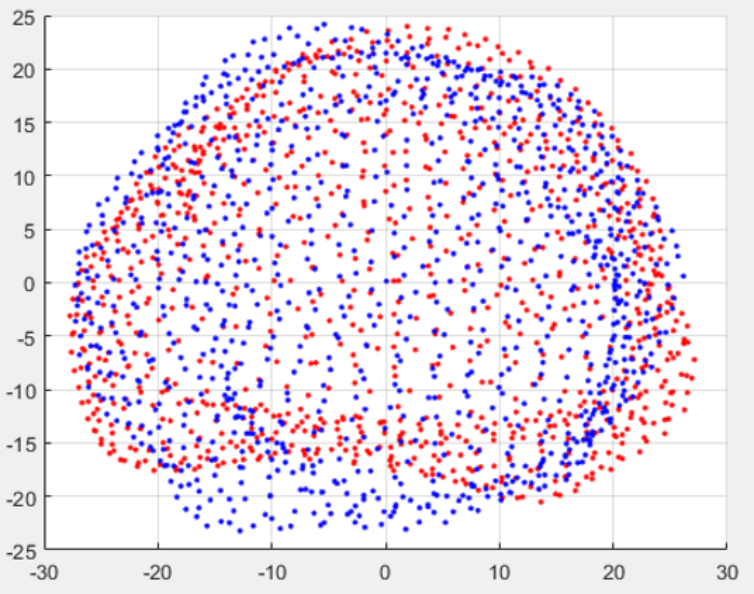

FIGURE 4.9 Point-to-point correspondences are established between the meshes. MRI surface points S_{MRI} (red) and it's equivalent deformed MRI surface points $S_{MRI'}$ (blue) of a patient on a common reference space. Each surface mesh is composed of 1002 3D vertices.

4.2.2 Training a non-rigid statistical deformation model

The distance between each MRI surface ($S_{MRI,i}$) to its deformed MRI surface ($S_{MRI',i}$) is computed to form a 3D translation matrix of displacement field, (Figure 4.10).

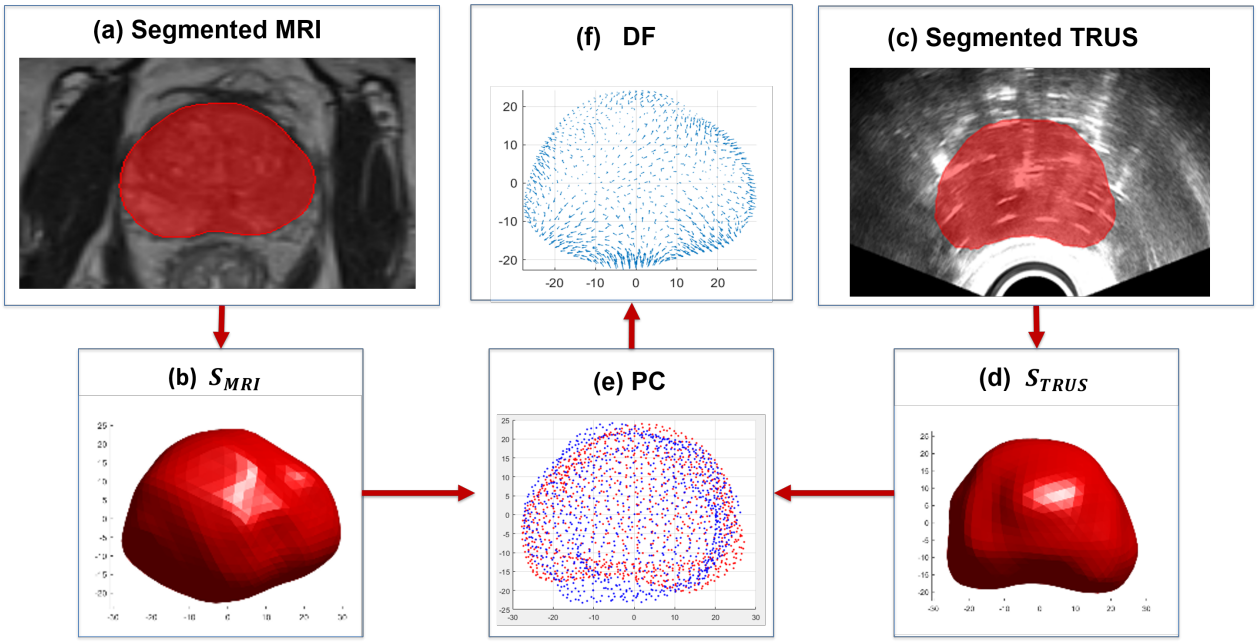

FIGURE 4.10 Diagram of deformation field extraction. For each sample patient data i, a segmented preoperative MRI (a) and its surface mesh of the prostate gland (b), segmented intra-operative TRUS image (c) along with its surface mesh (d) are present. This leads to the pre-processed MRI and TRUS surfaces in terms of discrete points (point cloud) (e). Then, t he non-rigid deformation field arrows between the two shapes (f) is represented.

Here, a statistical deformation model (SDM) of the prostate deformations is built. This is performed by performing Principal Component Analysis (PCA) on the training set of MRI-TRUS surface deformation fields (df). The mean displacement and the Eigen parameters of covariance matrices from PCA will then form a SDM to be used as prior for the non-rigid registration.

Generally, Eq. (4.5) is the PCA function that computes the sets of anatomical variations of the training set :

$$df = \bar{df} + \lambda w \tag{4.5}$$

where $\bar{df}$ is the mean deformation of all the displacement fields on the training set and is computed based on Eq. (4.6) :

$$\overline{df} = \frac{\sum_{i=1}^{n} df_i}{n}. \tag{4.6}$$

Here, n represents the number of samples, λ is the orthogonal eigen-vectors matrix calculated on equation 4.7 and w is a vector of model weights :

$$\lambda = \frac{\sum_{i=1}^{n}(df_i - \bar{df})}{n-1} \tag{4.7}$$

Figure 4.11 illustrates the deformation according to the first two (out of 20) eigen-modes. In order to optimally demonstrate the feature of the non-rigid deformations from the proposed SDM, the displacements were applied on a sample MRI surface ($S_{MRI,1}$ from the train data set).

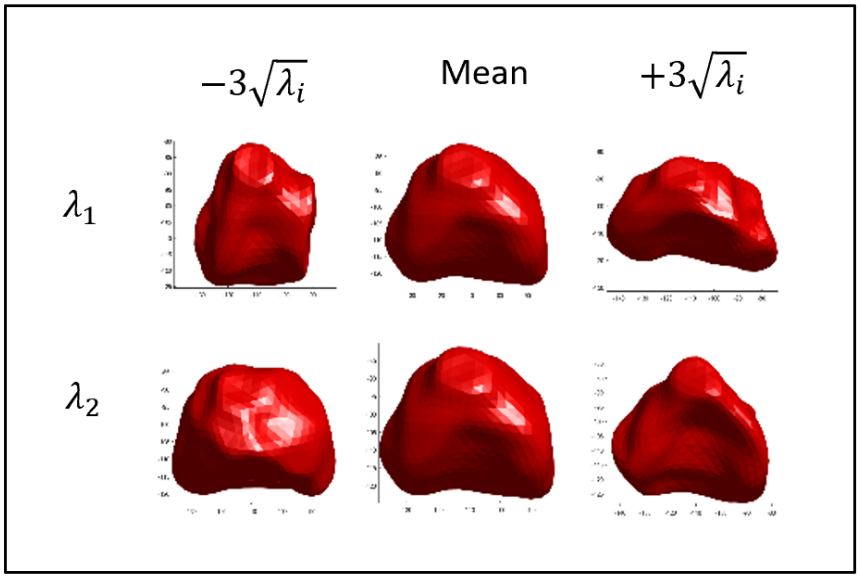

FIGURE 4.11 Visualization of the principle modes of variation of the MRI-TRUS surface deformation. The mean and primary modes of variation of the deformation fields are applied on the generated shapes. Each row shows a deformation according to the first and second eigen-vector, which capture deformations induced by insertion of the TRUS probe (8).

4.2.3 Surface-based statistical deformation model registration

In this section, the registration technique is presented to find the optimum deformation field in between unseen data surfaces. Just like in the previous section, each patient data consists of a manually segmented preoperative MRI image and a segmented intra-operative TRUS image. The surface meshes are extracted using the marching cube algorithm. The surfaces

are then rigidly registered to the SDM reference space.

Here, a non-rigid ICP based surface registration technique gradually warps S_{MRI} towards S_{TRUS} using the previously trained SDM as prior to the algorithm. The initial correspondence is estimated by spherical parameterization algorithm. The S_{MRI} is deformed towards S_{TRUS} using a series of stiffness coefficients. For each corresponding vertices (from S_{MRI} to S_{TRUS}), an affine transformation locally constrains the registration in order to minimise the local distance to the adjacent node.

Three factors affect the method and forms the final cost function : 1) the distance cost function E_d, 2) a stiffness term, and 3) a SDM regularizer :

$$E(x) = E_d + E_s + E_{SDM}. \tag{4.8}$$

Here, E_d is a sum of squared distance (SSD) between the source (S_{MRI}) and the target (S_{TRUS}) template, as shown in Eq. (4.9) :

$$E_d(X) := \sum_{v_i \sim v} dist^2(T, X_i v_i), \tag{4.9}$$

where $X = \{x_1, x_2, x_3, ...x_n\}$ is a 3x4 affine transformation matrices for each vertex. Furthermore, $v_i = [x, y, z, 1]^T$ is the template vertices and $dist(T, v)$ represents the distance between vertex v and the nearest vertex on S_{TRUS}.

The stiffness term (E_s) constrains the function according to the weighted distance of adjacent vertices (X_i and X_j are the adjacent points) as in Eq. (4.10). Also, $G = diag(1, 1, 1, \gamma)$ is the weight variable. The stiffness term is also penalized under the Frobenius norm :

$$E_s(X) := \sum_{i,j \sim \varepsilon} \|(X_i - X_j)G\|_2^F \tag{4.10}$$

An additional SDM term regularizes the deformation. The weighted difference of the transformations of neighbouring vertices are penalized under the Frobenius norm matrix weighted by the deformation matrix of the corresponding vertice on the SDM df_v :

$$E_{SDM}(X) := \sum_{i,j \sim \varepsilon} \|(X_i - X_j)df_v\|_2^F \tag{4.11}$$

For evaluating the proposed registration method, accuracy is quantified as both target registration error (TRE) (74) and mean squared deviation (MSD) (75).

$$MSD = \frac{1}{n}\sum_{i=1}^{n} x_i^2 \tag{4.12}$$

$$TRE = \|S_{TRUS} - T(S_{MRI})\| \tag{4.13}$$

where $T(.)$ is the transformation from the proposed registration approach and x_i^2 represents the point-to-point distance between fused MRI vertices and the TRUS vertices.

4.3 Deformable MRI-TRUS surface registration from deep auto-encoder deformation models

The previous statistical deformation model describes the linear relationships among samples in the training set. However, the non-linearity aspect of the data could effect the accuracy of the registration process. An auto encoder model (AEM) with non-linear activation functions, considers the non-linear relationship of the data alongside its linear factors. This is due to the inherent trait of the generative neural networks.

In this section, we show how to incorporate an AEM into the non-rigid ICP framework. First an AEM is trained on observation data of MRI-TRUS surfaces. Then, at test time, the AEM is incorporated in a non-rigid registration process to find the MRI-TRUS registration for an unseen subject. In the AEM based approach, the deformation between MRI and TRUS is constrained in a way that the TRUS surface fits to the trained sets of deformations.

The diagram in Figure 4.12 illustrates how the AEM-registration is performed. It indicates how the proposed AEM surface registration method is performed in two phases : a training phase (Section 4.3.1) and a registration phase (Section 4.3.2) using the AEM as prior.

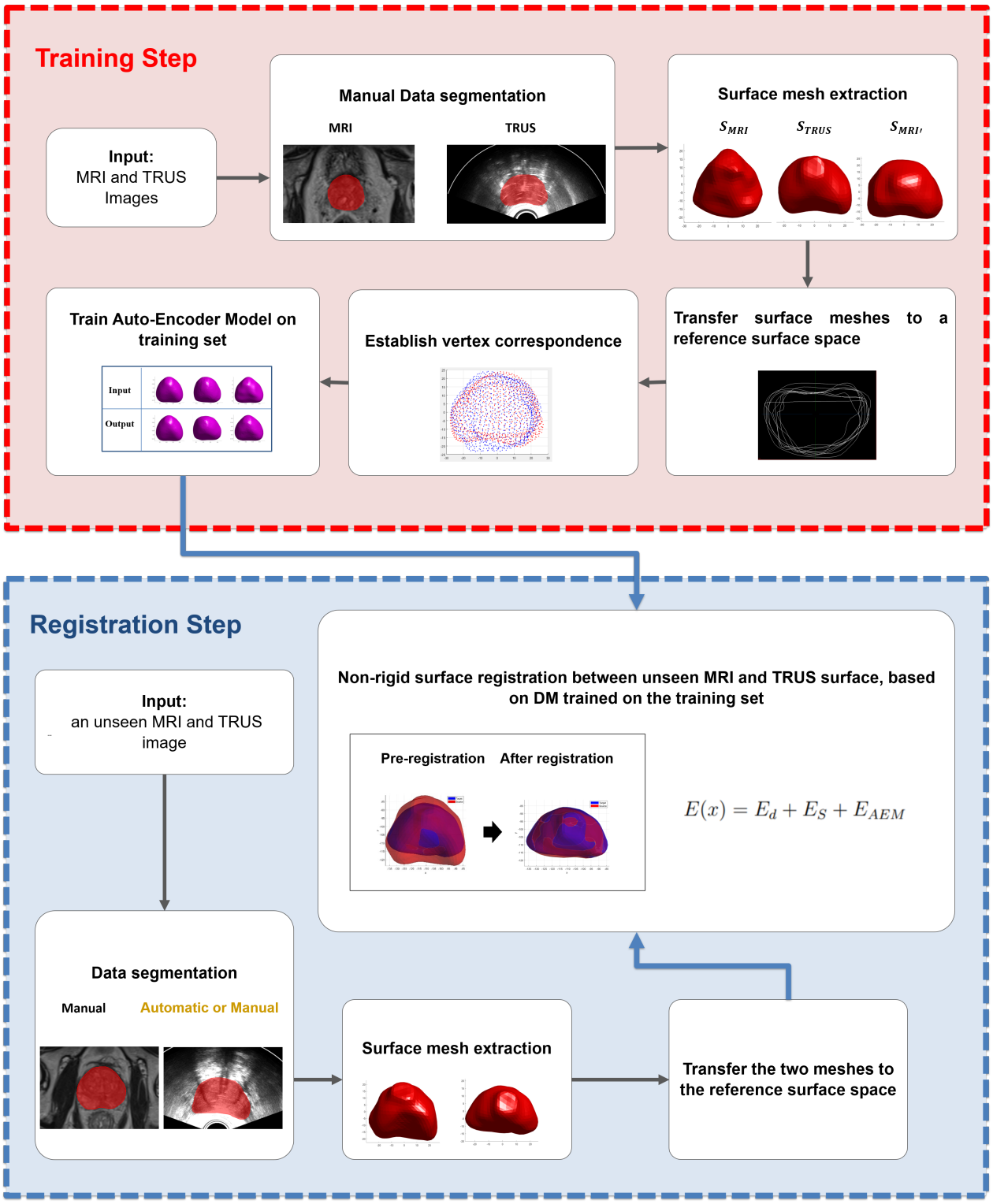

FIGURE 4.12 Schematic diagram of the proposed AEM registration framework.

4.3.1 Training phase of the AE model

In this section, modeling of the TRUS surface meshes is done as a latent representation. In fact, a shape manifold is created representing the 3D surfaces using few parameters, from the high dimensional parameter space (76).

Data pre-processing

For each intra-operative (TRUS) patient image, prostate boundaries were manually segmented by an expert as shown in Figure 4.13.

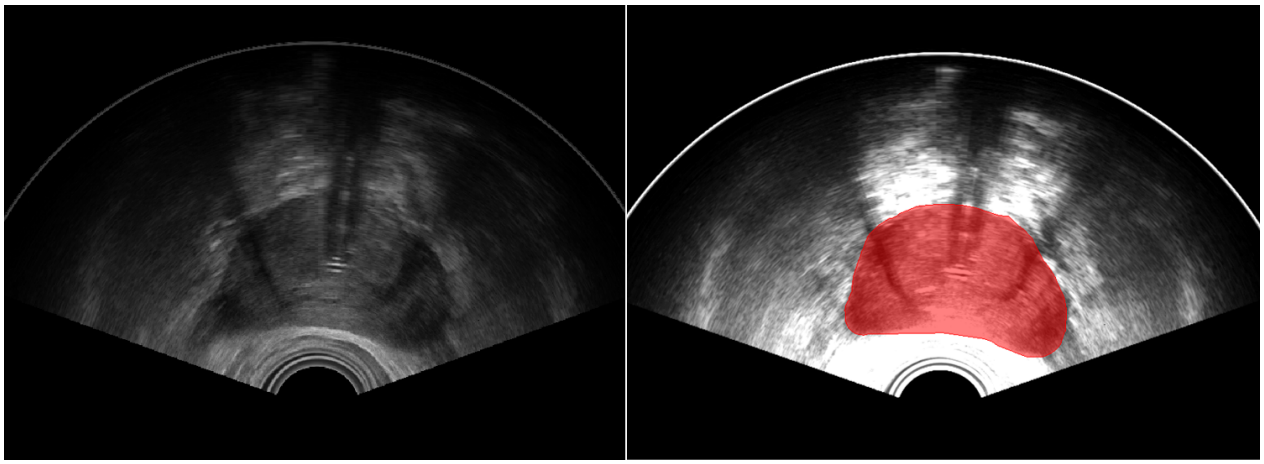

FIGURE 4.13 Left : an original TRUS image. Right : manually segmented TRUS image.

Here, the prostate triangular surface meshes of manually segmented MR and TRUS images are extracted using the Marching cube algorithm. Then, an initial rigid registration is performed to transform meshes to a common reference space (the reference can be a randomly selected meshes from the dataset). In the next step, a uniform subdivision of spherical parameterization of all surfaces is done to produce meshes with 1002 vertices. Then, the surface meshes are spatially aligned using the rigid Procrustes analysis to create a one-to-one mapping between vertices of all surface meshes. As a result, an initial point to point correspondence is established amongst all surface meshes.

Training a non-rigid AEM

A non-rigid AEM is trained on the TRUS meshes to non-linearly map each reduced 3D mesh parameters to its reconstructed version.

Figure 4.14 represents the auto encoder network that has been designed in the proposed approach. The detailed information about the dense layers in both encoder and decoder layers are presented. Generally, the auto encoder encodes the input into a smaller representation on several hidden layers, then decodes it to a degree of a quality.

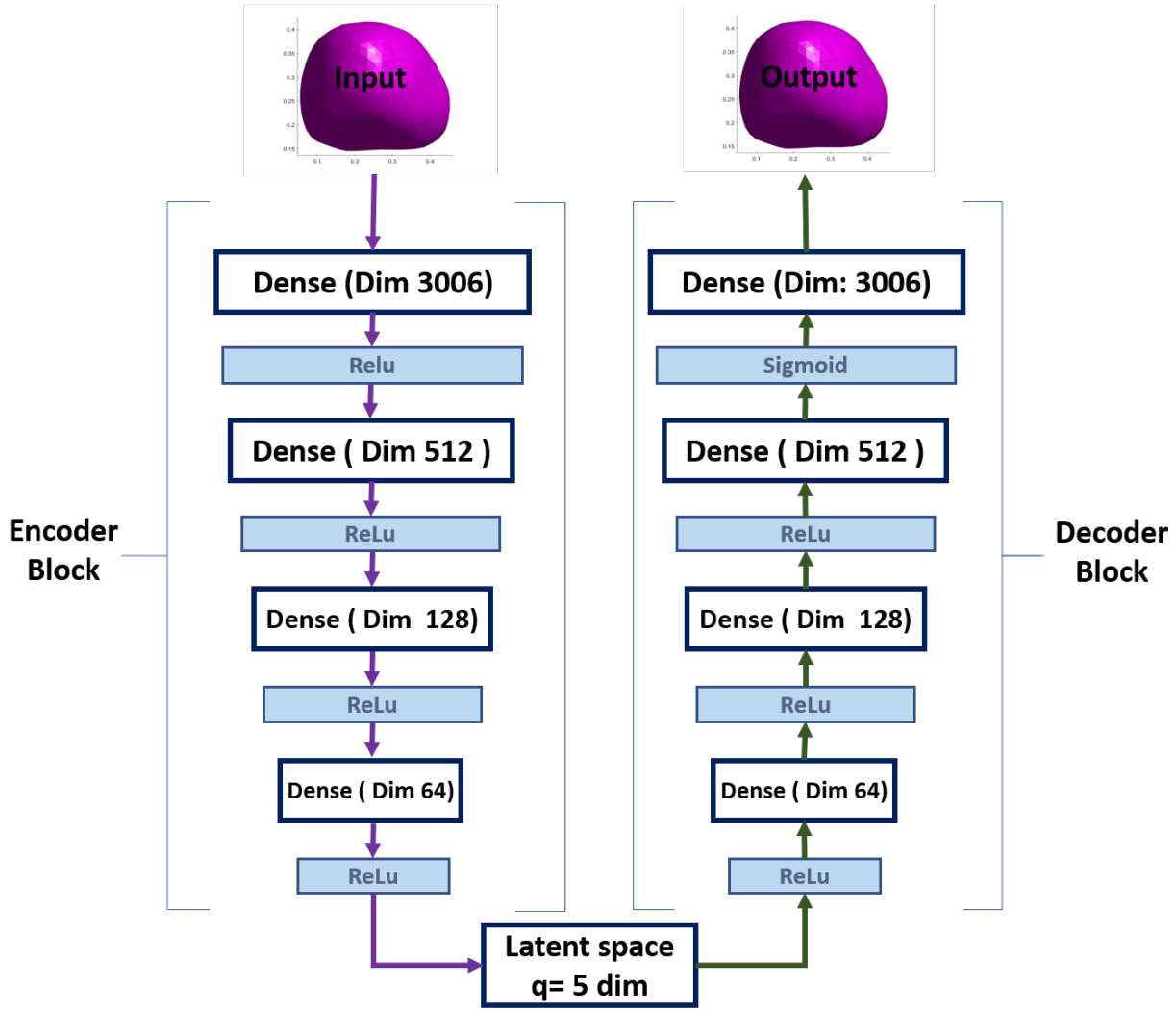

FIGURE 4.14 Configuration of the designed auto encoder network.

The designed feed-forward generative network is made of four fully connected layers. The layers have ReLu (Eq. (4.15), Figure 4.15) and Sigmoid (Eq. (4.16), Figure 4.16) activation functions in order to express non-linearity. The latent space q has the dimensionality of 5. The network is trained in a way that for all training meshes the input and output are as similar as possible. Thus, given the input S, the $encoder(.)$ brings S to the latent representation of q. The $decoder(.)$ maps q in to the output $S^{'}$, while minimizing the distance between S and

S' :

$$encoder(S) = q, decoder(q) = S'. \tag{4.14}$$

Here, the sum of squared distances is used as the similarity measure. In order to address the over-fitting issue, a dropout layer is used in all network layers with the probability of 20 percent.

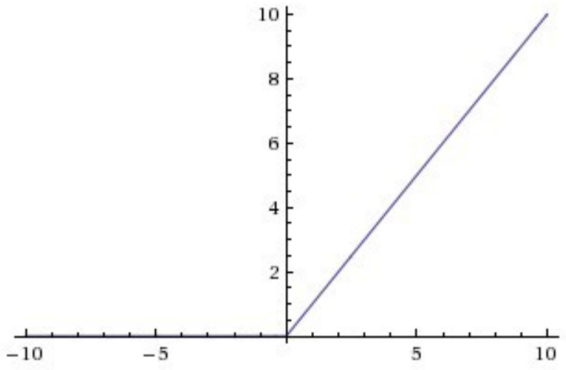

FIGURE 4.15 Rectified Linear Unit acts in a linear manner for all positive values, and neutralizes all negative values by setting them to zero. [www.medium.com]

$$y = max(0, x) \tag{4.15}$$

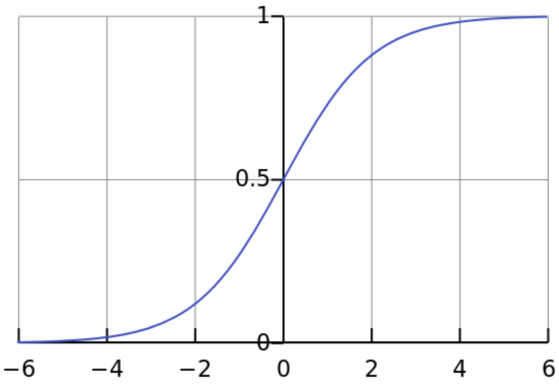

FIGURE 4.16 Sigmoid activation function (logistic function) it transforms the input value to an amount between zero and one. [www.medium.com]

$$y = 1/(1 + e^{-x}) \tag{4.16}$$

According to Figure 4.18, this AEM converged with a final mean square error of $1.02e^{-05}$. Figure 4.17 visualises some sample test subjects reconstructed using the proposed auto encoder.

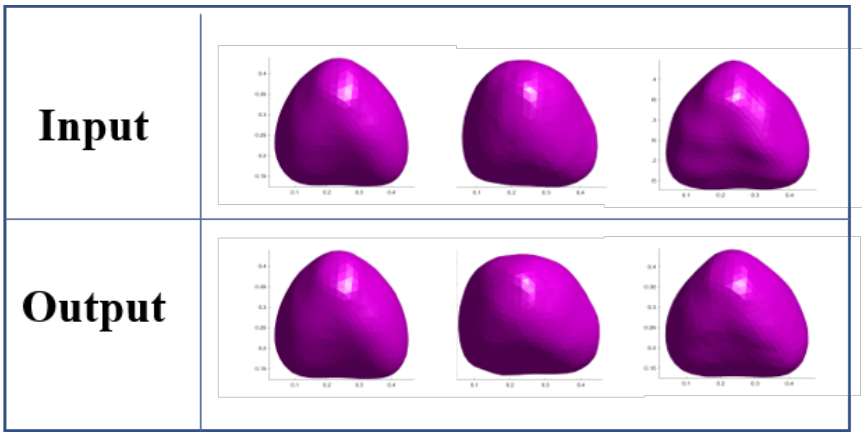

FIGURE 4.17 Reconstruction of some sample prostate surfaces by proposed Auto-Encoder.

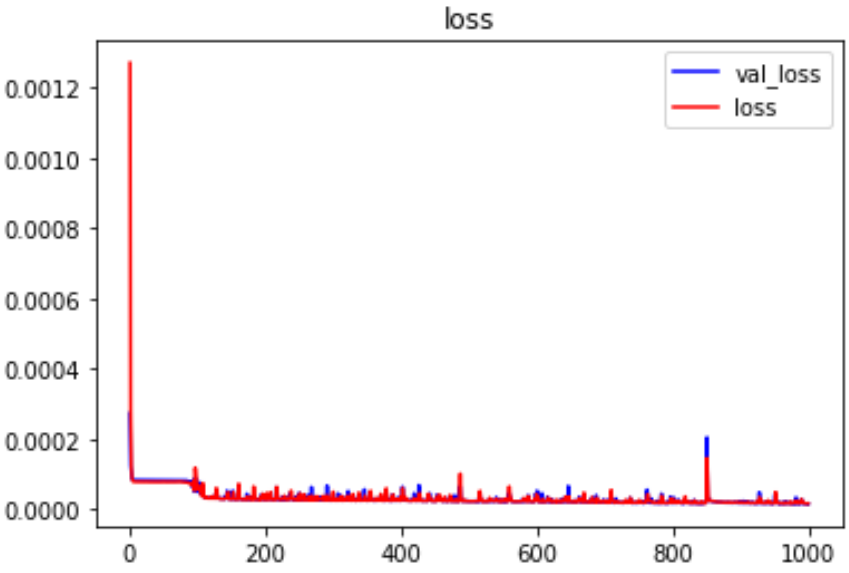

FIGURE 4.18 Convergence of sum of square distances of the presented Auto-encoder network.

4.3.2 Surface-based registration with deep auto-encoder model

Here, the objective is to register a preoperative MR image to an unseen TRUS image. First, the prostate boundary is extracted on both pre-operative MRI and intraoperative TRUS.

Then, the triangular surface meshes for both MRI and TRUS Masks are extracted using the Marching cube algorithm. The obtained surface meshes are then rigidly registered to the reference surface.

The proposed method non-rigidly registers the MRI surface to the TRUS surface by constraining the non-rigid surface registration algorithm to deform the surface according to the AEM modes of variation.

The proposed fusion approach between the MRI surface and the TRUS surface is computed by minimizing the following cost function :

$$E(x) = E_d + E_S + E_{AEM} \tag{4.17}$$

where E_d is a sum of squared distances between the source (MRI surface) and the target (TRUS surface) vertices, E_S is the stiffness term that penalizes the weighted differences related to the transformations of neighbouring vertices. The third term of the cost function is E_{AEM} that constrains the deformation to warp the surface in a way that fits in the AEM. Below each term is explained in more detail.

The distance cost function defines the deformation template on Eq. (4.18) :

$$E_d(X) := \sum_{v_i \sim v} w_i dist^2(T, X_i v_i) \tag{4.18}$$

where $X = \{x_1, x_2, x_3, ...x_n\}$ as the affine transformation matrices of size 3 by 4 for each vertices and the template vertices are defined as $v_i = [x, y, z, 1]^T$, $dist(T, v)$ denoting the surface for an unknown corresponding point node the w_i is set to zero.

A stiffness contributor regularizes the distance function. The differences of the transformation is weighted by $G = diag(1, 1, 1, \gamma)$ and is penalized under Frobenius norm Eq. (4.11). The weighted difference of the transformations of neighbouring vertices are penalized under the Frobenius norm :

$$E_s(X) := \sum_{i,j\sim\varepsilon} \|(X_i - X_j)G\|_2^F . \tag{4.19}$$

As mentioned in the previous section, the AEM is trained to reduce the dimension of a TRUS mesh in to the latent space q and reconstruct an output surface with minimum difference from the input mesh.

During the each registration iteration, one candidate deformation is computed that can be used to produce an intermediate TRUS surface S. This intermediate TRUS surface is fed to the encoder to produce the resulting q (i.e. $encoder(S) = q$). Here, the parameter q can be optimized such that the $decoder(q)$ is close to S (Eq. 4.20) :

$$E_{AEM} = \|decoder(q)_i - S_i\|_2 \tag{4.20}$$

where, i refers to the vertex index. As suggested in (76), in order to minimize the above equation, each element of q is projected between zero and one. This constraint on q works as a regularizer on each candidate deformation in our iterative registration process.

CHAPITRE 5 EXPERIMENTAL RESULTS

5.1 Evaluation of FC-ResNet automatic segmentation

In the first experiment, the accuracy of the FC-ResNet segmentation approach is evaluated. In order to assess the performance of the proposed method on segmented 2D TRUS slices, a five-fold cross-validation strategy was used. The division of the data on each cross-validation is set at 20% for the test set, 30% for the validation set, and 50% for the training subjects.

The Adam optimizer was used for an adaptive learning rate in order to train the network. The learning rate hyperparameter was initially set at $1e^{-8}$, which controls how much to change the model in response to the estimated error each time the model weights are updated. Here, the performance of the method is evaluated using the Dice score. It evaluates the volume overlap between an auto-segmentation result and ground truth segmentations. The Dice score is one of the common evaluation methods used in the literature to assess segmentation accuracy.

Here, the prostate surface is divided into three sub-regions : base, mid-gland, and apex (Figure 5.1). The validation metrics are reported for each sub-region, with results presented in Figure 5.2.

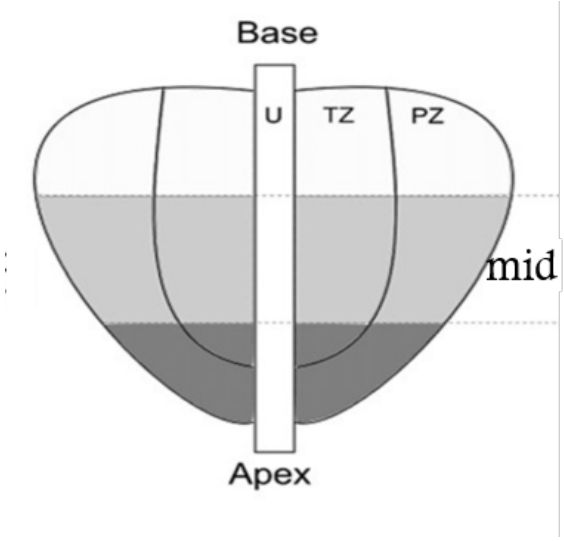

FIGURE 5.1 The prostate segmentation accuracy was assessed based on the 3 subsections : base, mid-gland and apex. [https ://pharmaceuticalintelligence.com/]

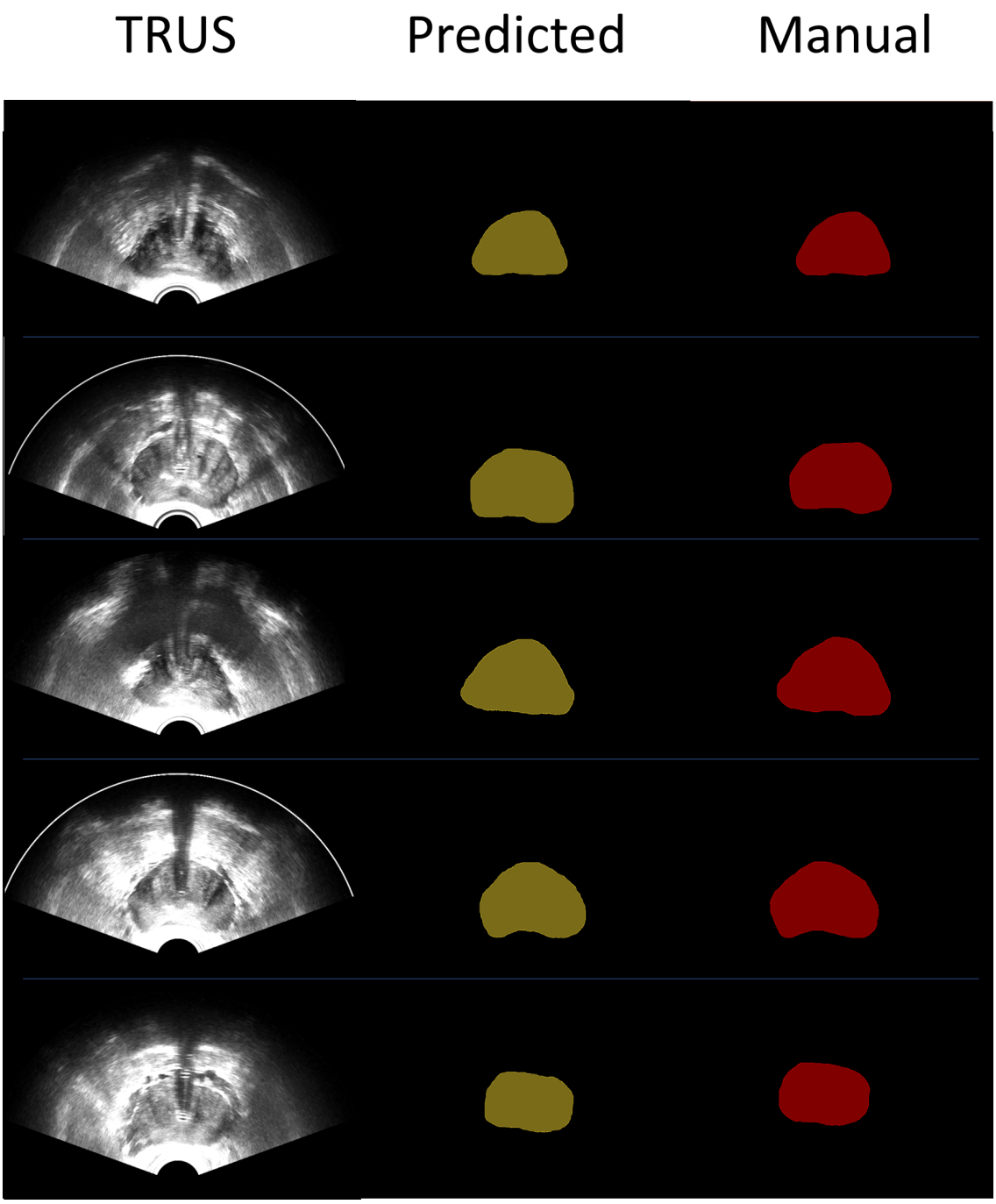

FIGURE 5.2 Samples of acceptable segmentation results from the FC-ResNet.

By exploring the segmentation results in more depth, we can observe that the proposed segmentation has some limitations. For instance, as it is shown in Figure 5.3, the FC-ResNet approach fails to segment or performs poorly on some slices. Figure 5.4 shows the effect of these missed slices on the segmentation of the whole gland.

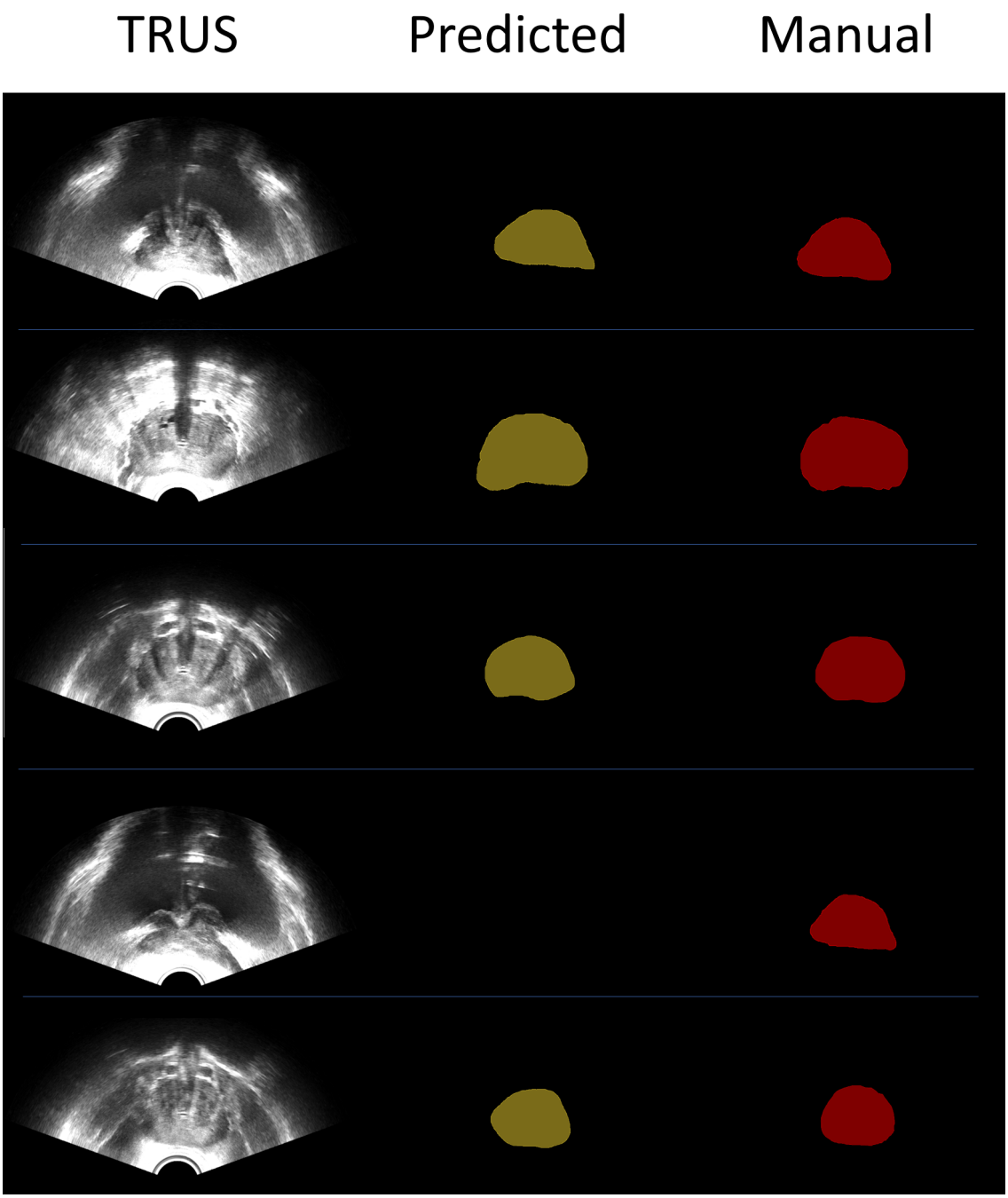

FIGURE 5.3 Samples of failed and inaccurate segmentation results of the prostate gland.

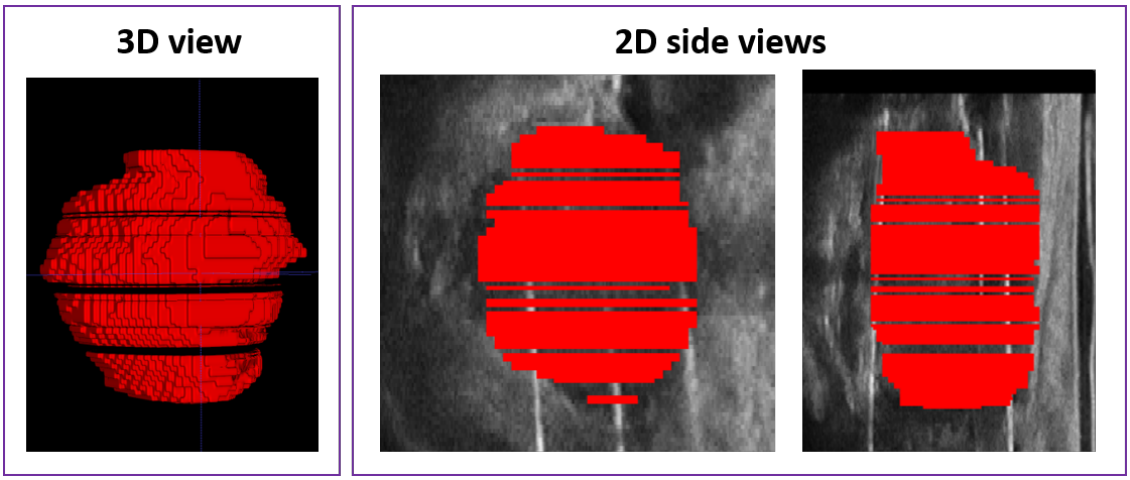

FIGURE 5.4 Failed segmentation results resulting in gaps in the segmentation of the whole 3D gland. Both 3D and 2D views are displayed.

In order to evaluate the accuracy of the FC-ResNet approach, the Dice score is computed from the automatic segmentation and the ground truth segmentation. Table 5.1 shows the Dice scores for each region.

TABLE 5.1 The Dice score computed between the FC-ResNet segmentation and the ground truth segmentation. The Dice measures are reported for each region (Apex, Mid, and Base) separately.

	Dice			
	Apex	Mid	Base	Overall
FC-ResNet	72.2	89.3	84.9	82.13

5.2 Evaluation of MRI-TRUS fusion approaches

In this work, two different MRI-TRUS fusion approaches are proposed. The SDM based registration approach (SDM-NICP), first extracts the MRI-TRUS deformation fields from a training set. Then, it trains a statistical deformation model on the set of deformations. In the registration phase, the unseen MRI surface is registered to it corresponding manually segmented TRUS surface using a NICP based registration. This proposed registration approach integrates the SDM as a regularizer to increase fusion accuracy. Table 5.2 reports target registration errors (TRE), mean squared distance (MSD), and Dice score for the proposed SDM-NICP approach.

The AEM based registration approach (AEM-NICP) first trains a deep neural network on

a training set of 3D TRUS surfaces. This trained Auto Encoder (AE) can encode an input surface into a latent space and then decode the latent representation to the output. The AE is trained in a way that for all training surfaces the input and output are as similar as possible. In the registration phase, a MRI-TRUS NICP registration approach is applied, in which the inferred TRUS surface is constrained to fit in the AE model trained in pairs of MRI-TRUS deformations. Table 5.2 shows the target registration errors (TRE), mean squared distance (MSD), and Dice score for the proposed AEM-NICP approach.

TABLE 5.2 Comparison of the proposed SDM-NICP and AEM-NICP approaches, where manual segmentation of the unseen TRUS image is used. Evaluation is based on target registration errors (TRE), mean squared distance (MSD), and Dice score. The results are reported in each sub-region separately.

	SDM-NICP w/ man TRUS seg.			AEM-NICP w/ man TRUS seg.		
	Apex	Mid	Base	Apex	Mid	Base
MSD (mm)	0.68 ±0.26	0.29 ±0.17	0.24 ±0.18	2.49 ±0.16	0.32 ±0.27	0.24 ±0.16
TRE (mm)	6.33 ±1.89	5.14 ±1.72	4.08 ±1.49	6.52 ±1.79	5.58 ±1.49	4.08 ±1.43
Dice	86.2	85.4	88.9	84.6	85.9	88.7

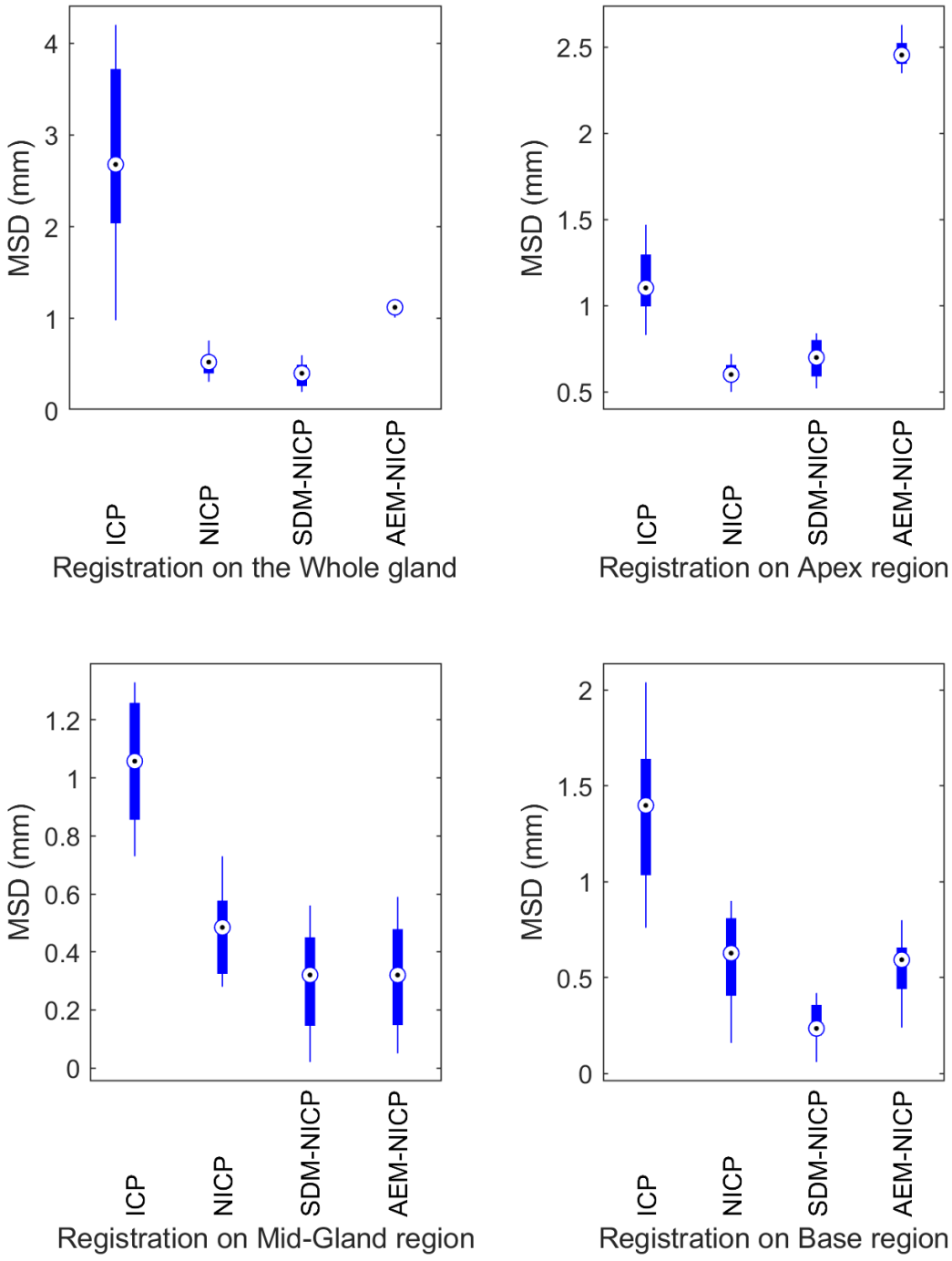

FIGURE 5.5 Comparison between the proposed registration approaches (SDM-based and AEM-based registration) and baseline methods (ICP and NICP). Mean squared distance (MSD) metric is computed on whole prostate gland and on each individual sub-region, separately.

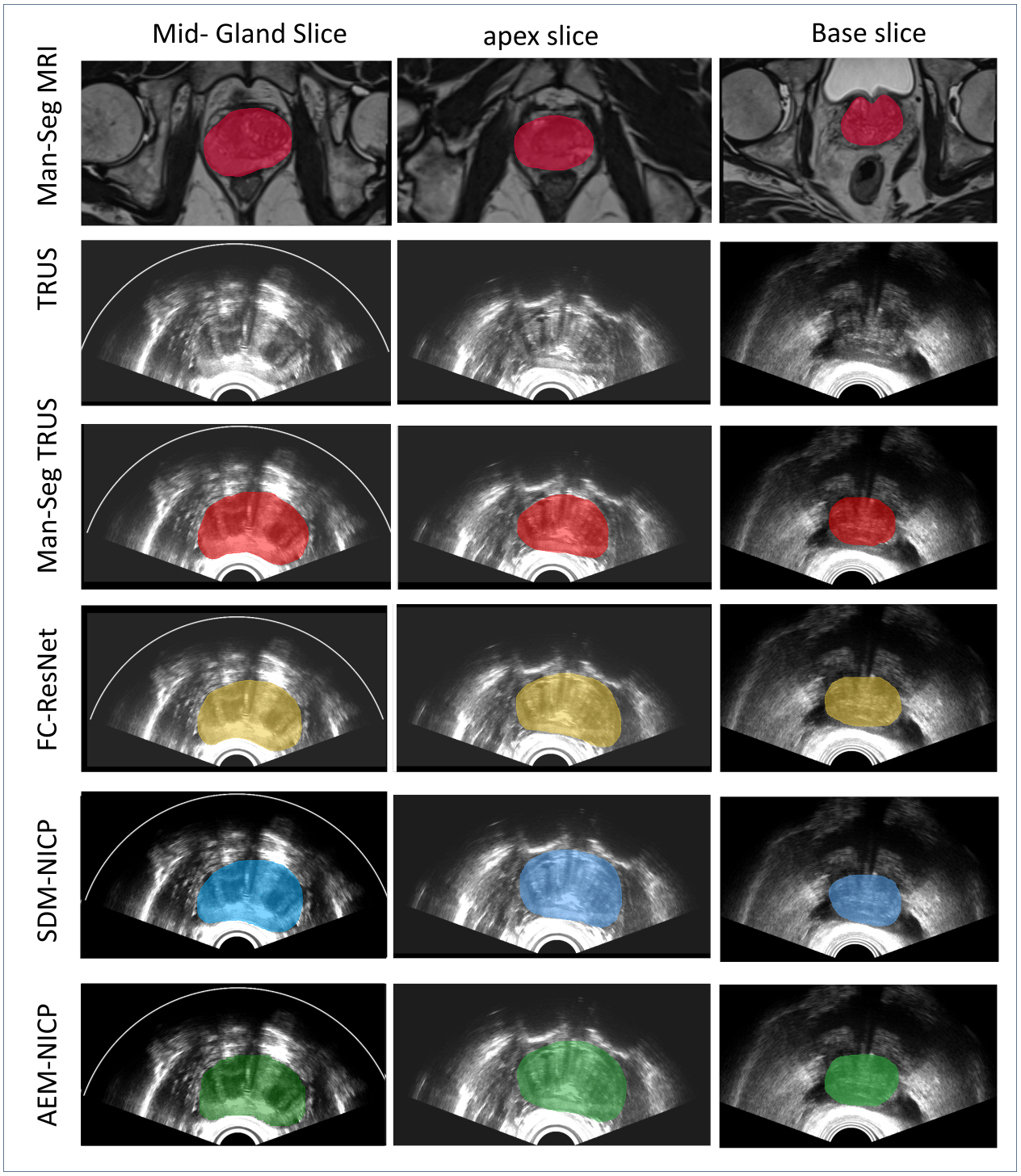

FIGURE 5.6 Segmented TRUS image for patient one in three sub-regions. Man-Seg MRI : original MRI with manually segmented prostate overlaid. TRUS : original TRUS image. Man-Seg TRUS : Manual segmentation shown on top of the TRUS image (Ground truth). FC-ResNet : Automatically segmented TRUS image. SDM-NICP : MRI surface fused to FC-ResNet surface by applying the SDM-NICP approach. AEM-NICP : MRI surface fused to FC-ResNet surface using the AEM-NICP proposed method.

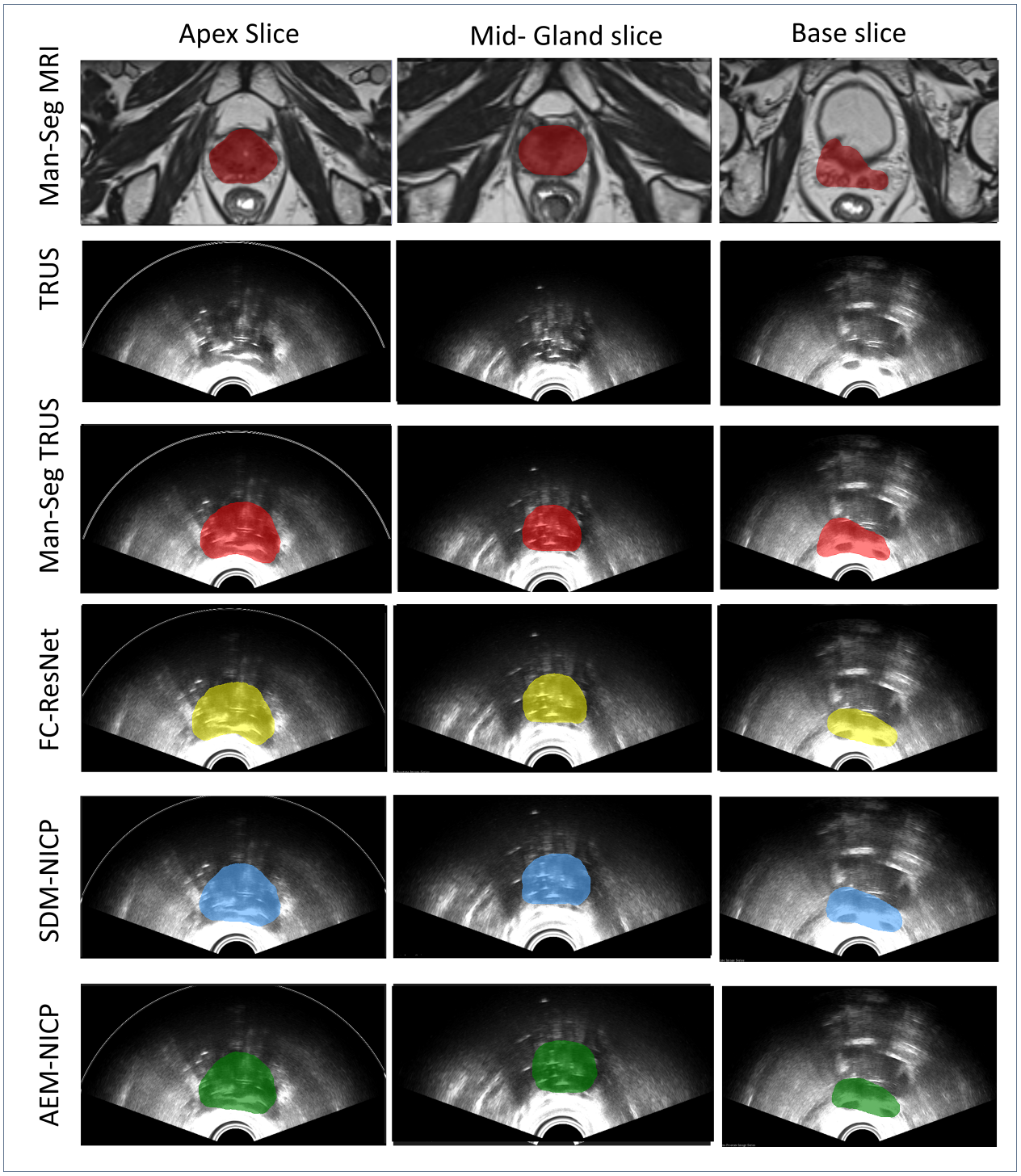

FIGURE 5.7 Segmented TRUS image for patient two in three sub-regions. Man-Seg MRI : original MRI with manually segmented prostate on top of it. TRUS : original TRUS image. Man-Seg TRUS : Manual segmentation shown on top of the TRUS image (Ground truth). FC-ResNet : Automatically segmented TRUS image. SDM-NICP : MRI surface fused to FC-ResNet surface by applying the SDM-NICP approach. AEM-NICP : MRI surface fused to FC-ResNet surface using the AEM-NICP proposed method.

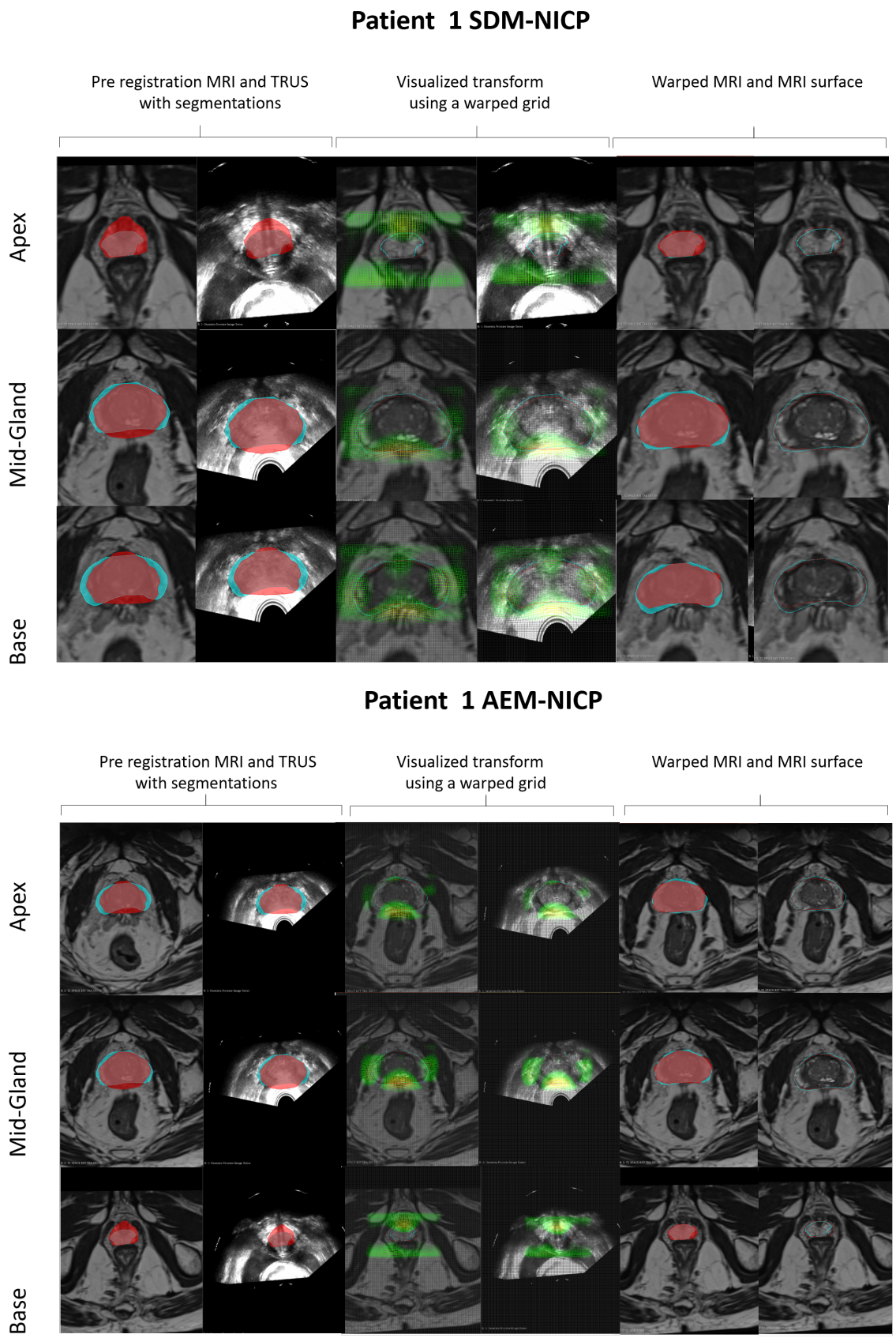

FIGURE 5.8 Sample MRI-TRUS registration results for a patient using 3D segmented surfaces as landmark and B-spline grid to warp the MRI on the targeted TRUS. The blue segmented area represents the prostate surface on TRUS image and the red area annotates the prostate gland on MRI.

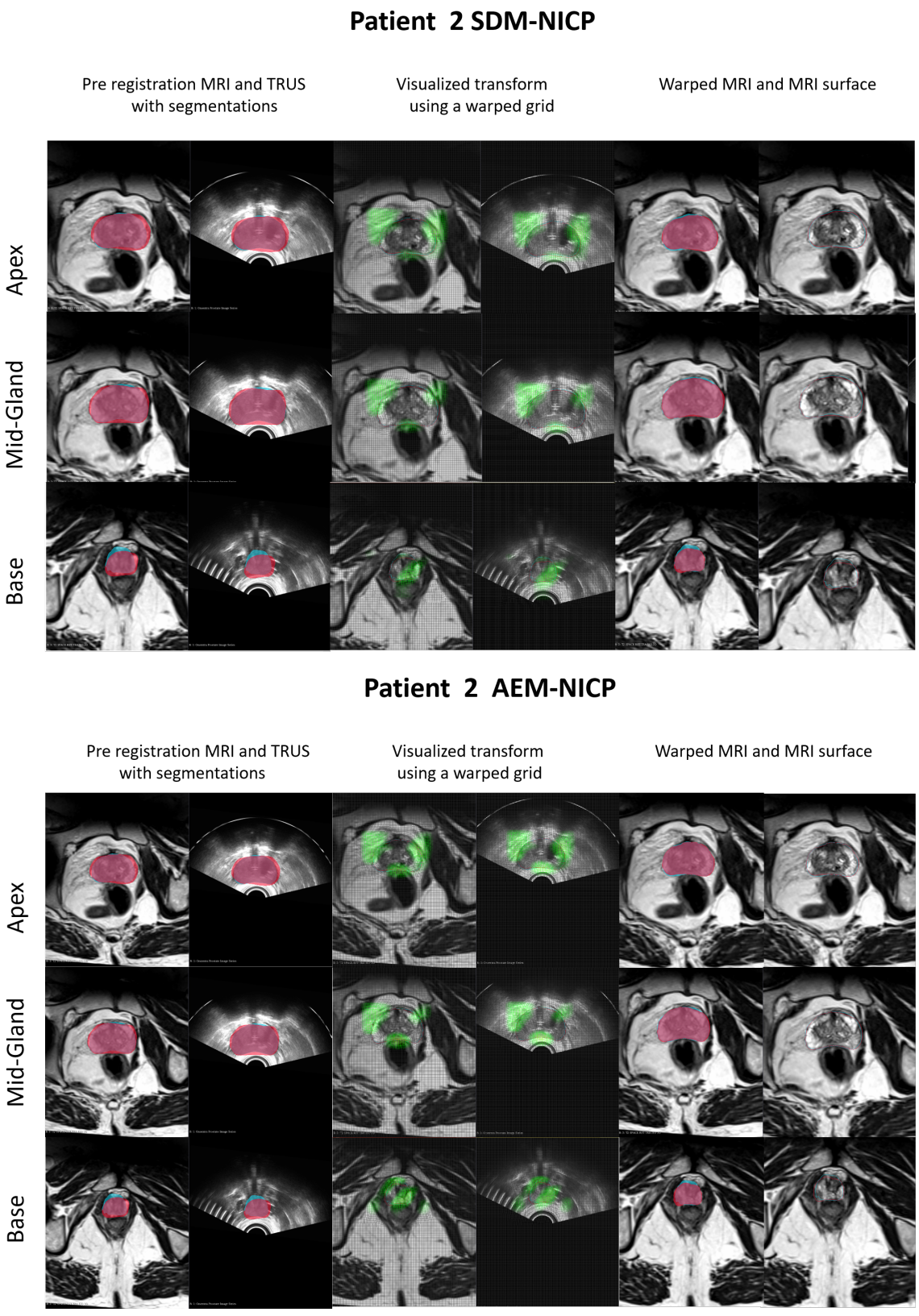

FIGURE 5.9 Sample MRI-TRUS registration results for a second patient using 3D segmented surfaces as landmark and B-spline grid to warp the MRI on the targeted TRUS. The blue segmented area represents the prostate surface on TRUS image and the red area annotates the prostate gland on MRI.

Figure 5.5 demonstrates the comparison between the proposed and the baseline registration approaches based on the MSD metric. As shown in Figure 5.5, SDM-NICP outperforms all other approaches in registering the whole prostate gland. Also, AEM-NICP outperforms the NICP algorithm in mid-gland and base regions.

Figure 5.6 and 5.7 show the segmented TRUS image for two distinct patients, respectively. One slice from each sub-region is demonstrated in these figures. The original MRI with its manual segmentation is shown along with the TRUS image and its corresponding ground truth segmentation. The visual result of FC-ResNet segmentation is shown in the fourth row. The last two rows illustrate the prostate segmentation after applying the two proposed MRI-TRUS fusion approaches. The SDM-NICP and AEM-NICP approaches register the segmented MRI surface to the auto-segmented TRUS surface. The visual comparison based on these two figures shows that the apical area is the most difficult region in both patients.

Finally, in order to warp the whole MR image into the space of the TRUS image a B-spline based registration approach is applied using the manually segmented surfaces as landmarks. Figures 5.8 and 5.9 show the visual results of MRI to TRUS registration on patient one and two, respectively.

TABLE 5.3 Comparison of the proposed SDM-NICP and AEM-NICP approaches with two baseline registration approaches, ICP and NICP, using manual TRUS segmentation. Evaluation is based on target registration errors (TRE) and means squared distance (MSD). The results are reported in each sub-region separately.

		Apex	Mid-Gland	Base
ICP	MSD (mm)	1.15 ±0.32	1.03 ±0.30	1.4 ±0.64
	TRE (mm)	7.93 ±2.31	7.98 ±2.35	7.52 ±0.63
NICP	MSD (mm)	0.62 ±0.12	0.47 ±0.19	0.53 ±0.37
	TRE (mm)	6.07 ±1.43	5.75 ±1.71	4.76 ±1.86
SDM-NICP	MSD (mm)	0.68 ±0.26	0.29 ±0.17	0.24 ±0.18
	TRE (mm)	6.33 ±1.89	5.14 ±1.72	4.08 ±1.49
AEM-NICP	MSE (mm)	2.49 ±0.16	0.32 ±0.27	0.24 ±0.16
	TRE (mm)	6.52 ±1.79	5.58 ±1.49	4.08 ±1.43

In another experiment, the proposed SDM based (SDM-NICP) and AEM based registration (SDM-NICP) approaches are compared to the NICP and ICP registrations. The TRE and MSD are computed between the resulting TRUS surface produced using each fusion approach and the corresponding manual TRUS segmentation. Table 5.3 reports these measures computed for SDM-NICP, AEM-NICP, NICP, and ICP registration approaches. The listed results are the average error measured for each area. It indicates how AEM-NICP outperforms in the base region and SDM-NICP results are best in the mid-Gland area, while in the apical region, NICP beats the two methods.

In the final experiment, the FC-ResNet automatic segmentation is applied to segment the TRUS surfaces on the unseen TRUS images. Table 5.4 reports the target registration errors (TRE), mean squared distance (MSD), and dice score for both proposed SDM-NICP and AEM-NICP approaches.

TABLE 5.4 Comparison of the proposed SDM-NICP and AEM-NICP approaches, using the automatic FC-ResNet segmentation on unseen TRUS image. Evaluation is based on target registration errors (TRE), mean squared distance (MSD), and dice score. The results are reported in each sub-region separately.

	SDM-NICP auto			AEM-NICP auto		
	Apex	Mid	Base	Apex	Mid	Base
MSD (mm)	0.75 ±0.26	0.32 ±0.27	0.30 ±0.11	2.76 ±0.26	0.37 ±0.27	0.29 ±0.13
TRE (mm)	6.42 ±1.82	5.73 ±1.73	4.63 ±1.89	6.52 ±1.60	6.26 ±1.12	4.57 ±1.48
DSC	72.5	84.2	88.07	72.4	84.05	88.08

As expected, using the automatic segmentation to extract TRUS surfaces produced slightly less accurate SDM-NICP and AEM-NICP registration results, but with insignificant differences to the manual TRUS segmentation (Table 5.4, 5.2). Furthermore, it is more realistic to use an automatic segmentation approach to extract the prostate surface in an intra-operative TRUS image to save time. The registration results using automatic TRUS segmentation is still promising.

CHAPITRE 6 DISCUSSION

In this thesis, two different surface-based MR-TRUS registration approaches were proposed. The first is based on a principal component analysis (PCA) approach to capture the statistical distribution of the deformation modes, coupled with a non-rigid ICP registration (NICP-SDM). The second is a deep neural network using multi-layered autoencoders, also coupled with a non-rigid ICP registration (NICP-AEM). The idea of both registration methods are to constrain an iterative closet point non-rigid registration to the plausible deformations.

The first proposed method is an SDM approach which includes two phases, training, and a registration phase. This method requires a training set of MRI-TRUS surface mesh pairs. During training, the prostate surface meshes are extracted from the MRI and TRUS images. Then, point to point correspondence is established between all surfaces. The MRI-TRUS surface deformation is computed for each MRI-TRUS pair, which results is a list of MRI-TRUS prostate surface deformations. These deformations are statistically modeled using a statistical deformation model (SDM) algorithm. In the registration phase, an unseen TRUS target volume is given. The trained SDM is incorporated into the non-rigid iterative closest point (NICP) registration algorithm to perform the MRI-TRUS fusion on the unseen patient data. The proposed SDM algorithm assumes that there is a linear relation between MR-TRUS deformations in the dataset. However, this linear assumption may not always be a correct representation of the dataset.

The autoencoder (AE) architecture includes a deep reconstruction process, through encoding and decoding. An AEM is trained to encode data into a lower-dimensional space. In addition, it learns how to reconstruct the data as a decoder output in a way that is close to the original input. In this thesis, AE is used to generate a wider range of deformations compared to SDM. AEM approach includes two steps : a training step and a registration step. The training step first extracts surface meshes from TRUS images in our training set then defines an Auto Encoder to learn the prostate shape variation on TRUS. In the registration phase, MRI and TRUS surface meshes are extracted for the unseen patient data. The non-rigid registration between the test MRI and the TRUS meshes is regularized using the trained AE.

In real scenarios, manual segmentation on intra-operative TRUS images is not readily available and involves a long manual delineation process. Therefore, a FC-ResNet automatic segmentation method is used to segment the intra-operative TRUS image at test time. Ho-

wever, it is usually possible to run the training phase in an offline mode. Thus, we can still take advantage of manual segmentation on both MRI and TRUS. Here, the main challenge is that the automatic TRUS segmentation fails to segment some slices and misses the prostate gland. This causes problems for the SPHARM PDM method that is used to point to point correspond the meshes in the training set. The SPHARM PDM framework requires monolithic meshes (single connected structure). A workaround that has been used in this thesis is to fill the gap in between the slices with the mean shape of the two neighboring slices from both sides of the missing mask. This mean shapes is used as initialization to fill the gap and create an integrated surface integrated as shown in Figure 4.5.

To evaluate the accuracy of the proposed method, the prostate surface is divided into three sub-regions (base, mid, and apex) and reported the TRE, MSD, and Dice metrics in each sub-region. This enabled us to provide detailed information about the registration accuracy. The experiment of segmenting the prostate gland using the FC-ResNet algorithm indicates the higher segmentation variability in the apex and base areas of the prostate. It appears to be more accurate in the mid-gland section of the prostate which suggests that the lowest variability in that area compared with the other areas. It also suggests that the most variability belongs to the apex region.

In another experiment, the performance of the proposed SDM-NICP and AEM-NICP method were compared to the gold standard manual registration (ground Truth Dice score = 90.1). The gold standard registration provides the clinical standard to the MRI-TRUS fusion problem by manually selecting some fiducial points. Experiments revealed that although the accuracy of the proposed surface-based registration approaches is less than the gold standard, it is not far from the ground truth and it could be still acceptable in practice, given the gain in time. The registration accuracy of the SDM-NICP and AEM-NICP was also compared to standard automatic registration approaches. Based on the evaluations of the proposed SDM and AEM approaches, the registration accuracy improved compared to two baseline methods (non-rigid iterative closest point (NICP) and rigid ICP). The rigid ICP registration results show poor registration performance across all three areas of the Base, Mid gland, and Apex of the prostate. The non-rigid ICP method performs better on the prostate areas especially the ones which are most difficult to segment in the TRUS images and are subject to the most variability (base and apex). The AEM-based non-rigid registration approach fails to beat the SDM Based approach in the mid-gland and apex areas, due to limitations in the dataset size. Yet, it outperforms the NICP algorithm in the mid gland and base sub-regions.

It is also demonstrated how the Bspline based FDD fuses the MRI onto the TRUS image by employing the MRI-TRUS surface deformation.

During the procedure, a fully automated processing system is needed to assess the needle localization. Manually placing the landmarks or manually segmenting the TRUS slices is not possible in real-time. For that reason, a fully automated experiment is also employed in which both SDM and AEM are applied to auto segmented TRUS images using FC-ResNet. Here, since the MR images are acquired in advance of the procedure, the manually segmented MRIs are used. Also, the training remains on manual segmentation. Experiments on testing the method on the manually segmented MRI surface to automatically segmented TRUS surface is compared with the standard NICP method. The method is shown to outperform the NICP method on the mid gland and base regions.

Based on our experiments, it was shown the highest variability was in the apex region and was the most challenging area in both segmentation and registration tasks. This has been reported in previous studies as well. It is common to achieve higher accuracy in the Mid gland, and less accurate in the apex and base sections for segmentation tasks. In a previous study by (52), it was suggested that in order to improve the segmentation accuracy in apex and base regions of the prostate mesh. Instead of using statistical shape models of the MRI as priors, we use the deformation models (SDM and AEM) to better capture the changes. Manual segmentation was used to extract prostate surfaces in the training set, which was required for the auto segmentation on unseen TRUS image (here we use FC-ResNet to produce the automatic segmentation).

According to our experiments, the overall Dice score of the whole prostate gland segmentation using the FC-ResNet algorithm is 82.13 (see Table 5.1). This result is higher than the computed total Dice values after employing our proposed registrations (see Table 5.4). However, in sub-region comparison, the Dice score in the Apex area shows some improvement after applying registration (from 72.2% to 72.5% in NICP-SDM and 72.4% in NICP-AEM). This indicates that employing our proposed registration on just the apex area after applying FC-ResNet segmentation on TRUS image could improve the segmentation accuracy.

Instead of using statistical shape models of the MRI as priors, we use the deformation models (SDM and AEM) to better capture the changes. Manual segmentation was used to extract prostate surfaces in the training set, which was required for the auto segmentation on unseen TRUS image (here we use FC-ResNet to produce auto segmentation).

On the last note, it should be noted that comparison of the results to other methods presented in the literature using different datasets originating from different clinical institutions which

will adopt different systems and practices is difficult. Also, most previous methods are not open source and the code is not available. Re-implementation of the methods is a potential perspective for future work, however, the reported accuracy in terms of mean square distance and Dice overlap is in the same range as what was obtained in this study.

CHAPITRE 7 CONCLUSION

7.1 Advancement of knowledge

In this thesis, several contributions were proposed towards improving clinical adoption of MRI-TRUS fusion guidance during biopsy and brachytherapy procedures. Using a newly FC-ResNet model for the unsupervised TRUS prostate segmentation, a statistical deformation model based registration (SDM-registration) and an Auto Encoder Model based registration (AEM-registration) were presented. Both of these approaches constrain the registration to anatomically plausible deformations.

The SDM-based registration approach first models the linear prostate deformations using a statistical deformation model (SDM). Then, the trained SDM is incorporated in the non-rigid Iterative Closest point (NICP) registration approach (8). The SDM algorithm assumes linear relation between deformations in the dataset.

The linear assumption in the SDM approach may not always be a correct representation of a the observed shape changes between the MRI (with no ERC coil) and the TRUS (with probe pressue). Thus, in second proposed approach a nonlinear approach based on Auto encoder is designed.

The Auto encoder (AE) is trained to encode data into a low-dimensional latent space. The AE learns how to decode the data back from the encoded representation to a reconstructed version in a way that is as close to the original input as possible. In this thesis, this characteristic of the AE is used to generate a wider range of deformations. In this proposed approach, the registration is constrained with an AE trained on meshes extracted from training MRI-TRUS images.

7.2 Limits and constraints

Although the results presented in this thesis are encouraging, there are general limitations to this work.

One constraint is the limited amount of data samples. As mentioned in the previous sections, our access to curated and validated datasets was limited. Therefore for example for training ResUNet the 2D architecture was designed to deal with lack of train data.

In addition, the auto-encoder could surely take advantage of more data to better represent the deformation between MR-TRUS. This could improve the accuracy of the AEM-based

registration approach.

Another constraint is the use of NICP registration algorithm as a baseline registration method. More powerful registration approaches like coherent point drift can be used instead. However, the same AEM or SDM model can be integrated in that.

7.3 Recommendations

7.3.1 Future direction on FC-ResNet improvement

One of the first things that will be considered in the future is training the network for more epochs and with more data. Continuing the training for more epochs could improve the segmentation accuracy, while generalization will benefit from extensive paired datasets.

The other thing that could be considered in the future work is increasing the number of residual blocks (stacked residual layers). The TRUS images are ambiguous and the prostate itself is so flexible that it undergoes changes easily. Therefore, it seems that the network needs to be more complex compared to when the data has bony structure or the imaging technique is of high quality (like MRI).

Furthermore, it is expected that replacing the 2D ResUNet approach with a 3D one can be effective to improve segmentation accuracy. Evidently, a 3D approach acknowledges the information from the neighbor 2D slices and would be a fair advantage over the 2D approach. In this work, the number of available dataset (45) was one of the limitations against using the 3D approach. However, it could be possible to augment this number with more real data samples or even proper augmentation algorithms in the future.

7.3.2 Future work

In this work, the NICP registration algorithm was implemented to compute the non-rigid deformation field. However, given the fact that a Kernel correlation (KC) and Coherent point drift (CPD) approach are more robust than NICP, replacing the NICP registration with these approaches could be more effective.

The SDM approach extracts the linear presentation of the MRI/TRUS deformation. While the AEM method implements an auto-encoder to model the prostate variations on TRUS images, using other advanced deep learning approaches (e.g., generative adversarial network (GAN)) may be explored to improve capturing the complex information about prostate deformation and achieve a more accurate registration result. However, a network like GAN's,

which is popular in replicating shape variations, are known to be difficult to train properly.

Finally, clinical translation of the tool and prospective evaluation during brachytherapy procedures is the next step towards evaluation of workflow improvements.

REFERENCES

[1] F. Couñago, G. Sancho, V. Catalá, D. Hernandez, M. Recio, S. Montemuiño, J. Hernández, A. Maldonado, and E. del Cerro, "Magnetic resonance imaging for prostate cancer before radical and salvage radiotherapy : What radiation oncologists need to know," *World Journal of Clinical Oncology*, vol. 8, p. 305, 08 2017.

[2] D. L. Davis, "Prostate cancer treatment with radioactive seed implantation," *AORN Journal*, vol. 68, no. 1, pp. 15 – 40, 1998. [Online]. Available : http://www.sciencedirect.com/science/article/pii/S0001209206627117

[3] S. Natarajan, L. S. Marks, D. J. A. Margolis, J. Huang, M. L. Macairan, P. Lieu, and A. Fenster, "Clinical application of a 3d ultrasound-guided prostate biopsy system," *Urologic oncology*, vol. 29, no. 3, pp. 334–342, 2011, 21555104[pmid]. [Online]. Available : https://pubmed.ncbi.nlm.nih.gov/21555104

[4] I. Kaplan, N. E. Oldenburg, P. Meskell, M. Blake, P. Church, and E. J. Holupka, "Real time mri-ultrasound image guided stereotactic prostate biopsy," *Magnetic Resonance Imaging*, vol. 20, no. 3, pp. 295 – 299, 2002. [Online]. Available : http://www.sciencedirect.com/science/article/pii/S0730725X02004903

[5] G. Haskins, J. Kruecker, U. Kruger, S. Xu, P. A. Pinto, B. J. Wood, and P. Yan, "Learning deep similarity metric for 3d mr–trus image registration," *International Journal of Computer Assisted Radiology and Surgery*, vol. 14, no. 3, pp. 417–425, Mar 2019. [Online]. Available : https://doi.org/10.1007/s11548-018-1875-7

[6] Q. Zeng, Y. Fu, J. Jeong, T. Zhen, T. Wang, Y. Lei, H. Mao, A. B. Jani, P. Patel, W. J. Curran, T. Liu, and X. Yang, "Weekly supervised convolutional long short-term memory neural networks for MR-TRUS registration," in *Medical Imaging 2020 : Ultrasonic Imaging and Tomography*, B. C. Byram and N. V. Ruiter, Eds., vol. 11319, International Society for Optics and Photonics. SPIE, 2020, pp. 203 – 209. [Online]. Available : https://doi.org/10.1117/12.2549760

[7] D. Karimi, Q. Zeng, P. Mathur, A. Avinash, S. Mahdavi, I. Spadinger, P. Abolmaesumi, and S. E. Salcudean, "Accurate and robust deep learning-based segmentation of the prostate clinical target volume in ultrasound images," *Medical Image Analysis*, vol. 57, pp. 186 – 196, 2019. [Online]. Available : http://www.sciencedirect.com/science/article/pii/S1361841519300623

[8] S. Shakeri, C. Menard, R. Lopes, and S. Kadoury, "Deformable MRI-TRUS surface registration from statistical deformation models of the prostate," in *Medical Imaging*

2019 : Image-Guided Procedures, Robotic Interventions, and Modeling, B. Fei and C. A. Linte, Eds., vol. 10951, International Society for Optics and Photonics. SPIE, 2019, pp. 504 – 510. [Online]. Available : https://doi.org/10.1117/12.2512844

[9] M. Drozdzal, G. Chartrand, E. Vorontsov, L. Di-Jorio, A. Tang, A. Romero, Y. Bengio, C. Pal, and S. Kadoury, "Learning normalized inputs for iterative estimation in medical image segmentation," *CoRR*, vol. abs/1702.05174, 2017. [Online]. Available : http://arxiv.org/abs/1702.05174

[10] K. S. Allen, H. Y. Kressel, P. H. Arger, and H. M. Pollack, "Age-related changes of the prostate : evaluation by mr imaging," *American Journal of Roentgenology*, vol. 152, no. 1, pp. 77–81, Jan 1989. [Online]. Available : https://doi.org/10.2214/ajr.152.1.77

[11] J. E. McNeal, "The zonal anatomy of the prostate," *The Prostate*, vol. 2, no. 1, pp. 35–49, 1981. [Online]. Available : https://onlinelibrary.wiley.com/doi/abs/10.1002/pros.2990020105

[12] L. Aaron, O. E. Franco, and S. W. Hayward, "Review of prostate anatomy and embryology and the etiology of benign prostatic hyperplasia," *Urologic Clinics*, vol. 43, no. 3, pp. 279–288, 2016.

[13] T. Chapman and S. J. Davies, "Functions and analysis of the seminal fluid proteins of male drosophila melanogaster fruit flies," *Peptides*, vol. 25, no. 9, pp. 1477 – 1490, 2004, m. Altstein. [Online]. Available : http://www.sciencedirect.com/science/article/pii/S0196978104002967

[14] A. Tsodikov, R. Gulati, E. A. M. Heijnsdijk, P. F. Pinsky, S. M. Moss, S. Qiu, T. M. de Carvalho, J. Hugosson, C. D. Berg, A. Auvinen, G. L. Andriole, M. J. Roobol, E. D. Crawford, V. Nelen, M. Kwiatkowski, M. Zappa, M. Luján, A. Villers, E. J. Feuer, H. J. de Koning, A. B. Mariotto, and R. Etzioni, "Reconciling the effects of screening on prostate cancer mortality in the erspc and plco trials," *Annals of internal medicine*, vol. 167, no. 7, pp. 449–455, Oct 2017, 28869989[pmid]. [Online]. Available : https://pubmed.ncbi.nlm.nih.gov/28869989

[15] M. van der Leest, E. Cornel, B. Israël, R. Hendriks, A. R. Padhani, M. Hoogenboom, P. Zamecnik, D. Bakker, A. Y. Setiasti, J. Veltman, H. van den Hout, H. van der Lelij, I. van Oort, S. Klaver, F. Debruyne, M. Sedelaar, G. Hannink, M. Rovers, C. Hulsbergen-van de Kaa, and J. O. Barentsz, "Head-to-head comparison of transrectal ultrasound-guided prostate biopsy versus multiparametric prostate resonance imaging with subsequent magnetic resonance-guided biopsy in biopsy-naïve men with elevated prostate-specific antigen : A large prospective multicenter clinical

study," *European Urology*, vol. 75, no. 4, pp. 570–578, 2019. [Online]. Available : http://www.sciencedirect.com/science/article/pii/S0302283818308807

[16] M. Peikari, "Characterization of ultrasound elevation beamwidth artefacts for brachytherapy needle insertion," Ph.D. dissertation, 2011, copyright - Database copyright ProQuest LLC ; ProQuest does not claim copyright in the individual underlying works ; Last updated - 2019-10-19. [Online]. Available : https://search.proquest.com/docview/1514486088?accountid=40695

[17] C. Das, A. Razik, S. Sharma, and S. Verma, "Prostate biopsy : when and how to perform," *Clinical Radiology*, vol. 74, no. 11, pp. 853 – 864, 2019. [Online]. Available : http://www.sciencedirect.com/science/article/pii/S0009926019301606

[18] H. A. Bogers, J. Sedelaar, H. P. Beerlage, J. J. de la Rosette, F. M. Debruyne, H. Wijkstra, and R. G. Aarnink, "Contrast-enhanced three-dimensional power doppler angiography of the human prostate : correlation with biopsy outcome," *Urology*, vol. 54, no. 1, pp. 97–104, Jul 1999. [Online]. Available : https://doi.org/10.1016/S0090-4295(99)00040-0

[19] J. Veltman, T. Goossen, P. Laguna, H. Wijkstra, and J. De la Rosette, "New technical improvements for trus in the diagnosis of prostate cancer." Elsevier, 9 2002.

[20] M. Norberg, L. Egevad, L. Holmberg, P. Sparén, B. Norlén, and C. Busch, "The sextant protocol for ultrasound-guided core biopsies of the prostate underestimates the presence of cancer," *Urology*, vol. 50, no. 4, pp. 562 – 566, 1997. [Online]. Available : http://www.sciencedirect.com/science/article/pii/S0090429597003063

[21] S. Y. Eskicorapci, D. E. Baydar, C. Akbal, M. Sofikerim, M. Günay, S. Ekici, and H. Ozen, "An extended 10-core transrectal ultrasonography guided prostate biopsy protocol improves the detection of prostate cancer," *European Urology*, vol. 45, no. 4, pp. 444 – 449, 2004. [Online]. Available : http://www.sciencedirect.com/science/article/pii/S0302283803006353

[22] E. C. Serefoglu, S. Altinova, N. S. Ugras, E. Akincioglu, E. Asil, and M. D. Balbay, "How reliable is 12-core prostate biopsy procedure in the detection of prostate cancer ?" *Canadian Urological Association journal = Journal de l'Association des urologues du Canada*, vol. 7, no. 5-6, pp. E293–E298, 2013, 22398204[pmid]. [Online]. Available : https://pubmed.ncbi.nlm.nih.gov/22398204

[23] M. D. Rifkin, E. A. Zerhouni, C. A. Gatsonis, L. E. Quint, D. M. Paushter, J. I. Epstein, U. Hamper, P. C. Walsh, and B. J. McNeil, "Comparison of magnetic resonance imaging and ultrasonography in staging early prostate cancer," *New England*

Journal of Medicine, vol. 323, no. 10, pp. 621–626, Sep 1990. [Online]. Available : https://doi.org/10.1056/NEJM199009063231001

[24] J. A. Onofrey, L. H. Staib, S. Sarkar, R. Venkataraman, and X. Papademetris, "Learning nonrigid deformations for constrained point-based registration for image-guided mr-trus prostate intervention," in *2015 IEEE 12th International Symposium on Biomedical Imaging (ISBI)*, 2015, pp. 1592–1595.

[25] S. Xu, J. Kruecker, B. Turkbey, N. Glossop, A. K. Singh, P. Choyke, P. Pinto, and B. J. Wood, "Real-time mri-trus fusion for guidance of targeted prostate biopsies," *Computer Aided Surgery*, vol. 13, no. 5, pp. 255–264, 2008, pMID : 18821344. [Online]. Available : https://doi.org/10.3109/10929080802364645

[26] N. Chrisochoides, A. Fedorov, A. Kot, N. Archip, P. Black, O. Clatz, A. Golby, R. Kikinis, and S. K. Warfield, "Toward real-time image guided neurosurgery using distributed and grid computing," in *Proceedings of the 2006 ACM/IEEE Conference on Supercomputing*, ser. SC '06. New York, NY, USA : Association for Computing Machinery, 2006, p. 76–es. [Online]. Available : https://doi.org/10.1145/1188455.1188536

[27] V. V. Karnik, A. Fenster, J. Bax, D. W. Cool, L. Gardi, I. Gyacskov, C. Romagnoli, and A. D. Ward, "Assessment of image registration accuracy in three-dimensional transrectal ultrasound guided prostate biopsy," *Medical Physics*, vol. 37, no. 2, pp. 802–813, 2010. [Online]. Available : https://aapm.onlinelibrary.wiley.com/doi/abs/10.1118/1.3298010

[28] R. Narayanan, J. Kurhanewicz, K. Shinohara, E. D. Crawford, A. Simoneau, and J. S. Suri, "Mri-ultrasound registration for targeted prostate biopsy," in *Proceedings of the Sixth IEEE International Conference on Symposium on Biomedical Imaging : From Nano to Macro*, ser. ISBI'09. IEEE Press, 2009, p. 991–994.

[29] M. R. Cheung and K. Krishnan, "Interactive deformation registration of endorectal prostate mri using itk thin plate splines," *Academic Radiology*, vol. 16, no. 3, pp. 351 – 357, 2009. [Online]. Available : http://www.sciencedirect.com/science/article/pii/S1076633208005692

[30] F. L. Bookstein, "Principal warps : thin-plate splines and the decomposition of deformations," *IEEE Transactions on Pattern Analysis and Machine Intelligence*, vol. 11, no. 6, pp. 567–585, 1989.

[31] J. Mitra, A. Oliver, R. Martí, X. Lladó, J. C. Vilanova, and F. Meriaudeau, "A thin-plate spline based multimodal prostate registration with optimal correspondences," in *2010 Sixth International Conference on Signal-Image Technology and Internet Based Systems*, 2010, pp. 7–11.

[32] R. Szeliski and S. Lavallee, "Matching 3-d anatomical surfaces with non-rigid deformations using octree-splines," in *Proceedings of IEEE Workshop on Biomedical Image Analysis*, 1994, pp. 144–153.

[33] C. Reynier, J. Troccaz, P. Fourneret, A. Dusserre, C. Gay-Jeune, J.-L. Descotes, M. Bolla, and J.-Y. Giraud, "Mri/trus data fusion for prostate brachytherapy. preliminary results," *Medical Physics*, vol. 31, no. 6, pp. 1568–1575, 2004. [Online]. Available : https://aapm.onlinelibrary.wiley.com/doi/abs/10.1118/1.1739003

[34] S. Viswanath, B. N. Bloch, M. Rosen, J. Chappelow, R. Toth, N. Rofsky, R. Lenkinski, E. Genega, A. Kalyanpur, and A. Madabhushi, "Integrating structural and functional imaging for computer assisted detection of prostate cancer on multi-protocol in vivo 3 tesla mri," *Proceedings of SPIE–the International Society for Optical Engineering*, vol. 7260, pp. 72 603I–72 603I, Feb 2009, 25301989[pmid]. [Online]. Available : https://pubmed.ncbi.nlm.nih.gov/25301989

[35] G. Xiao, B. N. Bloch, J. Chappelow, E. Genega, N. Rofsky, R. Lenkinski, and A. Madabhushi, "A structural-functional mri-based disease atlas : Application to computer-aided-diagnosis of prostate cancer," *Progress in Biomedical Optics and Imaging - Proceedings of SPIE*, vol. 7623, 03 2010.

[36] S. Oguro, J. Tokuda, H. Elhawary, S. Haker, R. Kikinis, C. M. C. Tempany, and N. Hata, "Mri signal intensity based b-spline nonrigid registration for pre- and intraoperative imaging during prostate brachytherapy," *Journal of magnetic resonance imaging : JMRI*, vol. 30, no. 5, pp. 1052–1058, Nov 2009, 19856437[pmid]. [Online]. Available : https://pubmed.ncbi.nlm.nih.gov/19856437

[37] G. Nir, R. S. Sahebjavaher, P. Kozlowski, S. D. Chang, E. C. Jones, S. L. Goldenberg, and S. E. Salcudean, "Registration of whole-mount histology and volumetric imaging of the prostate using particle filtering," *IEEE Transactions on Medical Imaging*, vol. 33, no. 8, pp. 1601–1613, 2014.

[38] P. J. Besl and N. D. McKay, "A method for registration of 3-d shapes," *IEEE Transactions on Pattern Analysis and Machine Intelligence*, vol. 14, no. 2, pp. 239–256, 1992.

[39] S. Ourselin, A. Roche, S. Prima, and N. Ayache, "Block matching : A general framework to improve robustness of rigid registration of medical images," in *Medical Image Computing and Computer-Assisted Intervention – MICCAI 2000*, S. L. Delp, A. M. DiGoia, and B. Jaramaz, Eds. Berlin, Heidelberg : Springer Berlin Heidelberg, 2000, pp. 557–566.

[40] J. Mitra, A. Srikantha, D. Sidibé, R. Martí, A. Oliver, X. Llado, S. Ghose, J. C. Vilanova, J. Comet, and F. Meriaudeau, "A shape-based statistical method to retrieve 2d trus-

mr slice correspondence for prostate biopsy," *Proceedings of SPIE - The International Society for Optical Engineering*, vol. 8314, 02 2012.

[41] J. Mitra, Z. Kato, R. Martí, A. Oliver, X. Lladó, D. Sidibé, S. Ghose, J. C. Vilanova, J. Comet, and F. Meriaudeau, "A spline-based non-linear diffeomorphism for multimodal prostate registration," *Medical Image Analysis*, vol. 16, no. 6, pp. 1259–1279, 2012. [Online]. Available : http://www.sciencedirect.com/science/article/pii/S1361841512000527

[42] Y. Sun, W. Qiu, J. Yuan, C. Romagnoli, and A. Fenster, "Three-dimensional nonrigid landmark-based magnetic resonance to transrectal ultrasound registration for image-guided prostate biopsy," *Journal of medical imaging (Bellingham, Wash.)*, vol. 2, no. 2, pp. 025 002–025 002, Apr 2015, 26158111[pmid]. [Online]. Available : https://pubmed.ncbi.nlm.nih.gov/26158111

[43] D. W. Cool, J. Bax, C. Romagnoli, A. D. Ward, L. Gardi, V. Karnik, J. Izawa, J. Chin, and A. Fenster, "Fusion of mri to 3d trus for mechanically-assisted targeted prostate biopsy : System design and initial clinical experience," in *Prostate Cancer Imaging. Image Analysis and Image-Guided Interventions*, A. Madabhushi, J. Dowling, H. Huisman, and D. Barratt, Eds. Berlin, Heidelberg : Springer Berlin Heidelberg, 2011, pp. 121–133.

[44] Y. Hu, H. U. Ahmed, Z. Taylor, C. Allen, M. Emberton, D. Hawkes, and D. Barratt, "Mr to ultrasound registration for image-guided prostate interventions," *Medical Image Analysis*, vol. 16, no. 3, pp. 687 – 703, 2012, computer Assisted Interventions. [Online]. Available : http://www.sciencedirect.com/science/article/pii/S1361841510001295

[45] J. A. Onofrey, L. H. Staib, S. Sarkar, R. Venkataraman, C. B. Nawaf, P. C. Sprenkle, and X. Papademetris, "Learning non-rigid deformations for robust, constrained point-based registration in image-guided mr-trus prostate intervention," *Medical Image Analysis*, vol. 39, pp. 29 – 43, 2017. [Online]. Available : http://www.sciencedirect.com/science/article/pii/S1361841517300452

[46] X. Papademetris, A. Jackowski, R. Schultz, L. Staibl, and J. Duncan, "Miccai'03," 2003.

[47] D. Rueckert, L. I. Sonoda, C. Hayes, D. L. Hill, M. O. Leach, and D. J. Hawkes, "Non-rigid registration using free-form deformations : application to breast mr images," *IEEE transactions on medical imaging*, vol. 18, no. 8, pp. 712–721, 1999.

[48] M. Moradi, F. Janoos, A. Fedorov, P. Risholm, T. Kapur, L. D. Wolfsberger, P. L. Nguyen, C. M. Tempany, and W. M. Wells, "Two solutions for registration of ultrasound to mri for image-guided prostate interventions," *Conference proceedings : ... Annual International Conference of the IEEE Engineering in Medicine and*

Biology Society. IEEE Engineering in Medicine and Biology Society. Annual Conference, vol. 2012, pp. 1129–1132, 2012, 23366095[pmid]. [Online]. Available : https://pubmed.ncbi.nlm.nih.gov/23366095

[49] P. Yan, S. Xu, B. Turkbey, and J. Kruecker, "Adaptively learning local shape statistics for prostate segmentation in ultrasound," *IEEE Transactions on Biomedical Engineering*, vol. 58, no. 3, pp. 633–641, 2011.

[50] O. Zettinig, J. Rackerseder, B. Lentes, T. Maurer, K. Westenfelder, M. Eiber, B. Frisch, and N. Navab, "Preconditioned intensity-based prostate registration using statistical deformation models," in *2017 IEEE 14th International Symposium on Biomedical Imaging (ISBI 2017)*, 2017, pp. 853–857.

[51] Y. Wang, Z. Deng, X. Hu, L. Zhu, X. Yang, X. Xu, P.-A. Heng, and D. Ni, "Deep attentional features for prostate segmentation in ultrasound," in *Medical Image Computing and Computer Assisted Intervention – MICCAI 2018*, A. F. Frangi, J. A. Schnabel, C. Davatzikos, C. Alberola-López, and G. Fichtinger, Eds. Cham : Springer International Publishing, 2018, pp. 523–530.

[52] Q. Zeng, G. Samei, D. Karimi, C. Kesch, S. S. Mahdavi, P. Abolmaesumi, and S. E. Salcudean, "Prostate segmentation in transrectal ultrasound using magnetic resonance imaging priors," *International Journal of Computer Assisted Radiology and Surgery*, vol. 13, no. 6, pp. 749–757, 2018. [Online]. Available : https://doi.org/10.1007/s11548-018-1742-6

[53] O. Ronneberger, P. Fischer, and T. Brox, "U-net : Convolutional networks for biomedical image segmentation," in *Medical Image Computing and Computer-Assisted Intervention – MICCAI 2015*, N. Navab, J. Hornegger, W. M. Wells, and A. F. Frangi, Eds. Cham : Springer International Publishing, 2015, pp. 234–241.

[54] Z. Zhang, "Iterative point matching for registration of free-form curves and surfaces," *International Journal of Computer Vision*, vol. 13, no. 2, pp. 119–152, 1994. [Online]. Available : https://doi.org/10.1007/BF01427149

[55] B. Amberg, S. Romdhani, and T. Vetter, "Optimal step nonrigid icp algorithms for surface registration," in *Computer Vision and Pattern Recognition, 2007. CVPR'07. IEEE Conference on*. IEEE, 2007, pp. 1–8.

[56] B. Allen, B. Curless, and Z. Popović, "The space of human body shapes : Reconstruction and parameterization from range scans," *ACM Trans. Graph.*, vol. 22, no. 3, p. 587–594, Jul. 2003. [Online]. Available : https://doi.org/10.1145/882262.882311

[57] T. W. Sederberg and S. R. Parry, "Free-form deformation of solid geometric models," *SIGGRAPH Comput. Graph.*, vol. 20, no. 4, p. 151–160, Aug. 1986. [Online]. Available : https://doi.org/10.1145/15886.15903

[58] S. Coquillart, "Extended free-form deformation : A sculpturing tool for 3d geometric modeling," *SIGGRAPH Comput. Graph.*, vol. 24, no. 4, p. 187–196, Sep. 1990. [Online]. Available : https://doi.org/10.1145/97880.97900

[59] A. H. Barr, "Global and local deformations of solid primitives," *SIGGRAPH Comput. Graph.*, vol. 18, no. 3, p. 21–30, Jan. 1984. [Online]. Available : https://doi.org/10.1145/964965.808573

[60] L. Cinque, S. Levialdi, and A. Malizia, "Shape description using cubic polynomial bezier curves," *Pattern Recognition Letters*, vol. 19, no. 9, pp. 821 – 828, 1998. [Online]. Available : http://www.sciencedirect.com/science/article/pii/S0167865598000695

[61] D. Rueckert, L. I. Sonoda, C. Hayes, D. L. G. Hill, M. O. Leach, and D. J. Hawkes, "Nonrigid registration using free-form deformations : application to breast mr images," *IEEE Transactions on Medical Imaging*, vol. 18, no. 8, pp. 712–721, 1999.

[62] Z. WU, L. Tian, W. Jiang, D. Yi, and Q. Zhiguang, "Medical image registration using b-spline transform."

[63] J. Kybic and M. Unser, "Fast parametric elastic image registration," *IEEE Transactions on Image Processing*, vol. 12, no. 11, pp. 1427–1442, 2003.

[64] C. Lindner, "Chapter 1 - automated image interpretation using statistical shape models," in *Statistical Shape and Deformation Analysis*, G. Zheng, S. Li, and G. Székely, Eds. Academic Press, 2017, pp. 3 – 32. [Online]. Available : http://www.sciencedirect.com/science/article/pii/B978012810493400002X

[65] M. Lüthi, A. Forster, T. Gerig, and T. Vetter, "Chapter 7 - shape modeling using gaussian process morphable models," in *Statistical Shape and Deformation Analysis*, G. Zheng, S. Li, and G. Székely, Eds. Academic Press, 2017, pp. 165 – 191. [Online]. Available : http://www.sciencedirect.com/science/article/pii/B9780128104934000080

[66] E. Plaut, "From principal subspaces to principal components with linear autoencoders," 2018.

[67] K. He, X. Zhang, S. Ren, and J. Sun, "Deep residual learning for image recognition," *CoRR*, vol. abs/1512.03385, 2015. [Online]. Available : http://arxiv.org/abs/1512.03385

[68] S. Khallaghi, C. A. Sánchez, A. Rasoulian, Y. Sun, F. Imani, A. Khojaste, O. Goksel, C. Romagnoli, H. Abdi, S. Chang, P. Mousavi, A. Fenster, A. Ward, S. Fels, and

P. Abolmaesumi, “Biomechanically constrained surface registration : Application to mr-trus fusion for prostate interventions,” *IEEE Transactions on Medical Imaging*, vol. 34, no. 11, pp. 2404–2414, Nov 2015.

[69] L. R. Dice, “Measures of the amount of ecologic association between species,” *Ecology*, vol. 26, no. 3, pp. 297–302, 1945. [Online]. Available : https://esajournals.onlinelibrary.wiley.com/doi/abs/10.2307/1932409

[70] E. Poulin, K. Boudam, C. Pinter, S. Kadoury, A. Lasso, G. Fichtinger, and C. Ménard, “Validation of mri to trus registration for high-dose-rate prostate brachytherapy,” *Brachytherapy*, vol. 17, no. 2, pp. 283–290, Mar 2018. [Online]. Available : https://doi.org/10.1016/j.brachy.2017.11.018

[71] A. Fedorov, S. Khallaghi, C. A. Sánchez, A. Lasso, S. Fels, K. Tuncali, E. N. Sugar, T. Kapur, C. Zhang, W. Wells, P. L. Nguyen, P. Abolmaesumi, and C. Tempany, “Open-source image registration for mri-trus fusion-guided prostate interventions,” *International journal of computer assisted radiology and surgery*, vol. 10, no. 6, pp. 925–934, Jun 2015, 25847666[pmid]. [Online]. Available : https://pubmed.ncbi.nlm.nih.gov/25847666

[72] W. E. Lorensen and H. E. Cline, “Marching cubes : A high resolution 3d surface construction algorithm,” *SIGGRAPH Comput. Graph.*, vol. 21, no. 4, p. 163–169, Aug. 1987. [Online]. Available : https://doi.org/10.1145/37402.37422

[73] H. Hufnagel, X. Pennec, J. Ehrhardt, N. Ayache, and H. Handels, “Generation of a statistical shape model with probabilistic point correspondences and the expectation maximization- iterative closest point algorithm,” *Int. J. Computer Assisted Radiology and Surgery*, vol. 2, pp. 265–273, Mar 2008.

[74] J. M. Fitzpatrick, J. B. West, and C. R. Maurer, “Predicting error in rigid-body point-based registration,” *IEEE Transactions on Medical Imaging*, vol. 17, no. 5, pp. 694–702, 1998.

[75] C. W. Helstrom, “Minimum mean-squared error of estimates in quantum statistics,” *Physics letters A*, vol. 25, no. 2, pp. 101–102, 1967.

[76] N. Umetani, “Exploring generative 3d shapes using autoencoder networks,” in *SIGGRAPH Asia 2017 Technical Briefs*, ser. SA ’17. New York, NY, USA : Association for Computing Machinery, 2017. [Online]. Available : https://doi.org/10.1145/3145749.3145758